Charles University in Prague
Faculty of Mathematics and Physics

Lattice Dynamics of Relaxor Ferroelectrics

Ph.D. Thesis

Martin Kempa

Supervisor: RNDr. Jan Petzelt, DrSc.
Institute of Physics
Academy of Sciences of the Czech Republic

F-3: Physics of Condensed Matter and Materials Research
Prague 2008

Acknowledgements

In the first place, I am very grateful to my supervisors: to Jan Petzelt, for introducing me to the field of relaxors and for devoting his time to many fruitful discussions; to Jirka Hlinka, for teaching me how an experimental physicist should work and view the problems, and for his helping hand whenever I needed; to Jiří Kulda, for introducing me to neutron scattering techniques, for helping with experiments and for many useful comments and discussions; to Stanislav Kamba, for introducing me to infrared spectrosopy and for valuable advice.

I would also like to thank to my colleagues from the Department of Dielectrics, for a friendly and pleasant atmosphere, and for many pieces od advice which have been facilitating my work.

This thesis is a result of collaboration with many other people who helped me during my studies. I want to express my thanks to all of them.

This work was supported by the Doctoral Grant no. 202/05/H003.

Contents

Units and abbreviations

Throughout this thesis, we use the following units:

- meV (milli electron volts) as spectroscopic units.
  The conversions to other units are:
  $1\,\mathrm{meV} \doteq 0.242\,\mathrm{THz} \doteq 8.065\ \mathrm{cm}^{-1}$
  and this frequency also corresponds to:
  temperature 11.604 K and wavelength 12.398 Å.

  We will use both energy E and frequency ω when describing excitations in the lattice ($E = \hbar\omega$), depending on what is more suitable in each case. This is purely a matter of appellation, as both E and ω will be given in meV.

  Similarly, energy transfers will be labelled E or ΔE but they represent exactly the same.

- reduced (dimensionless) phonon wave vectors expressed in r.l.u. (reciprocal lattice units) to express positions in reciprocal space: $a^* = 2\pi/a$, where a is a lattice constant of a crystal along a certain symmetry axis. As an example, for PMN: $a \doteq 4.04$Å, $a^* \doteq 1.555\,\text{Å}^{-1}$).

Chemical compounds:

PZN–xPT	(1-x)$\mathrm{Pb(Zn_{1/3}Nb_{2/3})O_3}$–x$\mathrm{PbTiO_3}$
PMN–xPT	(1-x)$\mathrm{Pb(Mg_{1/3}Nb_{2/3})O_3}$–x$\mathrm{PbTiO_3}$
PST	$\mathrm{Pb(Sc_{1/2}Ta_{1/2})O_3}$

Abbreviations used in the text:

BZ	Brillouin Zone
DHO	damped harmonic oscillator
ILL	Institut Laue-Langevin, Grenoble, France
INS	inelastic neutron scattering
IXS	inelastic X-ray scattering
IR	infrared
LLB	Laboratoire Leon Brillouin, CE Saclay, France
PG	pyrolytic graphite
PNR	polar nanoregion
PSI	Paul Scherrer Institut, Villigen, Switzerland
SM	soft (phonon) mode
TAS	three-axis spectroscopy
TOF	time-of-flight (spectroscopy)

Chapter 1

Introduction

Relaxor ferroelectrics differ from "normal" ferroelectrics mainly by a smeared or absent structural phase transition, and by very broad and frequency-dependent dielectric permittivity maxima. This behaviour is now qualitatively understood in terms of polar nanoregions, which are present in the material within a large temperature range.

Some relaxor materials possess anomalously high piezoelectric and other material constants. This fact has already been widely used in many applications and devices: piezoelectric devices, capacitors, transducers, actuators, random access memories and others. The highest performance is attained for solid solutions of these relaxors with lead titanate $PbTiO_3$ (e.g. PZN–8%PT).

Ferroelectrics with a "simple" perovskite structure (such as $PbTiO_3$ and $BaTiO_3$) have served as model materials for elucidating the mechanisms of lattice dynamics since the boom of spectroscopic studies in the early 1960s. They are helping to understand dynamical properties of more complex systems, such as relaxors and other mixed perovskite crystals.

The most powerful and convenient way, how to obtain low-frequency phonon dispersions of solids, is by inelastic neutron scattering (INS), using three-axis spectroscopy (TAS) on reactor sources. On the other hand, the relatively low flux of neutron sources usually requires the use of "large" single crystals (typically 10-1000 mm^3). Because of this restriction, INS studies of many single-crystalline materials have been excluded. Recently, large enough and high-quality single crystals of relaxors, $PbTiO_3$ and their solid solutions have been grown, which allowed a new series of INS investigations.

After a short introduction to the properties of ferroelectrics and relaxors (chapter 2) and to neutron scattering (chapter 3), we give a brief overwiev of three-axis spectroscopy and the practical aspects of this technique (chapter 4). The experimental part is devoted to lattice-dynamical studies of relaxor ferroelectrics PMN and PZN–8%PT (chapter 5) and of ferroelectric $PbTiO_3$ (chapter 6). Brief summary and conclusions are given in chapter 7.

Chapter 2

Relaxor ferroelectrics

Relaxor ferroelectrics are a special case of ferroelectrics, in which the ferroelectric state arises only in nanoscopic regions. In order to describe the similarities and differences between them, we will first describe the properties of ferroelectrics[1]. In the final part, we summarize experimental results from our infrared studies on relaxors.

2.1 Ferroelectrics

A crystal is said to be ferroelectric when it possesses a spontaneous polarization $\vec{P}_s$ below a certain transition temperature T_C. The existence of $\vec{P}_s$ implies two or more crystallographically equivalent orientation states in the crystal. Usually a large enough, as-grown crystal consists of regions, called (macroscopic) domains, in which $\vec{P}_s$ is uniform (has the same direction in all unit cells in the domain). The reason why such domains are created in the crystal is the condition of minimum energy of the system.

The spontaneous polarization $\vec{P}_s$ can be switched between these states by applying strong enough external electric field. This property is used for poling – a process of preparing monodomain crystals, in which $\vec{P}_s$ has the same direction in the whole volume. For a poled ferroelectric crystal, the switching of polarization direction to other orientation involves hysteresis due to the barrier resisting the polarization switching (see left panel of figure 2.1, part (a)).

For ferroelectrics which undergo a structural phase transition at a finite temperature T_C, the polarization $\vec{P}_s$ becomes zero at this temperature (figure 2.1b). The non-polar phase above T_C is called the paraelectric phase.

---

[1] Incipient ferroelectrics, with zero (or even negative) extrapolated T_C are not in the scope of this thesis.

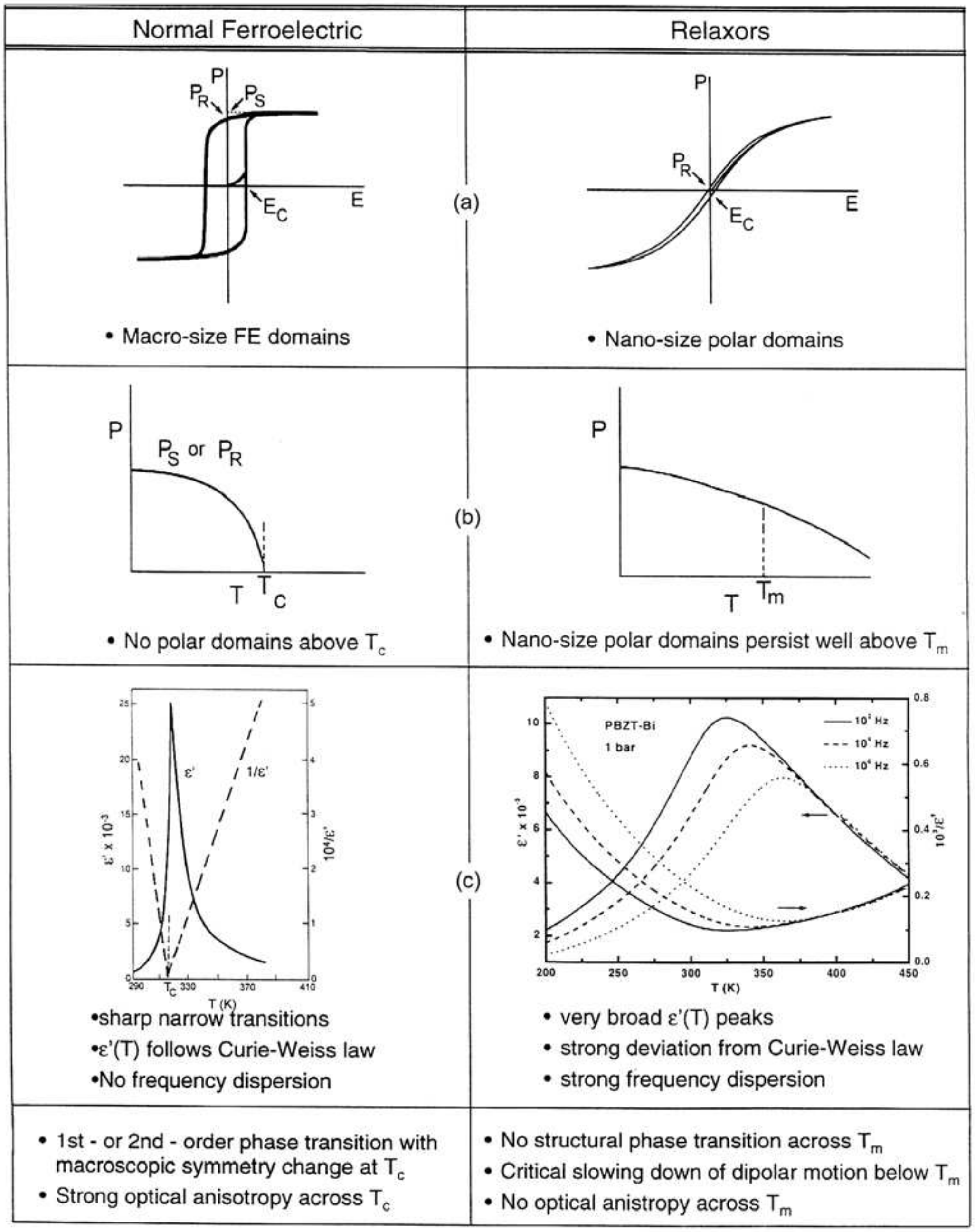

Normal Ferroelectric	Relaxors
• Macro-size FE domains	• Nano-size polar domains
• No polar domains above T_c	• Nano-size polar domains persist well above T_m
•sharp narrow transitions •ε'(T) follows Curie-Weiss law •No frequency dispersion	• very broad ε'(T) peaks • strong deviation from Curie-Weiss law • strong frequency dispersion
• 1st - or 2nd - order phase transition with macroscopic symmetry change at T_c • Strong optical anisotropy across T_c	• No structural phase transition across T_m • Critical slowing down of dipolar motion below T_m • No optical anistropy across T_m

Figure 2.1: Summary of the characteristic differences between ferroelectrics and relaxors. Taken from [Samara 03].

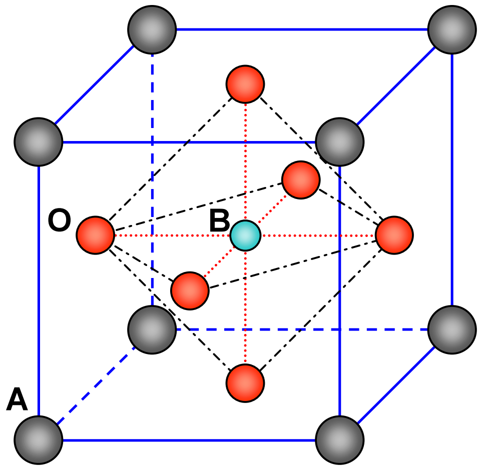

Figure 2.2: The perovskite ABO_3 structure.

The phase transition is accompanied by a sharp peak in the temperature dependence of the dielectric permittivity (figure 2.1c). Below T_C, there is one or more ferroelectric phases, depending on the thermodynamic balance of the particular crystal. For example, $BaTiO_3$ under cooling changes its structure from cubic to tetragonal, orthorhombic and rhombohedral, while $PbTiO_3$ undergoes only one cubic-to-tetragonal phase transition. Phase transitions can be equally induced by changing e.g. pressure instead of temperature (see section 6.3).

Depending on symmetry, a certain type of transverse lattice vibration (so called soft phonon mode, SM) is usually responsible for the structural phase transition. We say that the mode softens (decreases its frequency ω_{SM}) when approaching T_C:

$$\omega_{SM}^2(T) = A(T_C - T) \ . \tag{2.1}$$

The polarization direction in a domain is determined by the crystal symmetry. Concerning perovskite ferroelectrics with ABO_3 structure (see figure 2.2), there are two basic mechanisms how the polarization is created. In the case of displacive ferroelectrics (such as $PbTiO_3$), one or more atoms are displaced in one direction with respect to the rest of the lattice. In order-disorder ferroelectrics (e.g. KDP), some atoms in the unit cell may exist in several equivalent positions, determined by interatomic forces. In the ferroelectric phase, some of these positions are energetically favourable, so the atom is effectively shifted from its symmetry position in the unit cell.

2.2 Relaxors

Relaxor ferroelectrics (relaxors), first reported about half a century ago [Smolenskii 58], are sometimes called “dirty ferroelectrics” [Burns 76b]. They are materials for which the maximum of the dielectric constant $\varepsilon'(T)$ is very broad (with frequency dispersion over the Hz-GHz range, which clearly indicates relaxation processes at multiple time-scales, see below) and does not correspond to a transition from non-polar to a macroscopic ferroelectric polar phase. Instead, a phrase “diffuse phase transition” is suitable to describe the change from the high-temperature ”paraelectric” state to the low-temperaure ”frozen” state. The dielectric maximum is also strongly frequency-dependent, and the hysteresis loop is very slim near T_m, the temperature at which $\varepsilon'(T)$ reaches its maximum (see right panel of figure 2.1).

In pure relaxors [such as mixed perovskite system $Pb(Mg_{1/3}Nb_{2/3})O_3$ (PMN)], the high-temperature paraelectric structure is maintained down to the lowest temperatures. This behaviour is now qualitatively understood by the presence of the so-called polar nanoregions (PNRs), which are formed already few hundreds K above T_m, so that at nanoscale the symmetry is already broken on both sides of the dielectric anomaly. More generally, PNRs play an important role in the dielectric properties of relaxors [Westphal 92, Tagantsev 98].

The formation of PNRs is caused by the presence of smaller, randomly oriented nanoscale chemical clusters, induced by compositional fluctuations of the B-site atoms [Iwata 00] (Mg and Nb in the case of PMN). While the macroscopic symmetry of perovskite relaxors (at high enough temperatures) is $Pm\bar{3}m$, the chemical regions are considered to be of $Fm\bar{3}m$ symmetry, and they disappear at high temperatures; the PNRs are of rhombohedral symmetry and disappear only gradually with increasing temperature [Burns 83].

The soft phonon mode (SM), connected to the phase transition in the case of ferroelectrics, still plays an important role in relaxors, as will be described in chapter 5. Its frequency follows the Cochran law:

$$\omega_{SM}^2(T) = A(T_d - T) \; . \tag{2.2}$$

where T_d is the Burn temperature [Burns 83]. Below T_d, a new overdamped excitation appears below the SM frequency (figure 2.3). It is believed that this relaxational excitation has its origin in the dynamics of PNRs. This excitation is usually called central mode (dielectric relaxation) and usually splits into two components: the first appears in the THz range due to the breaking of local symmetry as a consequence of PNRs, another originates

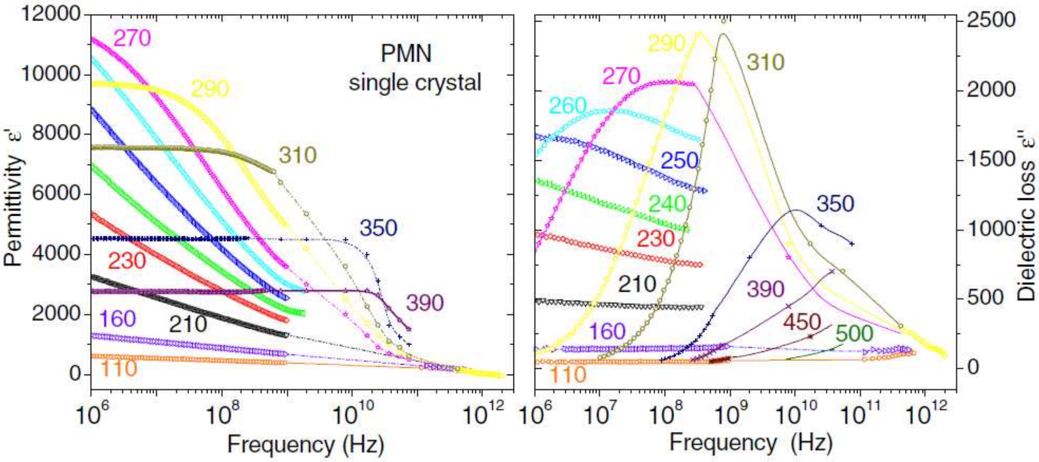

Figure 2.3: Frequency dependence of the real and imaginary part of the dielectric permittivity of PMN single crystal in the microwave and high-frequency range, showing the dielectric relaxation, at various temperatures (in Kelvins). Taken from [Kamba 05a].

from cluster breathing and flipping [Bovtun 04]. The mean relaxation time obeys the Vogel-Fulcher law:

$$\omega_R = \omega_\infty \exp \frac{-E_a}{T - T_{VF}} \tag{2.3}$$

where T_{VF} is freezing temperature (for PMN, e.g., $T_{VF} \approx 200\,\mathrm{K}$), E_a activation energy ($E_a \approx 800\,\mathrm{K}$ for PMN) and ω_∞ the high-temperature limit of the relaxation frequency ($\omega_\infty \approx 5.7\,\mathrm{THz}$ for PMN) [Bovtun 04]. Below T_{VF}, the loss maximum becomes very broad, and only frequency independent dielectric losses can be observed.

On the application side, relaxors, compared to ferroelectrics, usually offer higher dielectric constants, and anomalously high material constants (piezoelectric, pyroelectric, electrostriction etc.) These properties are attractive for a broad range of applications and devices, many of them already widely used (e.g. piezoelectric devices, capacitors, transducers, actuators, random access memories).

Since the discovery of the giant piezoelectric performance of PZN–xPT single crystals by Park and Shrout [Park 87], there was a tremendous effort in growing, investigation and understanding of these and analogous mixed perovskite systems. The highest performance is attained for compositions close to the so called morphotropic phase boundary (MPB). This

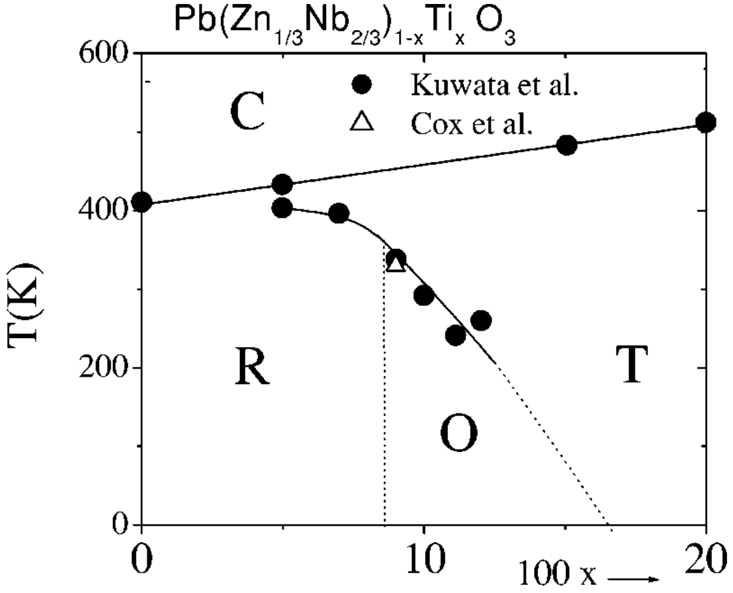

Figure 2.4: $T-x$ phase diagram of PZN–xPT, with a morphotropic phase boundary at x=9%. Taken from [La-Orauttapong 02]. Remark: it was also proposed [Noheda 00] that a monoclinic phase exists between the tetragonal and rhombohedral phases in the MPB region.

is a boundary between different structural phases in the $T-x$ phase diagram (see figure 2.4). For example, the MPB of PZN–xPT is located near x=9%, so that papers devoted to characterization of these crystals with x=8–9% of $PbTiO_3$ are abundant, and there has also been a number of elastic and inelastic neutron scattering studies [Gehring 00a, Ohwada 01, Ohwada 03, Uesu 02, Kiat 02, La-Orauttapong 03, Hlinka 03a, Hlinka 03b, La-Orauttapong cm 03, Gehring 04a, Gehring 04b]. However, the dynamical properties of these mixed solid-solution relaxors are still understood only vaguely.

Relaxors appear to be an intermediate state between ferroelectrics and dipolar glasses. The main difference between relaxors and dipolar glasses is in the size of the areas (polar clusters) where the dipoles are oriented: it is much smaller in the case of dipolar glasses. Also, relaxors under external electric field may be switched into a ferroelectric phase [Park 87], which is not possible in the case of dipolar glasses.

2.3 Far-infrared properties of relaxors

In this section, we report on experimental results obtained from our infrared studies on PMN and PST ($Pb(Sc_{1/2}Ta_{1/2})O_3$) thin films[2].

The unpolarized far IR transmission spectra were taken using an FTIR spectrometer Bruker IFS 113v at temperatures between 20 and 900 K with the resolution of $0.5\,\mathrm{cm}^{-1}$.

The complex dielectric function can be expressed as the sum of damped harmonic oscillators; then it has the form [Petzelt 87]

$$\varepsilon(\omega) = \varepsilon'(\omega) - \varepsilon''(\omega) = \varepsilon_\infty + \sum_{j=1}^{n} \frac{\Delta\varepsilon_j \omega_j^2}{\omega_j^2 - \omega^2 + i\omega\gamma_j} \tag{2.4}$$

where ω_j , γ_j and $\Delta\varepsilon_j$ denote the frequency, damping and contribution to the static permittivity of the j^{th} polar mode, respectively, and ε_∞ stands for the high-frequency permittivity originating from the electronic polarization and from polar phonons above the spectral range studied; n denotes number of excitations in the measured spectrum.

The transmission spectra of PMN thin film were fitted using the model (2.4). The $\varepsilon(\omega)$ spectra were then calculated from these fits. Figure 2.5 shows these spectra at different temperatures up to $100\,\mathrm{cm}^{-1}$. In this frequency range, the SM and the THz part of the CM are present. The higher-frequency modes were practically temperature-independent; their frequencies were found to be above $150\,\mathrm{cm}^{-1}$. The temperature dependence of the SM and CM are shown in figure 2.6a. The CM is overdamped, therefore the relaxation frequency (corresponding to the loss maximum $\omega_{CM}^2/\gamma_{CM}$) is plotted [Kamba 05a].

The ferroelectric-to-relaxor crossover, and its connection to the degree of ordering of the B-site occupancy, can be illustrated on a mixed compound $Pb(Sc_{1/2}Ta_{1/2})O_3$ (PST). The degree of order in the lattice is controlled during the preparation of the samples (by varying the temperature and time of annealing). The temperature dependence of the polar mode frequencies of disordered PST film is qualitatively comparable to that of e.g. PMN (figure 2.6b), while in the ordered sample (figure 2.6c), another mode appears below T_m in the spectra near $60\,\mathrm{cm}^{-1}$ (7.5 meV) [Kamba 05b]. This excitation appears in the disordered sample only below 100 K, and not at higher temperatures due to the line broadening compared to the ordered film.

From figure 2.6a we can see that the A_1(TO1) soft mode component follows the Cochran law, with the extrapolated critical temperature close to

---

[2] We used thin films of thickness 500 nm on sapphire substrate (transparent in the far IR range) instead of single crystals, because the latter are opaque in the far IR range, mainly due to strong absorption from polar modes, down to thicknesses of $1\,\mu$m.

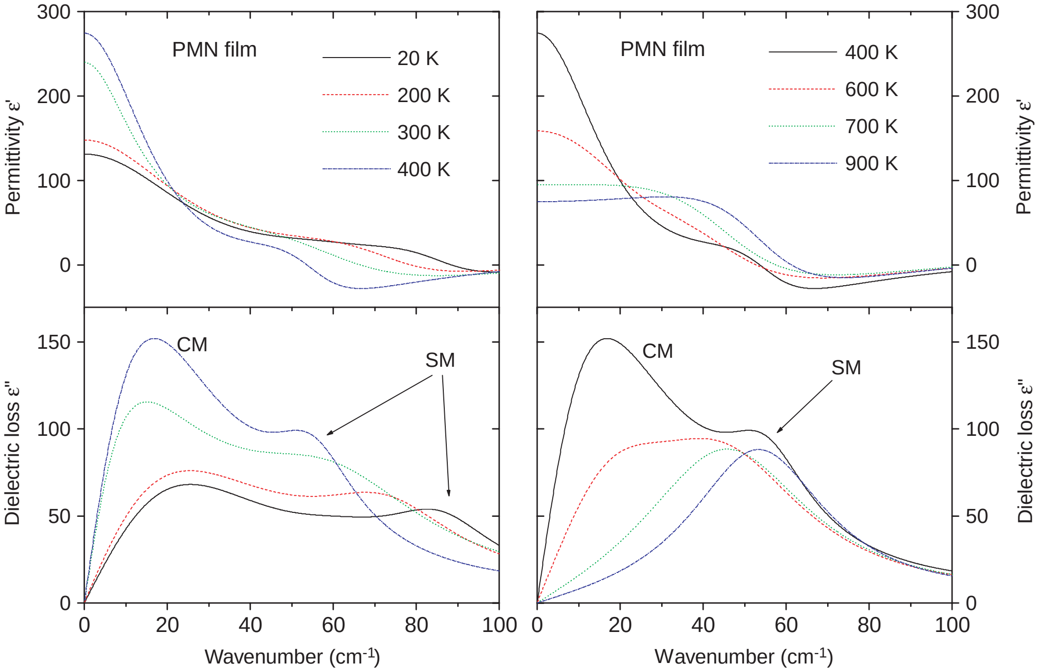

Figure 2.5: Complex dielectric spectra of PMN thin film obtained from the fits of far IR transmission spectra at various temperatures.

the Burns temperature of the PMN single crystal (620 K, figure 2.6a). The fact that the SM (partially) softens towards the Burns temperature instead of T_m or T_{VF}, indicates that it represents the ferroelectric SM inside the polar nanoregions [Kamba 05c]. This observation, however, does not put any constraints on the shape of PNRs, their size or the volume fraction of the material that they fill [Hlinka 06c].

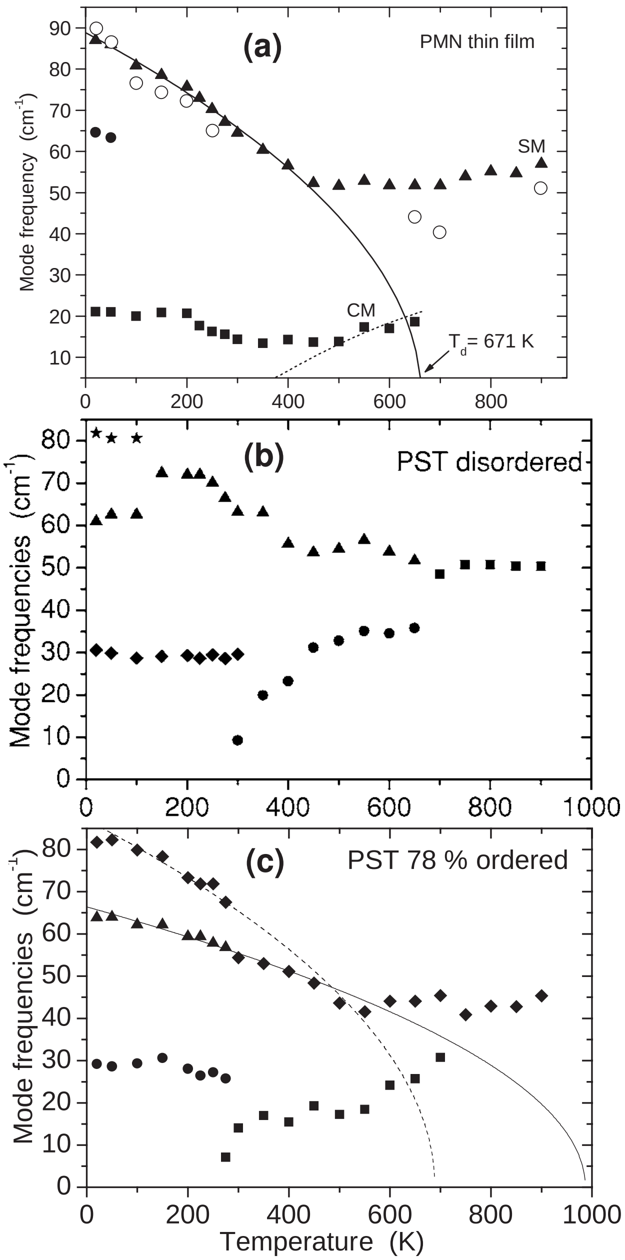

Figure 2.6: (a): Temperature dependence of the SM and CM frequencies of PMN. Solid and open points: modes obtained from far IR transmission [Kamba 05a] and INS [Wakimoto 02a] spectra, respectively. The Cochran fit [equation (2.2)] of the SM is shown by the solid line; the slowing down of the CM is shown schematically by the dashed line; (b) and (c): Temperature dependence of the polar mode frequencies of disordered and ordered PST films, respectively [Kamba 05b].

Chapter 3

Neutron Scattering

Concerning this thesis, most of the results have been obtained with inelastic neutron scattering (INS), particularly three-axis spectroscopy (TAS). This method is complementary to spectroscopic methods, in particular infra-red (IR) and Raman spectroscopies; the principles of these methods are not described in the thesis. In this chapter, we will briefly summarize the properties of neutrons and the principle of neutron scattering; in the next chapter, the three-axis spectroscopy and the new *FlatCone* multianalyzer for TAS will be described.

Neutron scattering is an experimental method used in many fields of science (to study crystal structures, magnetic structures, excitations, polymers; in biology, environmental sciences, engineering and many others). Lattice dynamics of crystalline solids is one of the examples where INS gives very useful (and in some cases unique) information.

Information contained in the following sections was drawn mainly from these sources: [Squires 78, Lovesey], presentations of Jiri Kulda (ILL) and from the HERCULES course [Hercules].

3.1 Fundamental properties of the neutron

Neutrons are elementary particles, which together with protons form a part of nuclei. A neutron has a mass $m_n \doteq 1.008665\,\mathrm{a.u.} \doteq 1.675.10^{-27}\,\mathrm{kg}$, zero charge (according to latest studies, $q < 10^{-21}e$), spin 1/2 and magnetic dipole moment $\mu_n \doteq 1.913$ nuclear magnetons. As a free particle, it decays with a half time $\tau_n \doteq 615\,\mathrm{s}$, thus allowing to perform a scattering experiment (which typically lasts much less than 1 s).

Neutrons as elementary particles show both wave and particle properties, as summarized in table 3.1. Both these properties are used in practice for

	particle	wave
energy	$E = m_n v^2/2$	$E = \hbar^2 k^2/(2m_n)$
momentum	$\vec{p} = m_n \vec{v}$	$\vec{p} = \hbar \vec{k}$

Table 3.1: Duality properties of the neutron; m_n is the neutron mass, v its velocity, and $\vec{k}$ is the wave vector (the wave number is given by $k = 2\pi/\lambda$, λ denoting the de Broglie wavelength).

analyzing the neutron beam (by diffraction and time-of-flight, respectively; see section 4).

Typical values for thermal neutrons (here, as an example, at room temperature) are: Kinetic energy $k_B T \approx 25\,\mathrm{meV}$, velocity $v \approx 2200\,\mathrm{m.s}^{-1}$, de Broglie wavelength $\lambda \approx 1.8\,\text{Å}$.

3.2 Neutrons in the scattering experiment

The neutrons coming out from the nuclear reactor are created by fission[1]

$$\mathrm{n} +^{235} \mathrm{U} \rightarrow 2 \text{ nuclei} + 2.5\,\mathrm{n} + \text{Energy} \tag{3.1}$$

The neutron flux depends on the thermal power of the reactor, and in most neutron reactors exceeds $10^{14}/\mathrm{cm}^{-2}\mathrm{s}^{-1}$. Because the neutrons from the reactor are very energetic (or fast, $v \approx 20000\,\mathrm{km.s}^{-1}$, moderation is necessary before the experiment, in order to obtain hot ($v \approx 10\,\mathrm{km.s}^{-1}$), thermal ($v \approx 2\,\mathrm{km.s}^{-1}$) or cold ($v \approx 10\,\mathrm{m.s}^{-1}$) secondary neutron sources (cf. figure 3.1).

Slowing down (moderation) is usually provided by heavy water D_2O (thanks to relatively high σ_{coh} and negligible σ_{inc} - see section 3.3), biological shielding by water H_2O (easily accessible, with high σ_{inc}).

After the scattering experiment, the neutrons have to be detected. Neutral particles must be converted to charged ones, so that they can be easily counted. On TAS instruments, detectors are usually tubes filled with ^{3}He gas, where the reaction

$$\mathrm{n} +^{3}\mathrm{He} \rightarrow \mathrm{p} +^{3}\mathrm{T}$$

is performed, charged particles are accelerated to electrodes and detected.

---

[1] We do not describe here the aspects of pulsed (spallation) sources; however, in the case of INS there is no much difference between reactors and spallation sources, as we detect the intensity of scattered neutrons continuously. Also the moderation of neutrons described below is similar.

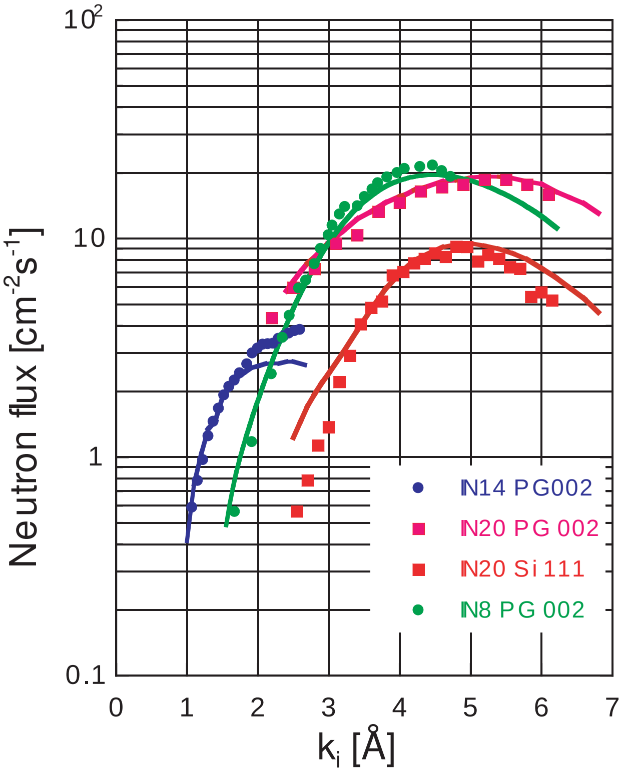

Figure 3.1: The dependence of the neutron flux on the wave number, for the cold (IN14) and thermal (IN8, IN20) instruments at the ILL. The dependence of the flux on the neutron energy is close to Maxwellian (for thermal neutrons, $E \approx 2k^2$). Graph taken from [Saroun 00].

3.3 Neutron scattering

Nuclear scattering of neutrons by an ensemble of nuclei is realized by strong interaction between a neutron and a nucleus. This interaction, however, is weak by intensity, and is well described by the so-called Fermi pseudopotential

$$V\left(\vec{r}\right) = \frac{2\pi\hbar^2}{m_n}\, b\, \delta\left(\vec{r} - \vec{R}\right) \, , \tag{3.2}$$

in fact a delta-function at the position $\vec{R}$ of the nucleus, multiplied by a constant[2]. The quantity b, called neutron scattering length, is specific for each nucleus (isotope), and randomly dependent on atomic number (contrary to X-rays). b is generally complex. Its real part is positive for most atoms, which corresponds to a repulsive interaction of neutrons and nuclei.

The differential scattering cross-section $\mathrm{d}\sigma/\mathrm{d}\Omega$ is defined as number of neutrons scattered per second into a small solid angle $\mathrm{d}\Omega$ in a chosen direction, divided by $\Phi\mathrm{d}\Omega$, where Φ is the flux of incident neutrons. Introducing the scattering vector (neutron momentum transfer)

$$\vec{Q} = \vec{k}_f - \vec{k}_i \, , \tag{3.3}$$

where $\vec{k}_i$ and $\vec{k}_f$ are the wave vectors of the incident and scattered neutron, respectively, $\mathrm{d}\sigma/\mathrm{d}\Omega$ from a single nucleus can be written in a form

$$\frac{\mathrm{d}\sigma}{\mathrm{d}\Omega} = \left(\frac{m_n}{2\pi\hbar^2}\right)^2 \left| \int_{-\infty}^{\infty} V\left(\vec{r}\right) \exp\left[i\,\vec{Q}\cdot\vec{r}\right] \mathrm{d}\vec{r} \right|^2 \tag{3.4}$$

which is isotropic (s-wave) for b $\ll \lambda$ and results in total scattering cross-section from a single nucleus

$$\sigma = 4\pi b^2 \, . \tag{3.5}$$

If we consider the whole ensemble of nuclei, we get (N is the number of nuclei in the scattering system)

$$V\left(\vec{r}\right) = \frac{2\pi\hbar^2}{m_n} \sum_{j=1}^{N} b_j\, \delta\left(\vec{r} - \vec{R}_j\right) \, . \tag{3.6}$$

The positions of the nuclei $\vec{R}_j = \vec{R}_j(t)$ are generally time-dependent.

---

[2] The constant was chosen in such a way that the total scattering cross-section from a single nucleus (equation 3.5) corresponds to quantum-mechanical scattering by a rigid sphere.

$\mathrm{d}\sigma/\mathrm{d}\Omega$ corresponding to transitions of the scattering system from state λ_i to λ_f is, following its definition and applying the Fermi's golden rule, given by

$$\left(\frac{\mathrm{d}\sigma}{\mathrm{d}\Omega}\right)_{\lambda_i\to\lambda_f} = \frac{1}{\Phi}\frac{1}{\mathrm{d}\Omega}\frac{2\pi}{\hbar}\rho_{\vec{k}_f}\left|\left\langle\vec{k}_f\lambda_f|V|\vec{k}_i\lambda_i\right\rangle\right|^2 \tag{3.7}$$

where $\rho_{\vec{k}_f}$ is the number of states for neutrons with momentum $\vec{k}_f$ in $\mathrm{d}\Omega$ per unit energy. After performing the box normalization, and considering incident and scattered neutrons as plane waves (for details se e.g. [Squires 78]), we get

$$\left(\frac{\mathrm{d}\sigma}{\mathrm{d}\Omega}\right)_{\lambda_i\to\lambda_f} = \frac{k_f}{k_i}\left(\frac{m_n}{2\pi\hbar^2}\right)^2\left|\left\langle\vec{k}_f\lambda_f|V|\vec{k}_i\lambda_i\right\rangle\right|^2 \,. \tag{3.8}$$

For fixed $\lambda_i, \lambda_f \mathrm{and} \vec{k}_i$, the value of k_f (and hence E_f) is already determined. Then the double-differential cross-section is defined as $\mathrm{d}\sigma/\mathrm{d}\Omega$ of neutrons with final energy between E_f and $E_f + \mathrm{d}E_f$. In a scattering experiment, we are not able to distinguish between particular states λ_i, λ_f of the system. Therefore we have to sum over all λ_f at a fixed λ_i, and then average over λ_i. Finally we obtain (see again [Squires 78]):

$$\frac{\mathrm{d}^2\sigma}{\mathrm{d}\Omega\,\mathrm{d}E_f} = \frac{k_f}{k_i}\frac{1}{2\pi\hbar}\sum_{jj'}\int_{-\infty}^{\infty}\left\langle\exp\left[-i\,\vec{Q}\cdot\vec{R}_{j'}(0)\right]\exp\left[i\,\vec{Q}\cdot\vec{R}_j(t)\right]\right\rangle e^{i\omega t}\mathrm{d}t\,. \tag{3.9}$$

It is useful to divide the scattering into two parts - coherent and incoherent:

$$\left(\frac{\mathrm{d}^2\sigma}{\mathrm{d}\Omega\,\mathrm{d}E_f}\right)_{coh} = \frac{\sigma_{coh}}{4\pi}\frac{k_f}{k_i}\frac{1}{2\pi\hbar}\sum_{jj'}\int_{-\infty}^{\infty}\left\langle\exp\left[-i\,\vec{Q}\cdot\vec{R}_{j'}(0)\right]\exp\left[i\,\vec{Q}\cdot\vec{R}_j(t)\right]\right\rangle e^{i\omega t}\mathrm{d}t \tag{3.10}$$

$$\left(\frac{\mathrm{d}^2\sigma}{\mathrm{d}\Omega\,\mathrm{d}E_f}\right)_{inc} = \frac{\sigma_{inc}}{4\pi}\frac{k_f}{k_i}\frac{1}{2\pi\hbar}\sum_{j}\int_{-\infty}^{\infty}\left\langle\exp\left[-i\,\vec{Q}\cdot\vec{R}_{j}(0)\right]\exp\left[i\,\vec{Q}\cdot\vec{R}_j(t)\right]\right\rangle e^{i\omega t}\mathrm{d}t \tag{3.11}$$

where

$$\sigma_{coh} = 4\pi\langle b\rangle^2\,, \tag{3.12}$$

$$\sigma_{inc} = 4\pi\left(\langle b^2\rangle - \langle b\rangle^2\right)\,. \tag{3.13}$$

The coherent scattering cross-section describes the correlations between the positions of nuclei at different times (including self-correlation); the incoherent part corresponds only to the correlation between the positions of the same nucleus at different times.

Although the incoherent scattering can be useful in various experiments, or during alignments and tests, it usually forms noise or even overlaps the desired signal coming from collective excitations, such as phonons. See also section 4.4. The widely used incoherent scatterer is vanadium, employed for alignments, calibration and for determination of the energy resolution of the instrument.

The neutron beam is generally being attenuated when passing through matter. Attenuation could play an important role during the scattering process, especially in strongly absorbing samples.

The optical theorem says that the scattering length of an isotope can be written in a form

$$b = b_0 + b' + ib'' \tag{3.14}$$

The real part $b_0 + b'$ describes scattering by the rigid sphere and resonant scattering, respectively. The imaginary part

$$b'' = \sigma_{tot} / (2\lambda) = (\sigma_{coh} + \sigma_{inc} + \sigma_{abs}) / (2\lambda)$$

is the total scattering cross-section (i.e. comprising coherent + incoherent scattering and absorption), represents the strength of attenuation of neutrons with wavelength λ. The attenuation coefficient is given by

$$\mu \, [\mathrm{cm}^{-1}] = N \sigma_{tot} \, . \tag{3.15}$$

The attenuation of neutron flux due to attenuation in a slab of thickness d is then

$$I = I_0 \, e^{-\mu d} \, . \tag{3.16}$$

For example, for PZN, $\mu = 0.465 \, \mathrm{cm}^{-1}$ (i.e. loss of 20% intensity on 5 mm), and similarly for PMN and related systems.

3.4 Inelastic neutron scattering

In the case of a crystal lattice, the positions of nuclei are labelled within the unit cell:

$$\vec{R}_j(t) = \vec{l} + \vec{u}_j(t) \ , \tag{3.17}$$

where $\vec{l}$ stands for the position of the unit cell, and $\vec{u}_j(t)$ is the displacement of the j-th nucleus from its equilibrium position. The coherent scattering amplitude from equation 3.10 can be then re-written as

$$\begin{aligned} \left\langle \exp\left[-i\,\vec{Q}\cdot\vec{R}_{j'}(0)\right] \exp\left[i\,\vec{Q}\cdot\vec{R}_j(t)\right] \right\rangle &= \left\langle \exp\left[-i\,\vec{Q}\cdot\vec{u}_0(0)\right] \exp\left[i\,\vec{Q}\cdot\vec{u}_j(t)\right] \right\rangle \\ &= \exp\left\langle \left[\vec{Q}\cdot\vec{u}_0(0)\right]^2 \right\rangle \exp\left\langle \left[\vec{Q}\cdot\vec{u}_j(t)\ \vec{Q}\cdot\vec{u}_0(0)\right] \right\rangle . \end{aligned} \tag{3.18}$$

The first part on the right-hand side is the Debye-Waller temperature factor which gives loss of intensity of Bragg diffraction due to thermal vibrations (see below). The second part is coherent scattering, which generally contains n-phonon contributions, $n \geq 0$:

$$\exp\left\langle\left[\vec{Q}\cdot\vec{u}_j(t)\ \vec{Q}\cdot\vec{u}_0(0)\right]\right\rangle = 1 + \left\langle\left[\vec{Q}\cdot\vec{u}_j(t)\ \vec{Q}\cdot\vec{u}_0(0)\right]\right\rangle + \frac{1}{2}\left\langle\left[\vec{Q}\cdot\vec{u}_j(t)\ \vec{Q}\cdot\vec{u}_0(0)\right]\right\rangle^2 + \ldots + \frac{1}{n!}\left\langle\left[\vec{Q}\cdot\vec{u}_j(t)\ \vec{Q}\cdot\vec{u}_0(0)\right]\right\rangle^n + \ldots . \tag{3.19}$$

The first term, the number one, represents elastic scattering. The second term is single-phonon scattering, which we will almost exclusively deal with, as a useful signal from which the physical information can be easily extracted.

In the particular case of (thermal) lattice vibrations, the coherent scattering cross-section can be adapted into a form directly applicable for the evaluation of the experiment.

Let us consider a model of a set of the equations of motion of the atoms in the crystal (in harmonic approximation)

$$m_{\vec{d}}\,\ddot{u}_\alpha\left(\vec{l}\,\vec{d}\right) = -\sum_{\vec{l}'\vec{d}',\beta} \Phi_{\alpha\beta}\left(\vec{l}\,\vec{d},\vec{l}'\vec{d}'\right) u_\beta\left(\vec{l}'\vec{d}'\right) , \tag{3.20}$$

where $u_\alpha\left(\vec{l}\,\vec{d}\right)$ is the displacement amplitude of the d-th atom with the mass $m_{\vec{d}}$ in the l-th unit cell in the cartesian α direction

$$u_\alpha\left(\vec{l}\,\vec{d}\right) = \frac{1}{\sqrt{m_{\vec{d}}}}\sum_{\vec{q}} U_\alpha\left(\vec{q},\vec{d}\right)\exp\left[i\left(\vec{q}\,\vec{l}-\omega t\right)\right], \tag{3.21}$$

and $\Phi_{\alpha\beta}$ are double partial derivatives of the potential of nuclei with respect to the displacements in equilibrium.

The solution of the set 3.20 leads to the condition

$$\left|D_{\alpha\beta}\left(\vec{d}\,\vec{d}'|\vec{q}\right) - \omega^2\delta_{\alpha\beta}\,\delta\left(\vec{d}-\vec{d}'\right)\right| = 0\,, \tag{3.22}$$

where $D_{\alpha\beta}\left(\vec{d}\,\vec{d}'|\vec{q}\right)$ is the dynamical matrix of the lattice. The eigenvalues ω_s of the matrix are the eigenfrequencies of the lattice, corresponding to eigenvectors $\vec{e}_{\vec{d}s}$.

Then the one-phonon part of equation 3.10 turns in

$$\left(\frac{\mathrm{d}^2\sigma}{\mathrm{d}\Omega\,\mathrm{d}\omega}\right)^1_{coh} = \frac{k_f}{k_i}\frac{(2\pi)^3}{2v_0}\sum_s\frac{\langle n_s+1\rangle}{\omega_s}\left|\sum_{\vec{d}}\frac{b_{\vec{d}}}{\sqrt{m_{\vec{d}}}}\left(\vec{Q}\cdot\vec{e}_{\vec{d}s}\right)\exp\left(-W_d\right)\exp\left(i\vec{Q}\cdot\vec{d}\right)\right|^2$$

$$\times\delta\left(\omega-\omega_s\right)\,\delta\left(\vec{Q}-\vec{q}-\vec{\tau}\right)\,. \tag{3.23}$$

In the last equation, v_0 is the volume of the unit cell, and $\langle n_s\rangle$ is the Bose temperature factor

$$\langle n_s\rangle=\frac{1}{\exp\left(\frac{\hbar\omega_s}{kT}\right)-1}\,. \tag{3.24}$$

The term in absolute value squared is the inelastic structure factor

$$F=\sum_{\vec{d}}\frac{b_{\vec{d}}}{\sqrt{m_{\vec{d}}}}\left(\vec{Q}\cdot\vec{e}_{\vec{d}s}\right)\exp\left(-W_d\right)\exp\left(i\vec{Q}\cdot\vec{d}\right) \tag{3.25}$$

which contains information on topology of displacement pattern (through the excitation eigenvectors $\vec{e}_{\vec{d}s}$, which are generally complex). However, because in the INS experiment we measure the scattering cross-section, we directly obtain only the magnitude of F.

As follows from equation 3.23, the scattering intensity increases as Q^2, even though moderated by the Debye-Waller factor at larger Q.

To summarize the properties of inelastic neutron scattering, its main advantages are the consequences of neutron properties :

- neutrons penetrate most of the materials (orders of magnitude better than e.g. X-rays or electrons); on the other hand, it is not so easy to provide detection and shielding.

- neutrons are non-destructive to materials (at the fluxes and times of exposure usual at neutron reactors).

- the interaction with elements (isotopes) is “randomly selective”, which results in contrast variation (differentiation of elements nearby in the periodic table, or of isotopes of the same element; the most important examples are hydrogen and deuterium).

- neutrons possess a magnetic dipole moment, so in principle one can separate the nuclear and magnetic signals; in this thesis, we do not deal with magnetic scattering.

- the kinetic energy E of thermal neutrons is of the order of k_BT, and hence of the order of typical thermal excitation energies in solids. INS can in principle be used in the range of energies $20\,\mu$eV–200 meV, while the resolution in energy transfer is typically 5–10%.

- by INS, in principle, we can access any position $\vec{Q}$ in the reciprocal space (although in practice we are of course limited by some maximum value Q_{max} and by “forbidden areas”, given by the properties and geometry of the instrument and by the flux distribution). That means, contrary to e.g. optical methods, we obtain $\vec{Q}$-dependent properties; in case of single crystals e.g. dispersion relations.

Chapter 4

Neutron Instrumentation

4.1 Principle of INS

The principle of an inelastic neutron scattering (INS) experiment is to collect data in a chosen direction (area) of the 4-dimensional reciprocal space $(\vec{Q}, E)$. In particular, we want to determine the scattering function $S(\vec{Q}, E)$, containing information about the sample, which is directly connected to the double-differential scattering cross-section (see equation 3.23):

$$\frac{\mathrm{d}^2\sigma}{\mathrm{d}\Omega\,\mathrm{d}E} = \frac{k_f}{k_i}\, b_c^2\, S(\vec{Q}, E) \otimes R(\vec{Q}, E)\,, \tag{4.1}$$

where $R(\vec{Q}, E)$ is the resolution function of the instrument, convoluted with $S(\vec{Q}, E)$. Spectroscopically, $S(\vec{Q}, E)$ corresponds to the imaginary part of the generalized susceptibility

$$S(\vec{Q}, E) = \frac{\chi''}{1 - e^{-E/k_B T}} \tag{4.2}$$

(in the case of one-phonon dielectric susceptibility, it is directly linked with permittivity: $\varepsilon'' \propto \chi''$).

$S(\vec{Q}, E)$ also obeys the fluctuation-dissipation theorem

$$S(-\vec{Q}, -E) = S(\vec{Q}, E)\, e^{-E/k_B T} \tag{4.3}$$

which is important for choosing the sign of energy transfer (energy gain or loss of the neutrons) for the experiment: in the case of energy gain ($-E$ within our convention), the measured intensity is much smaller due to the exponential factor (especially at low temperatures and higher energies).

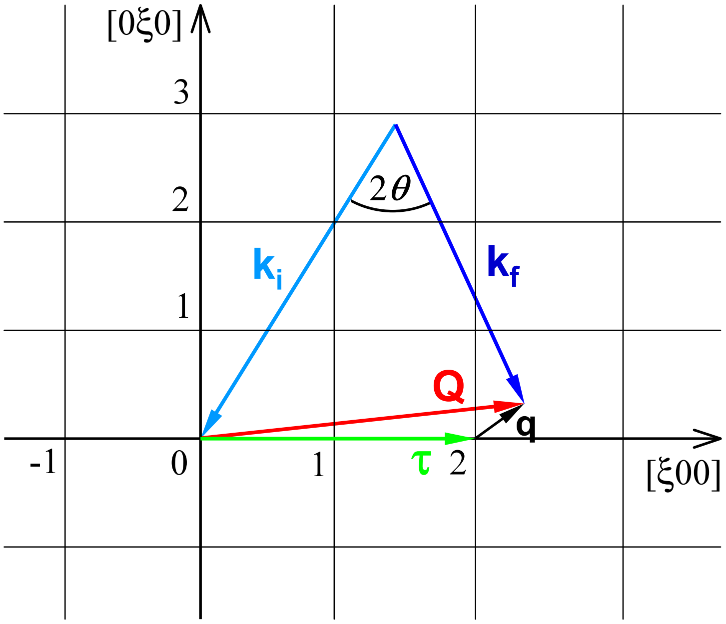

Figure 4.1: Schematic drawing of a scattering triangle in the scattering plane of an orthorhombic lattice; θ is the scattering angle.

As follows directly from equation 3.23, the neutron scattering process must fulfill conservation laws of the momentum and energy transfers in the form[1]

$$\vec{Q} = \vec{k}_f - \vec{k}_i \,, \tag{4.4}$$

$$\Delta E = \frac{\hbar^2}{2m_n} k_i^2 - k_f^2 \,. \tag{4.5}$$

As a consequence, a scattering process is possible only if the scattering triangle (figure 4.1) in the scattering plane can be closed.

By convention, the incident wave vector $\vec{k}_i$ points to the origin of the reciprocal space. If we choose the scattering vector $\vec{Q}$ and energy transfer E, the scattering triangle is unambiguously determined by equations 4.4,4.5. Concerning the determination of E, two main principles are used: the determination by time-of flight (TOF spectrometers) and by diffraction (TAS spectrometers).

---

[1] In practice, these equations are to be fulfilled only within the finite resolution of the particular settings of the instrument.

4.2 Time-of-flight spectroscopy

The TOF spectroscopy is not in the scope of this thesis, therefore we will only briefly mention its principle, as it is an INS method complementary to three-axis spectroscopy. In this section, the terms neutron energy and velocity are considered to be equivalent.

The time-of-flight (TOF) technique takes advantage of the particle properties of neutrons. Generally speaking, energy of the neutrons is being distinguished during the scattering experiment by their velocity (i.e. by the time they need to reach the sample/detector). The velocity of thermal neutrons is of the order of km.s^{-1} (section 3.1), so their energy can be determined by measuring the time of flight over a distance of a few meters.

In the case of a continuous neutron beam, we are in principle not able to differentiate between a faster and a slower neutron, the latter scattered earlier by the sample, if they arrive at the detector at the same time. In order to be able to separate the slower and faster neutrons coming to the detector, the neutron beam has to be chopped[2] into bunches of a defined velocity, with a large enough distance between them. This process is usually performed by the system of choppers (e.g. Fermi choppers or disk choppers, see figure 4.2).

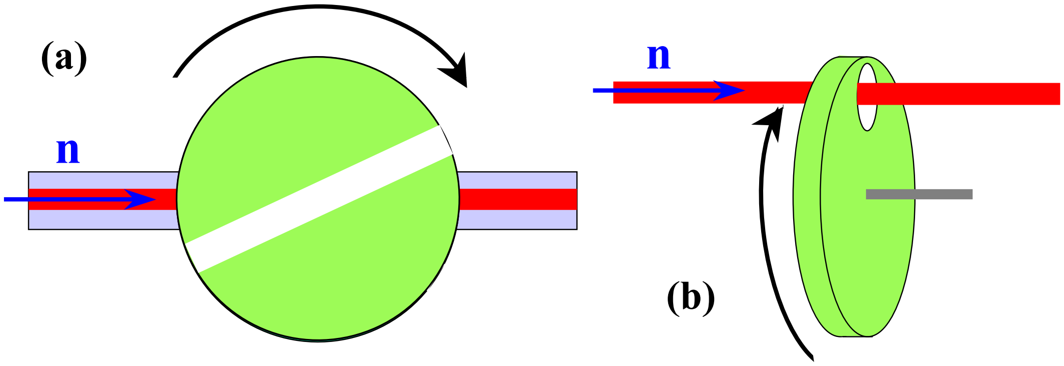

Figure 4.2: Schematic plot of (a) the Fermi chopper, (b) the disk chopper.

Time-of-flight spectrometers may be divided into two classes:

- Direct geometry spectrometers - the incident energy E_i is defined by a chopper (or crystal), and the final energy E_f is determined by time of flight.

---

[2] Pulsed sources already provide a naturally chopped beam, so the TOF spectrometers there do not have to use choppers. On the other hand, choppers are essential on steady-state sources, which then serve as pulsing devices.

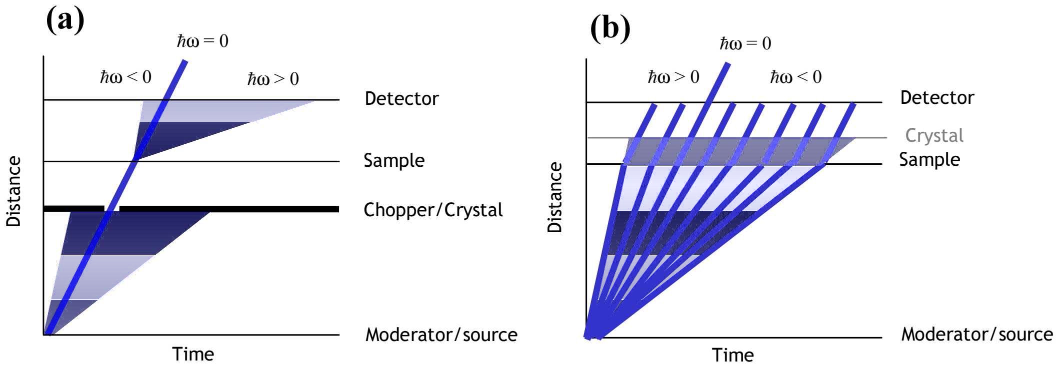

Figure 4.3: Distance-time diagrams of (a) direct and (b) indirect TOF geometry.

- Indirect geometry spectrometers - the beam incident on the sample is white (neither chopped nor monochromatized). E_f is defined by a crystal or filter and E_i is determined by time of flight.

Their principles are best understood from the distance-time diagrams (see figures 4.3a,b). In these plots, a line represents neutrons with the same velocity, and a triangle represents a polychromatic neutron beam "divergent" in time.

The corresponding scattering triangles are depicted in figures 4.4a,b for several energy transfers.

In the case of direct geometry spectrometers, large detector arrays are employed, giving simultaneous access to extended areas in the $S(\vec{Q}, E)$ space (see figure 4.13a as an example).

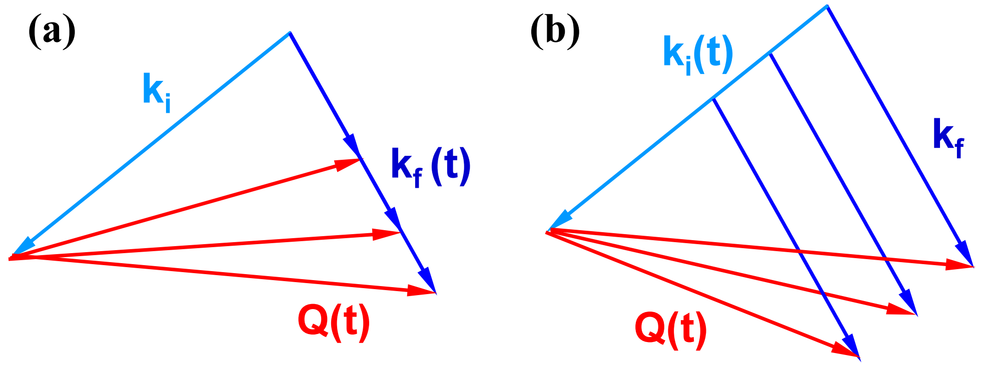

Figure 4.4: Schematic scattering triangles for the (a) direct and (b) indirect TOF geometry.

4.3 Three-axis spectroscopy

On a three-axis spectroscopy (TAS) instrument, the neutron energy is defined (analyzed) by the means of Bragg diffraction. This is performed twice for each neutron – before and after the scattering on the sample, so that we can determine the energy transfer in the scattering process. The measurement (in the case of a single-detector setup) then consists of scanning the 4-dimensional reciprocal space $(\vec{Q}, E)$ point by point in a chosen Brillouin zone (BZ) and direction of interest.

Prior to the experiment, the sample has to be aligned: one of the principal crystallographic axes of the sample is chosen to be vertical, and thus perpendicular to the incident neutron beam. Two other non-collinear axes, both perpendicular to the vertical axis, form the scattering plane. In the case of lattice vibrations, we can easily distinguish transverse and longitudinal phonon modes by choosing the right direction $\vec{Q}$ in the scattering plane, thus maximizing the structure factor 3.25 from one type of vibrations, i.e. maximizing the magnitude of the scalar product $\left(\vec{Q} \cdot \vec{e}_{\vec{d}s}\right)$.

The appellation "three-axis" points to three pairs of axes (at the monochromator, sample and analyzer) that can be set independently on the spectrometer. Choosing the $(\vec{Q}, E)$ point during the experiment then means to set the diffraction angles on monochromator and analyzer (to define energy transfer), the sample rotation angle ω and the scattering angle θ. The calculation of the angles from the $(\vec{Q}, E)$ coordinates and the positioning are done automatically at the instrument.

Three-axis spectroscopy (TAS) in its conventional configuration (with a single analyzer and detector) can be operated in two modes: constant-$\vec{Q}$ or constant-energy scanning in the chosen scattering plane (see figure 4.5). In general, const-$\vec{Q}$ scans are better when exploring "ordinary" dispersions, because, as a direct analogy to data from optical spectroscopy, the models on the basis of damped harmonic oscillators (DHOs) can be naturally applied to energy spectra. In some cases, however, the dispersions are very steep or containing some dips, so the const-$\vec{Q}$ spectra would only show very broad and unresolved features. Then it is better to "cut" the energy axis at a chosen value and to perform const-E scans, or even 2D mapping of the part of the scattering plane (see section 4.5).

In the case of const-$\vec{Q}$ scans, the energy transfer is changed, and consequently the magnitude of the incident wave vector $\vec{k}_i$ according to equation 4.5, simultaneously obeying equation 4.4. In the case of const-E scanning, the scattering vector $\vec{Q}$ is changed. Because the energy transfer is constant, the magnitude of $\vec{k}_i$ does not change.

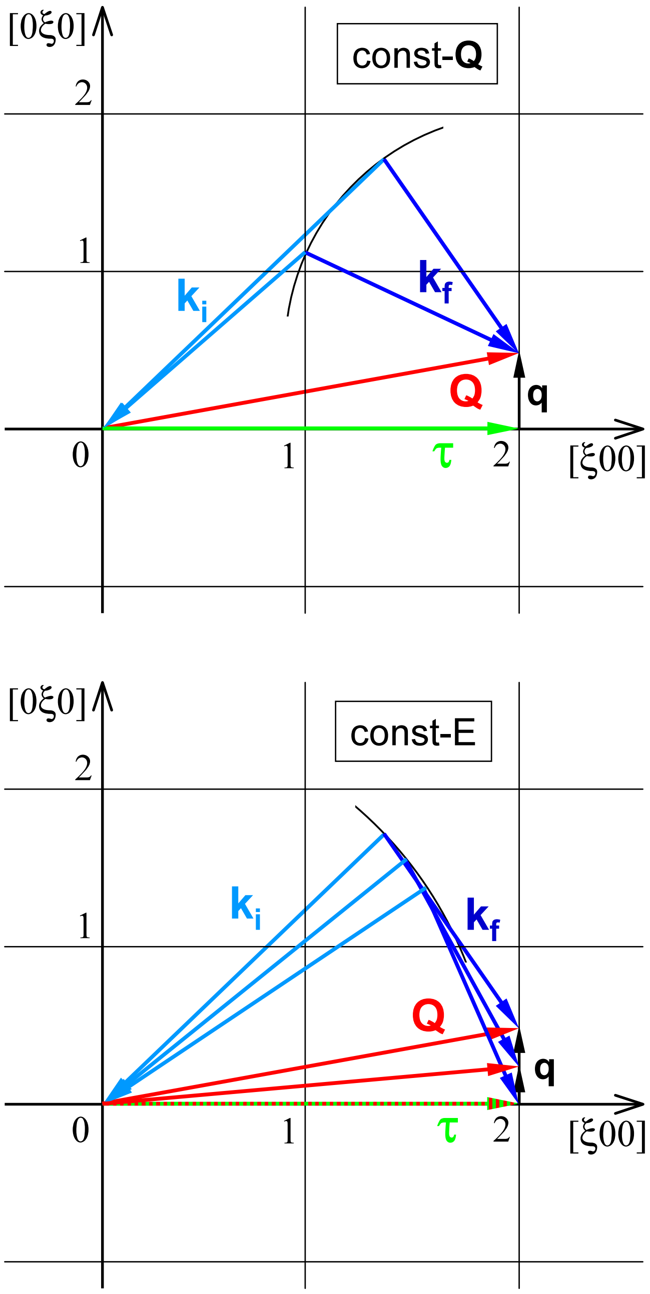

Figure 4.5: Schematic illustration of const-$\vec{Q}$ and const-E scanning (for an orthorhombic lattice and transverse geometry).

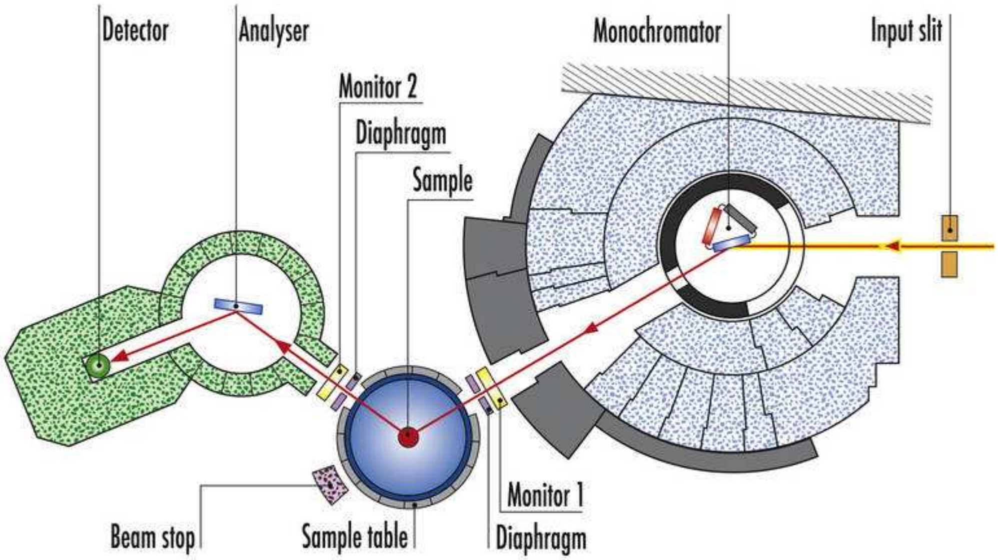

Figure 4.6: Top-view layout of the IN8 TAS instrument at the ILL; its components are described in the text. Copied from `http://www.ill.eu`

As examples of const-$\vec{Q}$ and const-E data, see figures 6.1 and 5.5, respectively.

The layout of a typical TAS instrument is depicted in figure 4.6. In this thesis, we will not go into details of the TAS instrumentation, which can be found e.g. in [Shirane 02]. Shortly, the way of the neutron beam is: secondary neutron source – monochromator – sample – analyzer – detector. The beam is defined by collimators and diaphragms (slits), and "cleaned" by filters of higher-order neutrons. The sample itself can be placed into various sample environments, such as cryostat, furnace, pressure cell or magnet. Monitors are in fact detectors with very low efficiency. Monitor 1 serves for the normalization of the neutron flux, whose intensity may vary in time; monitor 2 can reveal specific type of spurious (unwanted) Bragg scattering from the sample (see section 4.4).

The choice of the appropriate monochromator (and analyzer) crystal – its size, quality, lattice spacing d_{hkl}, potential bending and the crystal reflection – is the matter of the particular needs of the instrument and of the type of experiment. It is clear that the more perfect the crystal is, the better defined beam it reflects, however at the expense of the lower intensity. The resulting flux (see figure 3.1), degree of monochromatization and spatial divergence are different for crystals of different composition, structure and quality. For example, pyrolytic graphite with the (002) reflection (PG 002) gives higher total reflecting power than perfect bent silicon crystals with the (111) reflection (Si 111); however, in the first case, a filter of higher-order neutrons has to be used (Si 111 does not allow second-order contamination by symmetry[3]), therefore the useful monochromatized flux is lower for PG 002.

The TAS resolution function $R(\vec{Q}, E)$ is the property of the instrument (plus the mosaic spread of the sample). It is determined by the uncertainty in the incident energy (E_i) and scattered energy (E_f) and in the finite size of the solid angle $\mathrm{d}\omega$ from which the neutrons are detected. If we want to improve the resolution (e.g. by using more perfect monochromators or smaller detectors), we will pay for it by losing the intensity of the signal.

$R(\vec{Q}, E)$ can be represented by the so-called resolution ellipsoid, which reflects its (idealized) shape in $(\vec{Q}, E)$ space. The usual graphic representation of $R(\vec{Q}$,E) is then a 2D cut of the ellipsoid in chosen directions. With the progress in computing techniques, different approaches have been applied to calculate the resolution function. Probably the most important are the Cooper-Nathans method [Cooper 67], which neglects focussing and spatial effects (such as shapes and dimensions of the monochromators, sample and detector), and the Popovici method [Popovici 75], which takes these into account.

Figure 4.7 shows an example of the ellipsoid cuts calculated with the program RESTRAX [Kulda 96, Saroun 00], numerically (the Popovici method) by Monte Carlo simulation (dots) and analytically (the Cooper-Nathans method) within the Gaussian approximation (full lines – projections, dashed lines – sections). The coordinates have the following meanings: Q_X – in the direction of the beam, Q_Y – in the direction perpendicular to the beam (and in the horizontal plane), Q_Z – in the vertical direction.

When scanning dispersion curves, especially in the transverse geometry, it is favourable for the resulting spectrum that the resolution ellipsoid (its respective projection) is "laid" in the direction of the dispersion (see the red ellipsoids in figure 4.8a, contrary to the blue ones). Then the phonon group is focalized, viz. red data points in the figure 4.8b, in contrast to defocalized blue spectrum. In practice, however, the orientation of the ellipsoid in the $(\vec{Q}, E)$ space is given by the instrument setup; the way how to achieve focalization is to choose the appropriate one from equivalent directions in the Brillouin zone ($\pm q$, figure 4.8b)

---

[3] The (222) reflection is forbidden in the diamond structure.

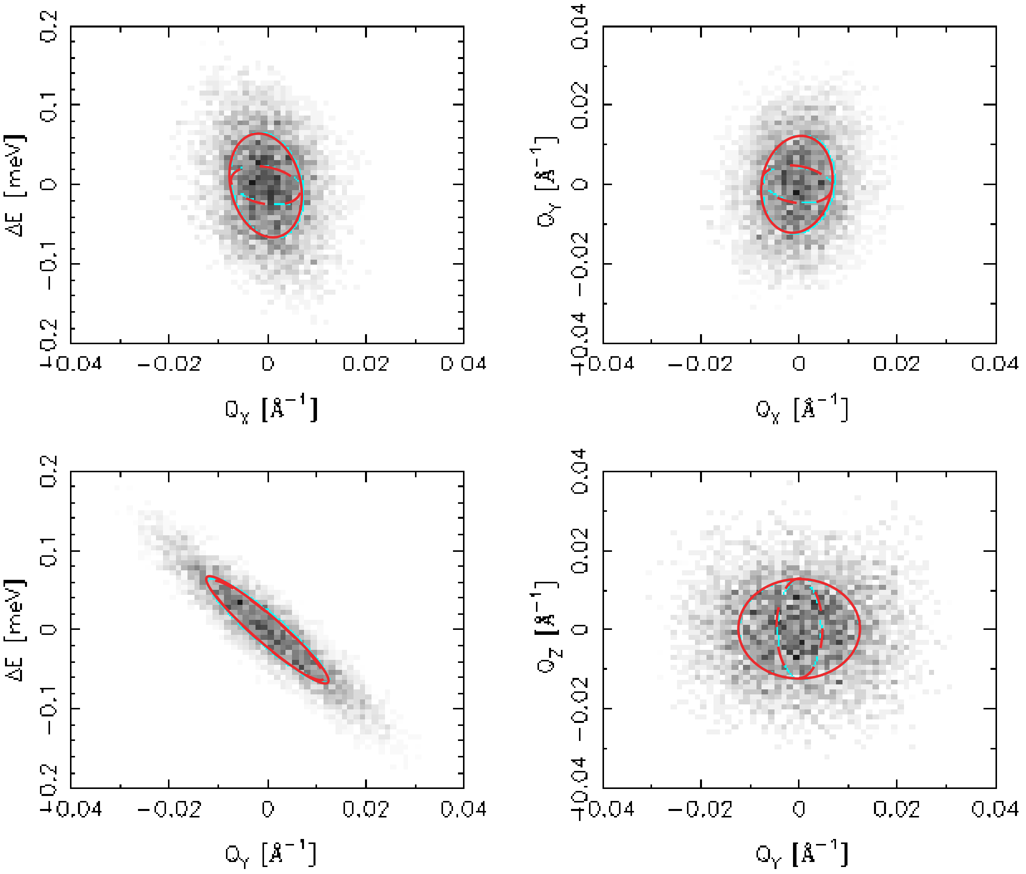

Figure 4.7: Example of projections of the resolution function calculated with RESTRAX [Kulda 96, Saroun 00]; numerically by Monte Carlo simulation (dots) and analytically within the approximation of gaussian beams (full lines – projections, dashed lines – sections).

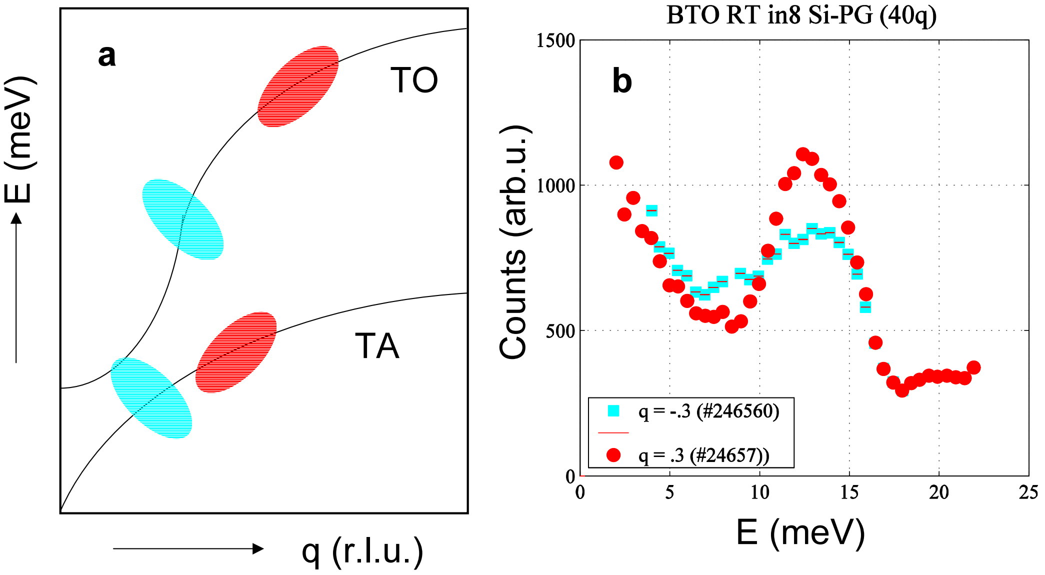

Figure 4.8: Left: Schematic plot of the orientation of the resolution ellipsoid with respect to the dispersion curves – focalized (red) and defocalized (blue). Right: Example of the spectrum of a transverse optic phonon measured in two equivalent directions from the BZ centre – focalized (red, $q = 0.3\,\mathrm{r.l.u.}$) and defocalized (blue, $q = -0.3\,\mathrm{r.l.u.}$).

4.4 Spurious signals

Quite exhaustive lists of types of spurious effects can be found e.g. in [Shirane 02] or on ILL webpages (`http://www.ill.eu/?id=1750`). In this section, we rather report on examples which we experienced during our INS studies.

As was already mentioned in section 3.4, the desired and most useful signal, in the case of lattice vibrations, comes from one-phonon coherent (inelastic) scattering (equation 3.19). In short, the rest of the scattering, coming into the detector, thus pretending to have been scattered from the sample in the intended way, is unwanted (spurious).

There are various types of the signal not desired in the experiment. Which is always present is the "true" **background**, i.e. general background in the reactor hall, and noise from detection electronics. This contribution is usually constant in INS spectra. To minimize the background, one could use better shielding of the analyzer and detector.

Higher-order contamination is a natural phenomenon that takes place at Bragg diffraction. Assuming that on monochromator, we want choose neutrons with energy E_i; to do this, the monochromator is set to reflect the neutrons from the (h, k, l) plane. At the same time, higher-order neutrons with energy $n^2 E_i$ are reflected from the (nh, nk, nl) plane, where $n > 1$ is integer. The same happens at the analyzer (generally of the order m). If these higher "harmonics" are scattered (with the elastic incoherent process), and if they fulfill the condition $n^2 E_i = m^2 E_f = m^2 E$, a "new" signal on energy transfer E will be detected. Usually, because of the distribution of the flux (figure 3.1), the biggest problem is second-order contamination (the higher orders should be negligible in most cases). This can be eliminated either by placing a filter before the analyzer (e.g. PG filter for PG 002 monochromators), which captures high-energy neutrons, or by using monochromators not allowing second-order reflections (e.g. Si 111) - see section 4.3.

The neutron beam can be **Bragg-scattered from the sample** (in the direction of the intended scattered beam), in combination with incoherent scattering from the monochromator or analyzer crystal. In this case, we can observe "dispersions" when changing $\vec{Q}$ or E (see figure 4.9a and 5.6), because the Bragg reflection on the sample simulates a non-zero energy transfer. The paths of this feature can be calculated from geometry, see figure 4.10. Monitor 2 (see section 4.3) can be very useful for uncovering the spurion of this type (cf. figure 4.9b). Usually we can get rid of this phenomenon (or at least shift it in $\vec{Q}$ and E away from the useful signal) by changing some of the parameters of the instrument (e.g. E_f in the fixed-E_f setup).

Because the resolution ellipsoid has finite size, its tail can "catch" some

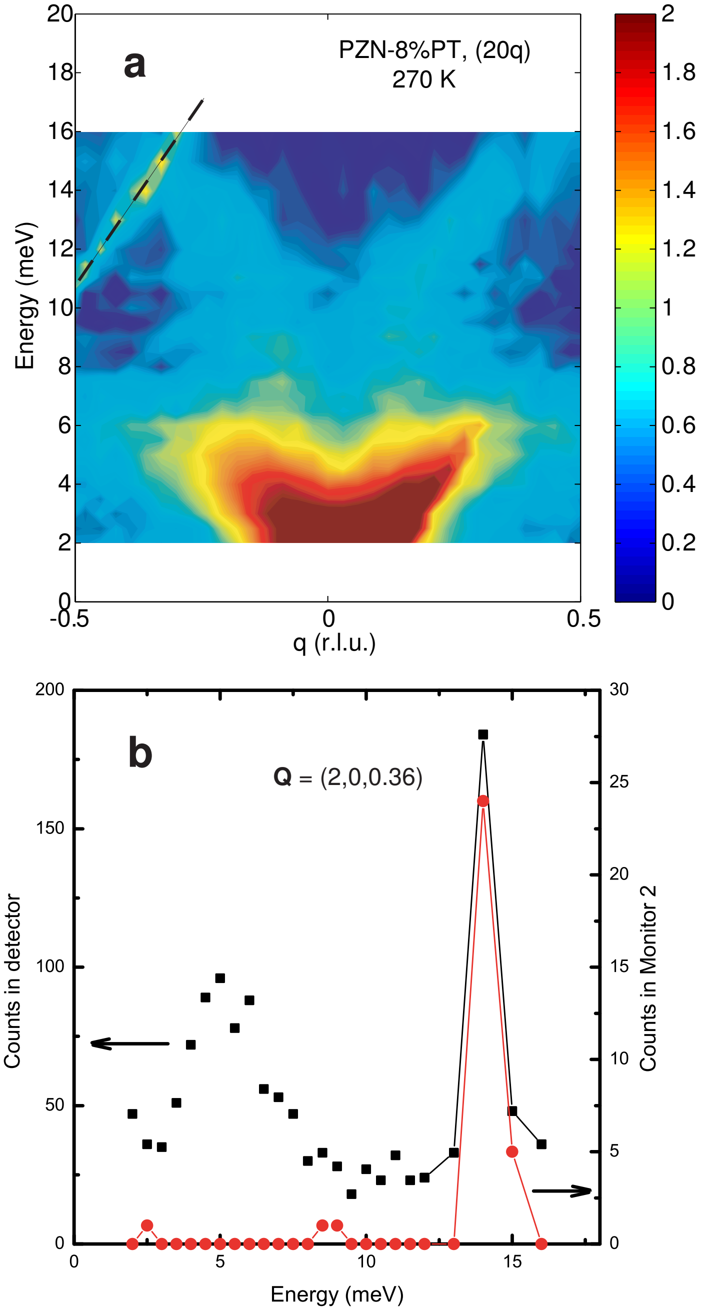

Figure 4.9: **a:** Intensity map of transverse dispersions in PZN–8%PT (see section 5) measured on the ILL's IN8 spectrometer. The spurious Bragg scattering is denoted by dashed line. The intensity scale is logarithmic. **b:** INS spectrum at $q = -0.36$ from panel a. The data (black squares, left axis), besides the TA phonon at 5 meV, reveal sharp signal at 14 meV. The intensity detected in monitor 2 (red circles, right axis) indicates that it is spurious. Lines are guides to the eye.

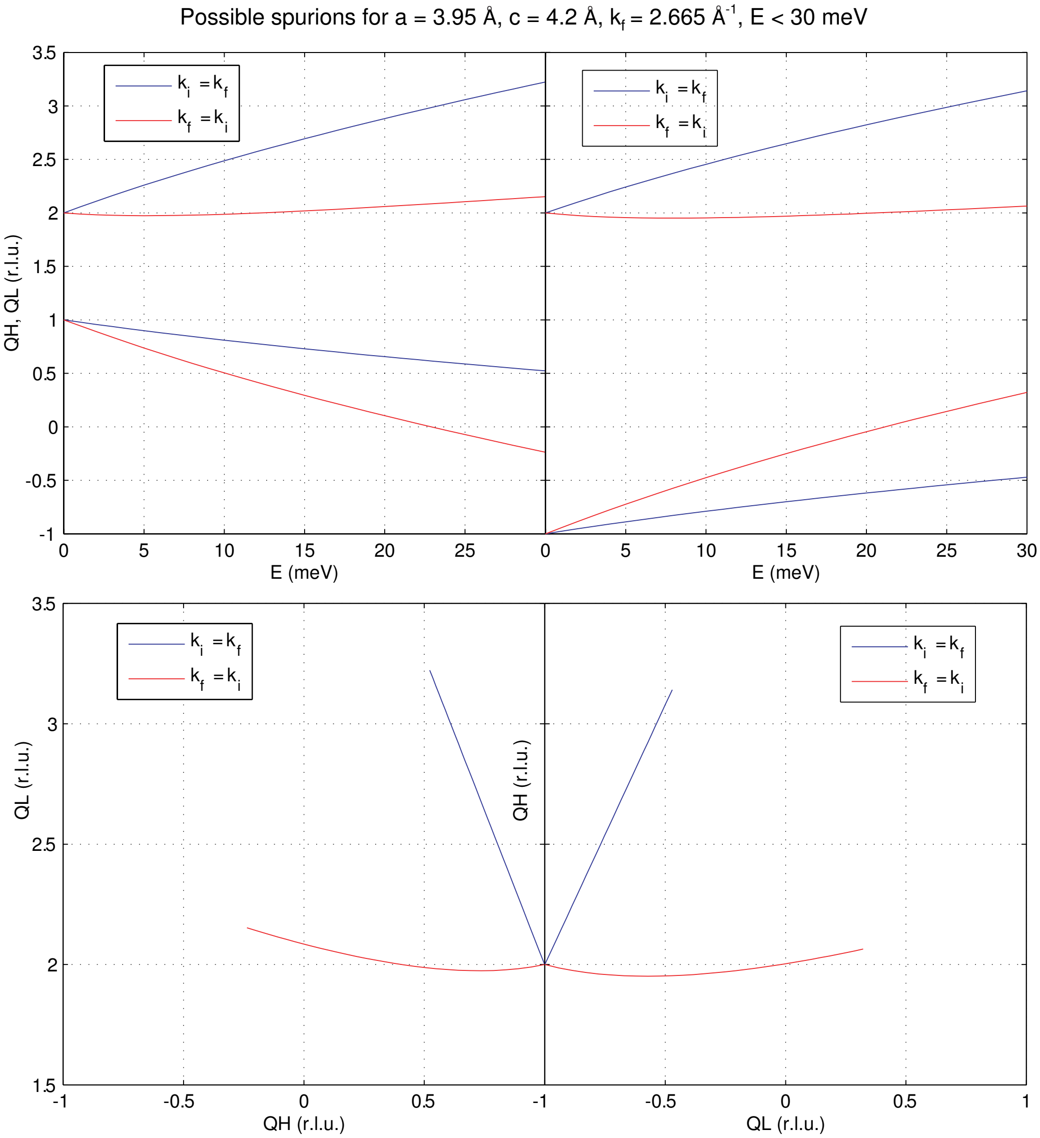

Figure 4.10: Calculation of possible paths of spurious scattering in an orthorhombic lattice (here with lattice parameters of $PbTiO_3$) arising from Bragg peaks (102) and $(20\bar{1})$. Q_X, Q_Y are in r.l.u., energy in meV. Top panel shows at which points the spurion can appear in the spectra (e.g., in the top-left panel, near $\vec{Q} = (0.5, 0, 2)$ or near $\vec{Q} = (0.8, 0, 2.5)$ at energy 10 meV). The two possibilities correspond to accidental incoherent scattering from monochromator ($k_i' = k_f$) or analyzer ($k_f' = k_i$). Bottom panel shows the path of the spurion in the scattering plane for different energy transfers, here up to 30 meV. At zero energy, of course, we get the limiting case of the Bragg scattering itself. Note the exchanged axes in the right bottom panel.

strong signal other than intended to measure (elastic scattering, diffuse scattering, strong phonons,...) – see figure 4.8a. Then another peak appears in the spectrum, with energy (or $\vec{Q}$) shifted accordingly with the size of the ellipsoid.

The spurious effects originating from accidental elastic scattering or from the capture by the tail of the resolution, are often very sharp (with respect to the resolution widths and comparing to “true” signal), strong and suspiciously “nice” (well-defined). This should be an incentive to check the origin of the signal, as described above.

Neutrons can be **double-scattered** in the sample – apart from the coherent one-phonon scattering, another Bragg scattering can take place. As a result, if the geometry of the experiment is favourable to this process, we can observe e.g. longitudinal modes in a predominantly transverse spectrum (see section 5.15). The probability of such spurion increases with the size of the sample and with its mosaic spread.

Multi-phonon scattering (equation 3.19), although coming from inelastic scattering from the sample, is mostly not useful in data analysis. Although the intensity of multiple phonon scattering is generally small, its contribution to the spectra can be considerable, especially at high energy transfers, where many combinations of lower-energy phonons are available. The resulting signal is slowly varying with energy (it may look like “very broad phonons”), but can cause problems with resolving weak or broad signal. As an example, see figure 5.22.

Parasitic scattering may occur also from **sample environment**, from other accessories present at the instrument, or from air in the vicinity of the sample (where the neutron beam is most focused). In our example (figure 4.11a), the extra signal at cca. 4 meV corresponds to scattering at some angle on the cylindric case of the furnace; then the beam is analyzed as if it was inelastically scattered on the sample, with energy loss 4 meV. Sample rotation (changing only the angle ω) did not change the measured intensity, on the other hand, after closing the slits the signal disappeared (figure 4.11c). Typically, making the beam better defined, e.g. by adjusting (more closing) the slits, helps to get rid of this problem. Another possibility is to change the geometry (angles in the scattering process), e.g. by choosing a different Brillouin zone (figure 4.11b).

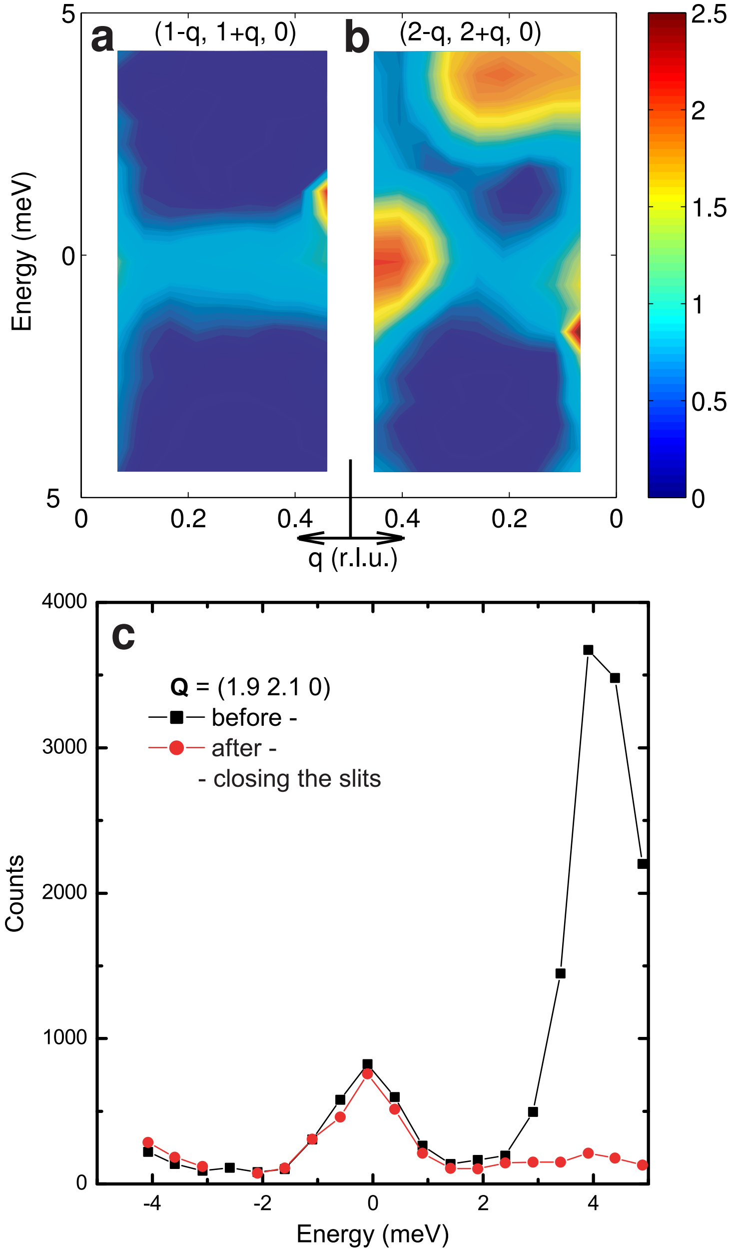

Figure 4.11: Example of accidental scattering from sample environment; $(\vec{Q}, E)$ map (a) in the (220) BZ (spurion present at 4 meV), (b) in the (110) BZ (not present). The intensity scale is logarithmic. (c): Effect of the slits closing. Measured on the IN8 instrument (ILL) at 600 K on $Na_{0.5}Bi_{0.5}TiO_3$ not presented in this thesis. Lines are guides to the eye.

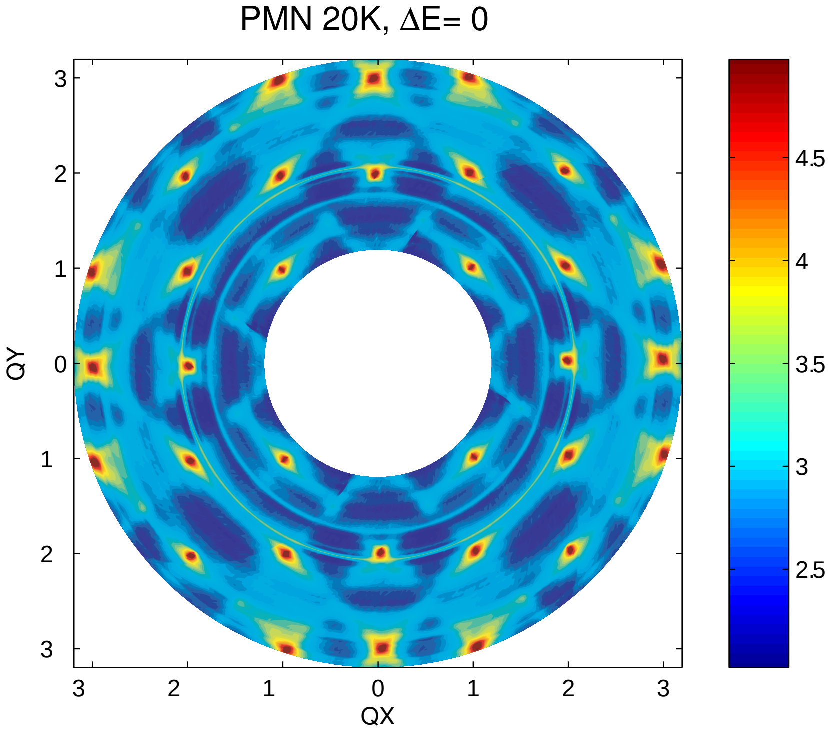

Figure 4.12: Brag scattering, diffuse scattering and powder lines in an "elastic" map (within the energy resolution) of PMN.

4.5 The *FlatCone* multianalyzer

4.5.1 Intensity maps in reciprocal space

During the analysis of the INS experiments, it showed to be useful to represent the experimental data (either measured by constant-$\vec{Q}$ or constant-E technique – see section 4.3)) as colour 2D intensity maps, whenever a more complete set of scans was available. This task can be equally applied to phonon dispersions (see e.g. figures 6.4,5.20,5.2), diffuse scattering (figure 4.12), mapping of the shape of Bragg reflections, unwanted scattering (figures 4.11,4.12,4.9) and many others, including equivalent phenomena from magnetic scattering (for illustration see spin waves in CuGeO$_3$, figure 4.13).

One of the apparent advantages of the pseudo-3D representation of the experimental data is that one gains the overview of the investigated object in a considerable part of the chosen $(\vec{Q}, E)$ subspace. In the case of phonon dispersions, one gets an idea of their whole (apparent) dispersions, instead of single peaks in single spectra.

Concerning the *FlatCone* (FC) multianalyzer and multidetector described

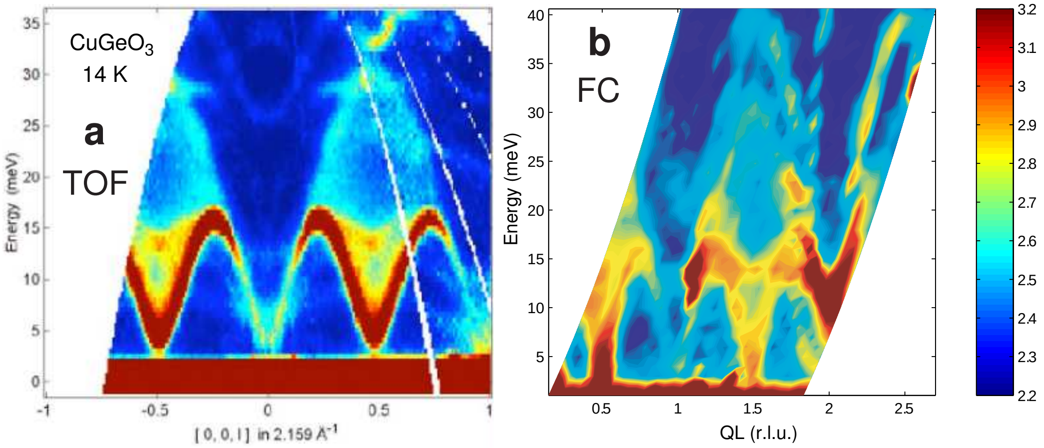

Figure 4.13: Spin waves in $CuGeO_3$ measured by (a) TOF (ISIS) [Arai 96] and (b) *FlatCone*.

hereafter, the natural outcome already is such a map, similarly as in the case of TOF (naturally of a different than rectangular shape in the (Q_x, E) or (Q_x, Q_y) coordinates; x, y mostly denote symmetry directions of the crystal).

4.5.2 *FlatCone* characteristics

The essential components of *FlatCone* are:

- two sets of 31 analyzers, adjusted to reflect neutrons with wavenumbers $k_f = 3\,\text{Å}(\approx 18\,\text{meV}$, thermal) and $k_f = 1.5\,\text{Å}(\approx 4.5\,\text{meV}$, cold). The fact that the analyzers are optimized for fixed scattered energies implies a compulsory fixed-k_f mode.
- one set of 31 ^{3}He detector tubes in horizontal position (see figure 4.14b) that serves for either of the sets of analyzers, being selected by a movable vertical partition.
- shielding – polyethylene blocks with B_4C lining, covering the whole box (figure 4.15a,b), and absorbing plates (aluminium doped with boron, figure 4.14a) which prevent crosstalks between neighbouring channels.

Each analyzer (figure 4.15c) is a cassette containing (values for thermal neutrons; those for cold neutrons are in brackets) 10 (12) blades of Si 111 crystals, 15 (20) mm wide, 200 (150) mm long, 1 (0.85) mm thick and bent to curvatures optimized for focussing at the respective energies. Si 111 analyzers, besides bending, permit to avoid filters of second-order neutrons (see

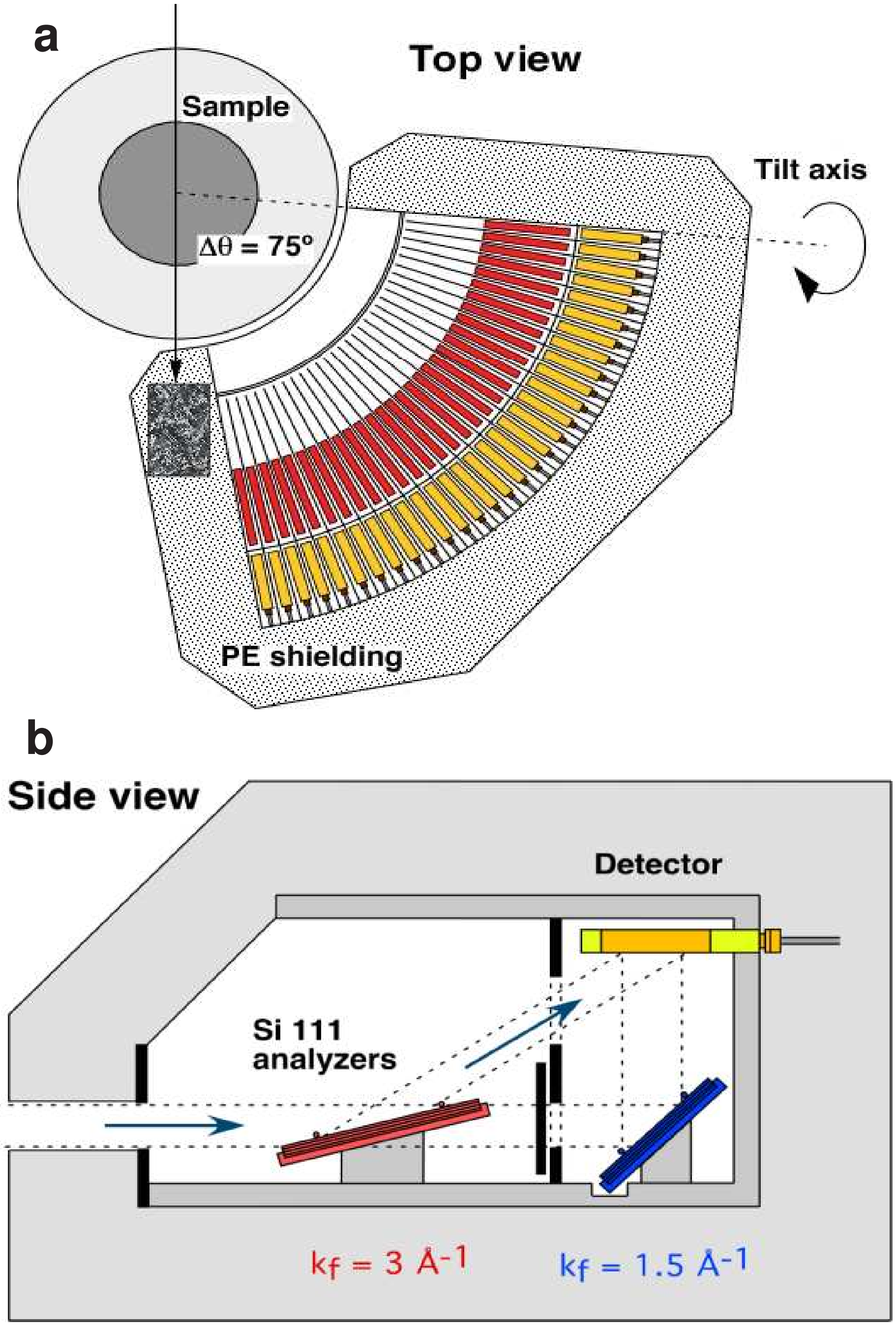

Figure 4.14: Schematic sketch of the multianalyzer layout; a: top view, b: side view.

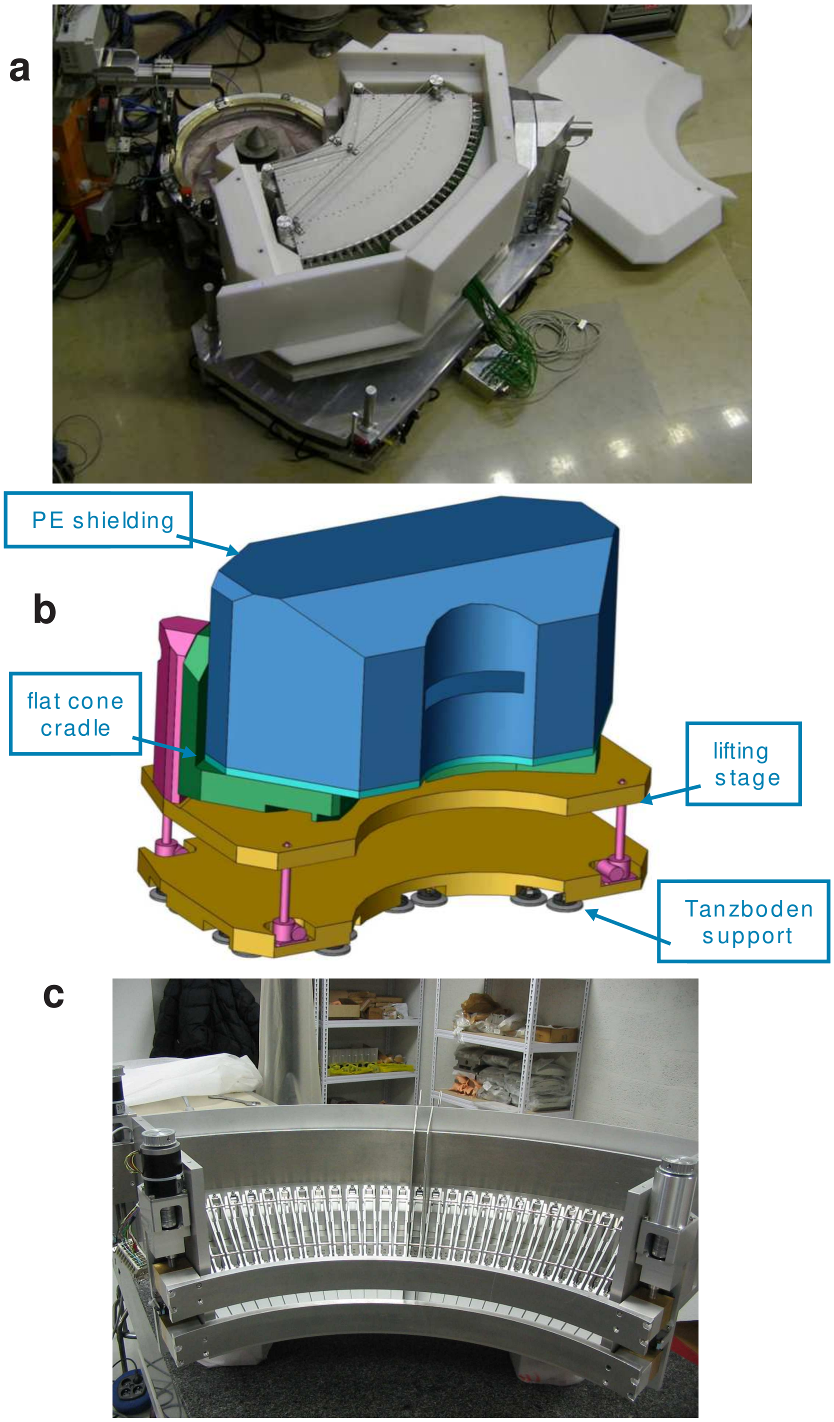

Figure 4.15: a: photo of FC during commissioning tests; b: model of the FC shielding and lifting stage; c: photo of one set of the analyzer cassettes mounted into the box.

section 4.3), which is essential in the case of *FlatCone*, as we do not deal with a single analyzer.

The 31 analyzers cover the angular range 75 degrees. Each channel thus corresponds to a different scattering angle 2θ, with the step $\Delta(2\theta) = 2.5\,\mathrm{deg}$ in between. The angular acceptance of each channel is roughly one half of those 2.5 deg belonging to the channel. It is therefore recommended to make (typically) two scans shifted by 2θ to cover the blind areas (cf. figures 4.16b,c).

The whole box is attached to the instrument similarly as the single analyzer, and lies on a lifting stage enabling to adjust the height and to tilt the whole box (to reach out of the scattering plane).

As was already mentioned (and as it follows from the construction), maps obtained with *FlatCone* are rectangular in "instrument coordinates": one of them is naturally the scattering angle 2θ, the second one is typically the sample rotation angle ω (figure 4.16a) or energy E_i of incident neutrons. From geometry, these coordinates can be recalculated to usual momentum-energy ones (figure 4.16a,b). In practice, e.g. in the case of const-E sweeps, one has to take into consideration the moving and "deforming" of the shape (figure 4.17b), depending on the energy transfer, unit cell dimensions of the sample and on the magnitude of 2θ for a reference channel.

FlatCone can be operated in several scanning modes:

- const-E mode, schematically sketched in figure 4.17c, is performed just by rotating the sample; the resulting $(2\theta, \omega)$ map is transformed into (Q_x, Q_y) coordinates (figure 4.16.
- const-$\vec{Q}$ mode, when a selected channel is set to perform a conventional const-$\vec{Q}$ scan, thus defining the paths of other channels.
- k_i-mode, a simpler variant of the const-$\vec{Q}$ mode; cf. figure 4.13. The output of the two latter modes is usually represented in (Q_x, E) coordinates (figure 4.13).

4.5.3 *FlatCone* commissioning tests

Prior to first neutron measurements, the analyzer crystals had been pre-adjusted and bent to the nominal curvature of $R = 2.3\,\mathrm{m}$, on the ILL's hard X-ray diffractometer.

The first part of the hereafter-described commissioning tests was performed on the ILL's IN3 spectrometer, and were carried out with the first set of analyzers (with $k_f = 3\text{Å}^{-1}$), using a PG (002) monochromator and a

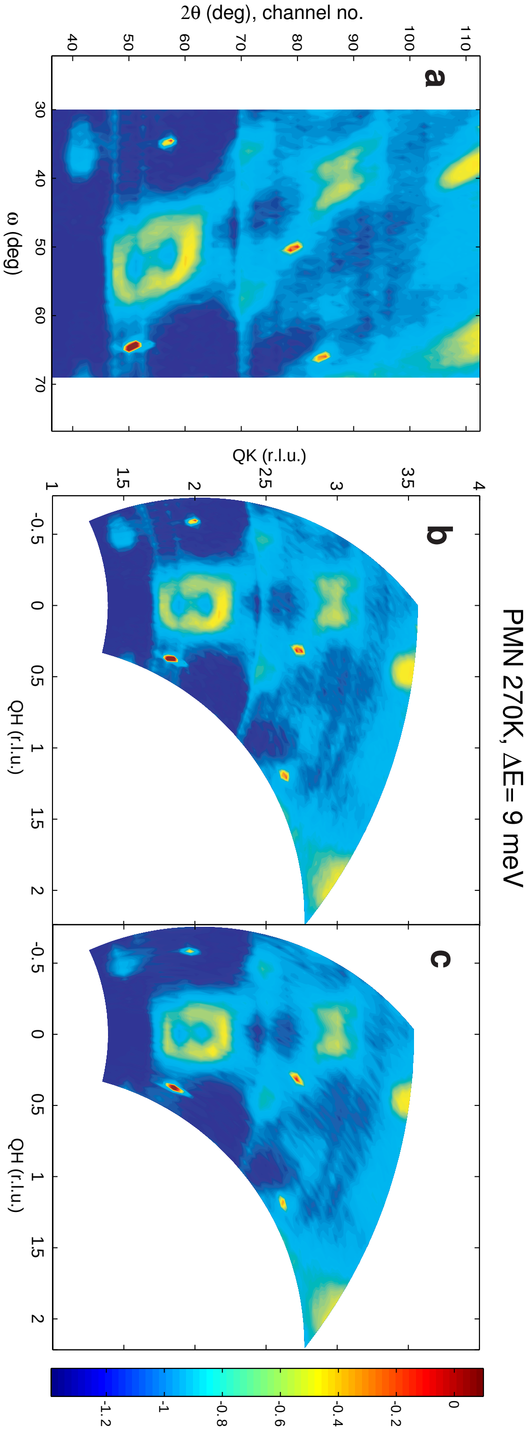

Figure 4.16: Example of representation of the FC const-E data; a: in $\omega - 2\theta$ coordinates, b: in reciprocal space. Panel b contains two overlapped scans, mutually shifted by 2θ as described in the text. For comparison, panel c consists only of one of the scans.

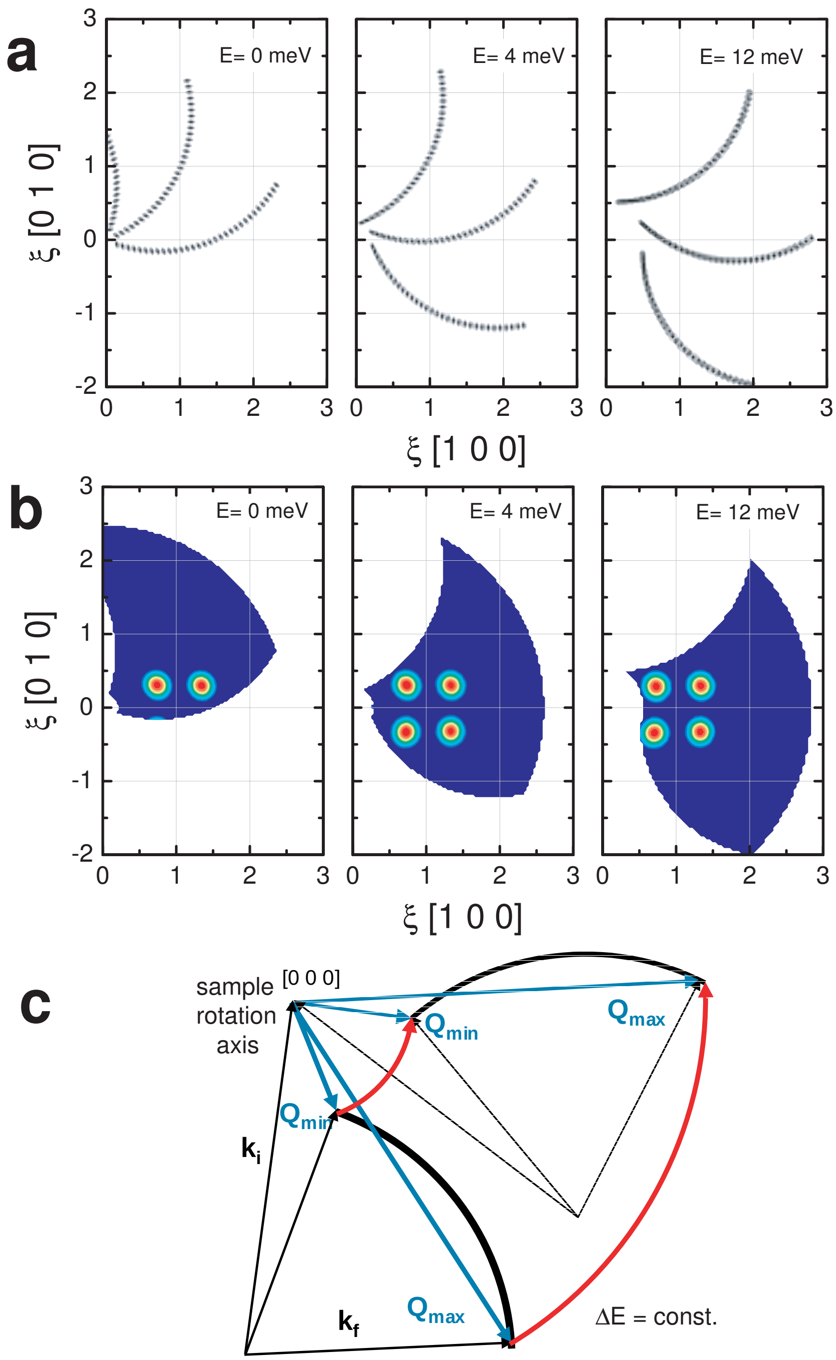

Figure 4.17: a: schematic plot of the “lines” (set of points) in the scattering plane that are measured at once, for 3 different rotations ω of the sample, and at different energy transfers (simulated by RESTRAX [Saroun 04]); b: area covered for a given range of ω is generally changing its shape with energy [Saroun 04]; c: sketch of the principle of ω- scanning.

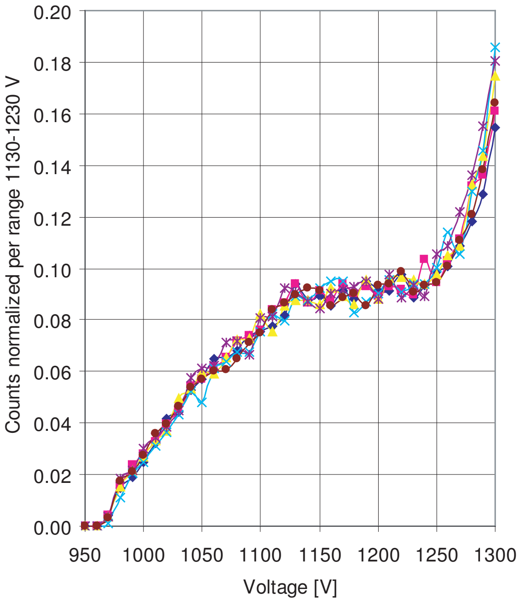

Figure 4.18: Plateau characteristics for 6 arbitrarily chosen channels, corrected for differences between analyzers.

standard IN3 vanadium sample[4]. We were able to collect signal from 6 out of the total 31 detector tubes at a time. The standard IN3 detector stayed connected and served as a reference of the background. The purpose of these tests was to check the functionality of the elements of the detection system (analyzer crystals, ^{3}He detector tubes and preamplifiers), and to adjust them in order to achieve optimum detection efficiencies throughout the channels.

The box with analyzers and detectors was aligned manually with respect to the IN3 sample table, temporarily without the possibility of changing the energy transfer. Provisional B_4C shielding significantly reduced the background, except for the first and last channels (see below).

The optimum magnitude of high voltage applied to detectors was determined from the plateau in the voltage dependence of detector efficiency (figure 4.18) and set to 1150 V.

Independently of the other effects, we checked that the preamplifiers have equal efficiencies within the statistical errors.

As the next step, we separated the possible effect of detector tubes in the same manner as for the preamps. Their detection efficiencies, specified by their manufacture, showed to stay within the interval of ±3%.

---

[4] The tests and adjustment of the second set of analyzers with $k_f = 1.5\text{Å}^{-1}$ were performed in the same way on the cold-source IN14 instrument and are not described here; moreover the author was not active in the second part.

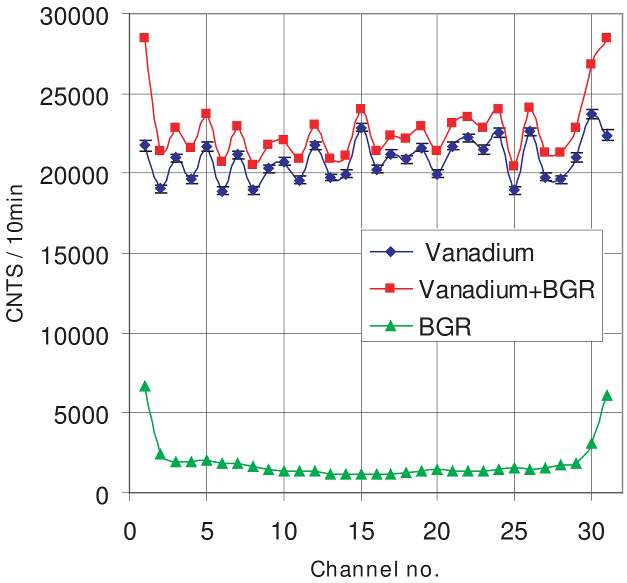

Figure 4.19: Characteristics of *Flatcone* channels: intensity from scattering on vanadium and free space (background).

Finally, we used the adjustment screws to optimize the orientation of analyzer crystals, in order to obtain maximum signal from each analyzer. After subtracting the background measured without vanadium, the resulting difference among the intensities of the analyzer-detector pairs does not exceed ±10% (figure 4.19). The exceptions were only the channels on the edge of the box, which were affected by higher background, caused by temporarily lower shielding during these tests. The variances in remaining channels are predominantly due to a spread in effective curvatures of individual analyzers.

As the next step, we tested the *FlatCone* on IN20 for real measurements, i.e. already connected to positioning motors and with full shielding. Characteristics of individual channels by scattering on vanadium are summarized in figure 4.20. The zero energy positions were ±0.25 meV, the energy resolution widths (FWHM) 1.58 ± 0.04 meV (in good agreement with the value 1.40 meV predicted by Monte Carlo ray-tracing simulations in RESTRAX), and peak intensity spread was ±8% (relative standard deviation).

Figure 4.21 compares maps assembled from conventional const-E scans, with the "one-scan" 2D *FlatCone* map. It is obvious that with less effort we get better survey of the scattering plane than with classical TAS.

It is clear at first glance, that the first scans taken with *FlatCone* were of worse quality than with TAS. During the commissioning tests, several

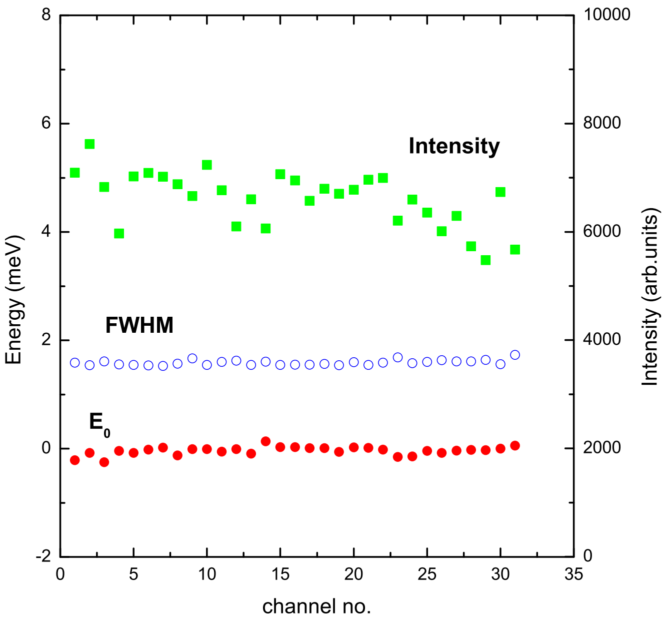

Figure 4.20: Vanadium positions (E_0), widths (FWHM) and scattering intensities (see right axis) of individual analyzer channels. The results manifested very good uniformity.

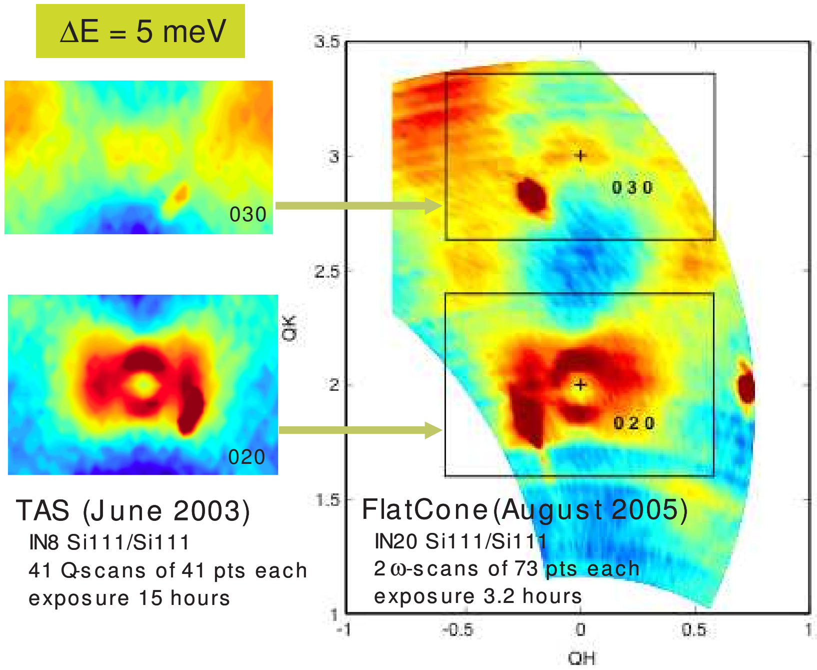

Figure 4.21: Comparison of time efficiency of conventional TAS setup and the *FlatCone* setup. For explanation of experimental artefacts see text.

technical problems occurred, which partly affected the data collected in the beginnings, but have been gradually solved – above all the "wavelets" occurring in const-E maps which have been an artefact in the detection system. Further, we managed to improve the overall quality of the signal by suppressing background, "powder" lines and spurious peaks (concerning the last item, cf. figure 5.6).

In conclusion, he main advantages of the *FlatCone* option are following:

- It is a versatile tool which facilitates the search for useful signal in a similar way as TOF.
- The data collection is by an order of magnitude faster (cf. figure 4.21) thanks to scanning the whole line at a time (figure 4.17a) instead of a single point in each step. One thus saves the valuable and costly neutron beam time. Moreover, such scanning requires much less movements of the positioning motors.
- In contrast to conventional single-detector setup, it allows to access momentum transfers in the vertical direction, i.e. out of the scattering plane, without changing the sample orientation. This is very useful especially when turning the sample would require significant time effort (e.g. when fixed in sample environment).
- The instrument resolution is generally better (even if partly at the expense of counting rate). Compared to a conventional analyzer, the FC analyzer crystals are narrower (have smaller acceptance angle) and scatter upwards (out of the horizontal plane).

Apart from the fact that such data overview is of useful informational character ("for the eye"), the data are to be subject to further systematic analysis, such as consistent fitting of the whole set of 3D data with a suitable model, which is a task for near future. As a first step, an inverse procedure has been applied for now – extracting "straight" lines (conventional scans) in the $(\vec{Q}, E)$ space from the maps.

Chapter 5

Inelastic neutron scattering studies of PZN–8%PT and PMN

In this chapter, we present our inelastic neutron scattering studies on relaxor ferroelectrics, together with detailed comparison to results from literature. The main part is devoted to the so-called waterfall effect, which is closely connected with the dynamical properties of relaxors and their temperature dependence. The nature of extra modes, also closely related to the issues of lattice dynamics and polar nanoregions, is discussed in the end.

5.1 The "waterfall effect"

In the past decade, inelastic neutron scattering (INS) studies of relaxor materials often stimulated a discussion about the nature of the behaviour of relaxors (cf. [Naberezhnov 99, Gehring 00a, Gehring 01a, La-Orauttapong 02, Wakimoto 02b, Vakhrushev 02, Hlinka 03b, Stock 05, Gvasaliya 04]). One of the most challenging observations was the apparent vertical dispersion of the soft TO branch (the so-called waterfall effect), first noticed in the crystal of PZN–8%PT [Gehring 00a], and then observed in a number of subsequent experiments on similar relaxor-like systems [Gehring 01a, La-Orauttapong 02, Wakimoto 02b, Gehring 00b, Tomeno 01, Koo 02]. The waterfall is temperature dependent, as was e.g. demonstrated by [Wakimoto 02b], figure 5.1; see also figure 5.2.

Immediately after the discovery of the waterfall effect, it was proposed that the phonon wave vector at which the waterfall phenomenon occurs, ($q_{\mathrm{wf}} \approx 0.2\,\text{Å}^{-1} \approx 0.15\,\mathrm{r.l.u.}$), reflects the correlation length of polar nanore-

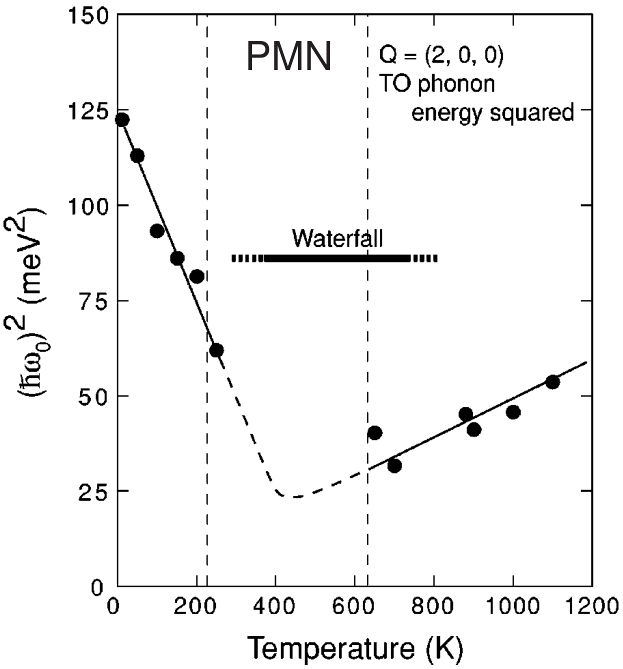

Figure 5.1: Temperature dependence of the TO soft mode frequency; copied from [Wakimoto 02b].

gions (PNRs) [Gehring 00a]. However, several facts testify against this proposition - for example, another experiment performed in PZN–8%PT has demonstrated that q_{wf} changes substantially between different Brillouin zones (see figure 5.3a) [Hlinka 03a].

As a matter of fact, a very similar feature was documented also in the soft mode data of a standard, single domain ferroelectric $BaTiO_3$ (see figure 5.3b) [Shirane 70b], which suggests that the importance of the waterfall feature is a more general issue relevant also to other materials beyond the borders of relaxor physics.

It was also proposed that the very essence of the waterfall phenomenon may consist in perturbation of the damped harmonic oscillator (DHO) response of the soft mode by its interaction with the nearby transverse acoustic (TA) mode [Hlinka 03a, Ivanov 05]. In this acoustic-optic mode interaction (AOMI) model, the value of q_{wf} is determined solely by the interplay among the shapes of phonon dispersion curves, values of damping parameters and structure factors. This implies that a similar effect and similar values of q_{wf} are to be expected in related compounds with slightly modified B-site occupancy, as it is indeed observed for example within the PMN–xPT and PZN–xPT family [Gehring 00a, Gehring 01a, La-Orauttapong 02]. Such an

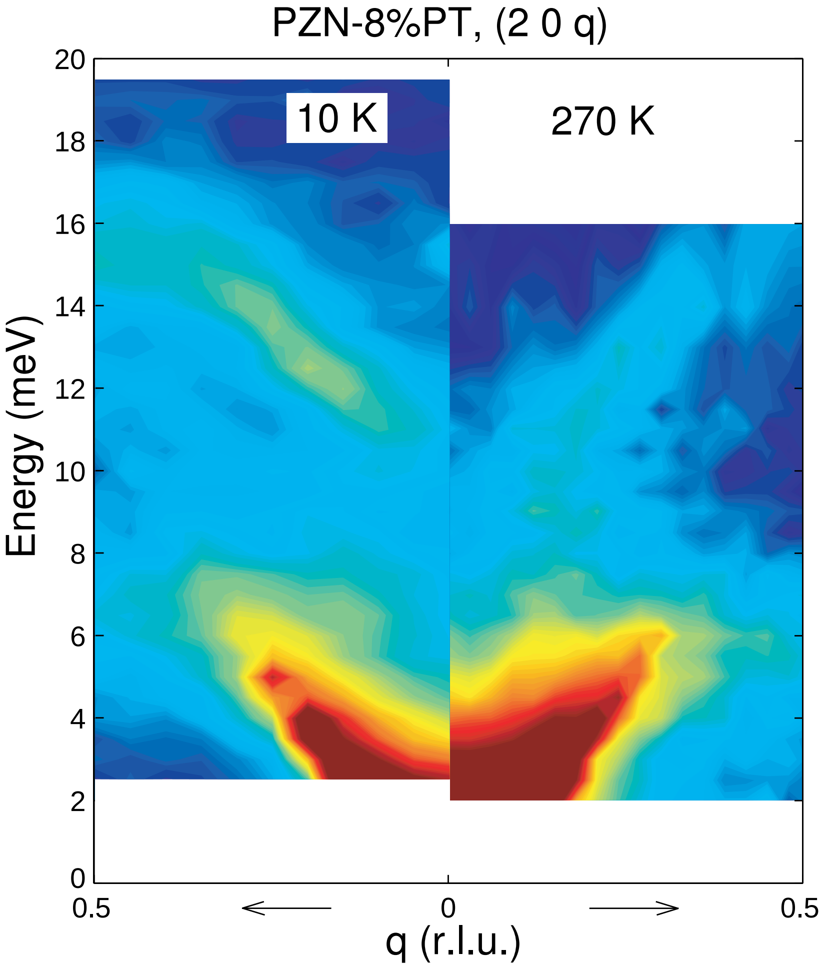

Figure 5.2: Waterfall effect in PZN–8%PT in the (2 0 0) Brillouin zone (BZ) is present at 270 K, but disappears at low temperatures (10 K). The intensity scale (not shown) is logarithmic, and arbitrary between different temperatures (taking into account the Bose factor).

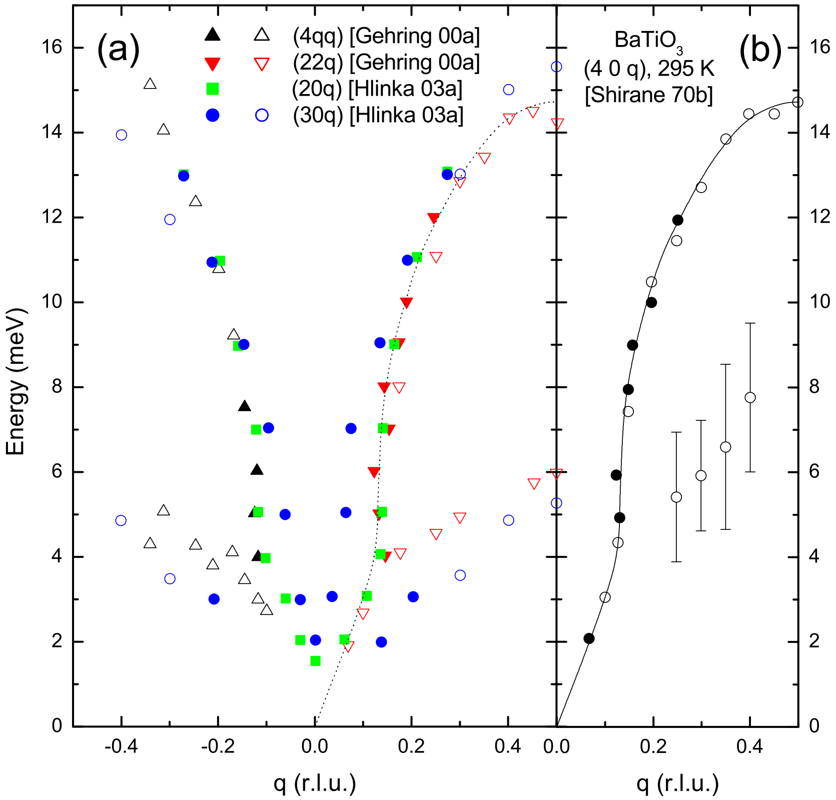

Figure 5.3: Waterfall effect in PZN–8%PT and $BaTiO_3$. Left (a): comparison of the apparent dispersion curves of lowest frequency transverse phonon branches of PZN-8%PT at 500 K, as obtained in [Gehring 00a] (triangles) and independently in [Hlinka 03a](squares, circles). The almost vertical segment of the upper phonon branch appears at the same wave vector (waterfall wave vector q_{wf}) for the measurements taken in Brillouin zones with even indexes; it has a clearly smaller value for measurements done in (030) zone (circles). Full symbols stand for peaks in constant energy scans, open symbols stand for maxima in constant-q scans. Right (b): Similar plot of apparent dispersion curves for a single domain tetragonal ferroelectric $BaTiO_3$ from [Shirane 70b]. The continuous lines serving as a guide to the eye in (a) and (b) are identical.

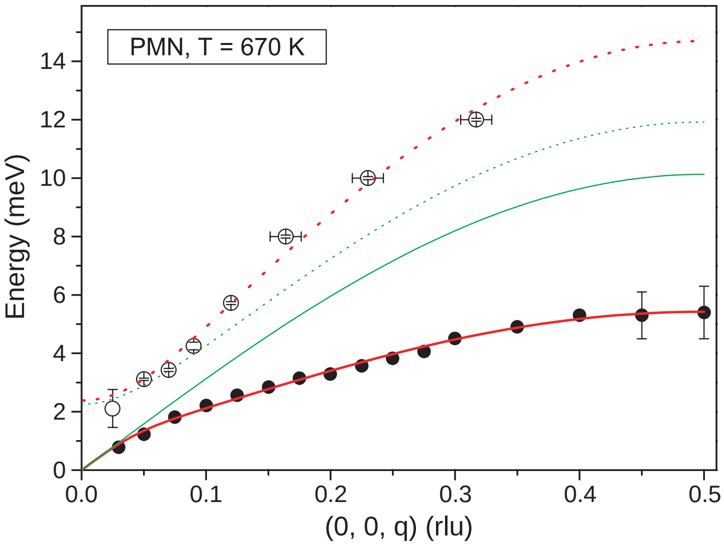

Figure 5.4: Dispersions of the TA (solid circles) and the lowest TO (open circles) branches in PMN at T = 670 K, copied from [Gvasaliya 05]. The solid and dotted green lines correspond to the calculated dispersion of the TA and TO phonons with the coupling set to zero.

interpretation, however, seems to be in contradiction with the more recent experiment [Gvasaliya 05] with the prototypic relaxor system PMN, disclosing a well underdamped and largely temperature independent soft optic branch with no sign of a waterfall-type phenomenon (see figure 5.4).

In such a situation, it is desirable to reconcile the recent "no-waterfall" results in PMN [Gvasaliya 05], partly reproduced also in the similar system PMN-30%PT [Gvasaliya 07], with those of previous work on PZN-8%PT [Gehring 00a, Hlinka 03a] and on PMN [Gehring 00b], all of which have produced an evidence for the "waterfall" phenomenon. For this purpose, we have initially formulated the following rather simple hypotheses as possible explanations:

1. The large soft mode damping and the anomalous q-dependence of the spectral lineshape observed in earlier experiments is just an apparent effect that was in [Gvasaliya 05] avoided by using more appropriate experimental conditions[1].

2. The waterfall effect does not appear in the experiments of [Gvasaliya 05] just because of different phonon structure factors (in the spirit of the model of [Hlinka 03a]), associated with a different BZ choice.

---

[1] First two hypotheses are close to those invoked in [Gvasaliya 05].

3. The absence of the waterfall effect in experiments of [Gvasaliya 05] is merely a matter of different data treatment and interpretation.

4. Different TO soft phonon mode properties merely reflect the differences in growing methods or in thermal history of the investigated samples.

5.2 Experimental confirmation of the waterfall effect under improved resolution conditions

The magnitude of the TO mode damping plays an important role in all theories, trying to explain the waterfall phenomenon [Gehring 00a, Wakimoto 02b, Stock 05, Hlinka 03a, Ivanov 05, Gvasaliya 05, Glinchuk 02]. Thus, the observation of a visibly underdamped TO soft mode might be ultimately related to the absence of the waterfall, and the theoretical possibility that the soft mode damping was strongly overestimated due to the resolution effects should be clarified. Indeed, frequency shifts and line broadening due to steep slopes of phonon dispersion surfaces in conjunction with the relaxed resolution profile in certain directions of the 4-dimensional ($\vec{Q}-E$) space in typical experimental conditions of thermal three-axis spectrometers were previously spotted. As a rule, their a-posteriori analysis is rather difficult in the absence of a reliable 3D lattice-dynamical model [Shirane 02]. Therefore, we decided to repeat several scans with exactly the same PZN–8%PT sample, at the same temperature and the same Brillouin zone as in our previous experiment held in the Institut Laue-Langevin (ILL, Grenoble) [Hlinka 03a], but having the instrumental arrangement of the “no-waterfall” experiment [Gvasaliya 05] held previously in the Paul Scherrer Institute (PSI, Villigen).

This verification experiment was carried out on the TASP cold neutron three-axis spectrometer at the SINQ spallation source of the PSI. The instrument was operated under similar conditions as described in [Gvasaliya 05], except for a much smaller sample. Both the monochromator and analyzer were pyrolytic graphite (PG) crystals, using the (002) reflection. The data were collected at fixed momentum of scattered neutrons k_f=1.97 Å^{-1}. The collimation before and after the sample was set to 80’–S–80’ or 40’–S–40’, S standing for the sample. The measurement was performed at 500 K, on a single crystal of PZN–8%PT, already used in previous studies [Hlinka 03b, Hlinka 03a]. The sample was mounted using a niobium holder inside a furnace, with the cubic (001) axis vertical.

Representative constant-energy scans obtained in this experiment are

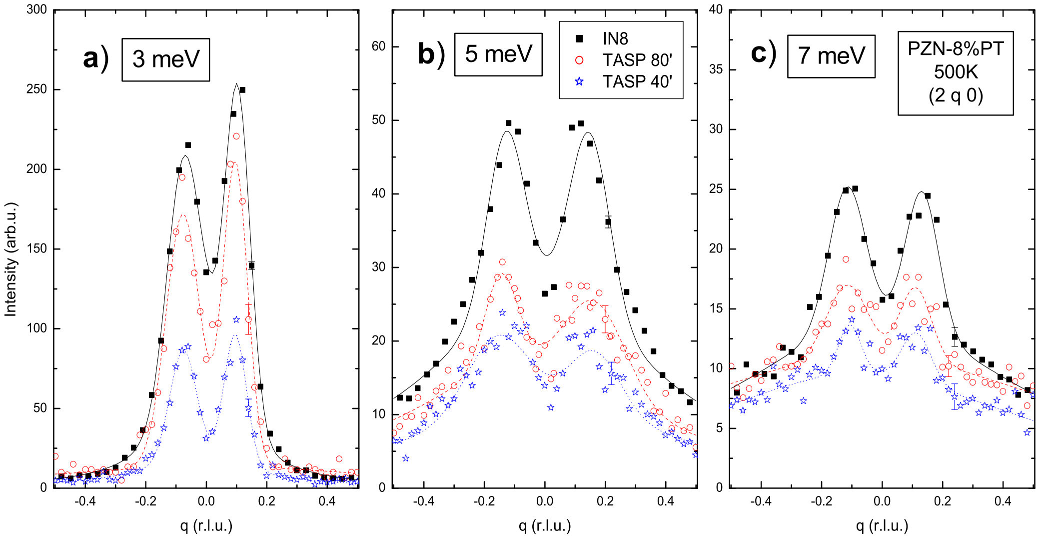

Figure 5.5: Constant-E scans (a: 3 meV, b: 5 meV, c: 7 meV) taken under different experimental conditions (from top to bottom: measured on the IN8 instrument at the ILL with Si monochromators; measured on the TASP instrument at PSI with PG monochromators and 80' collimation; measured on the same instrument with 40' collimation). Lines are guides to the eye.

shown in figure 5.5, in comparison with the data taken earlier at the ILL. The peak positions in scans taken at TASP with 80'–S–80' and 40'–S–40' collimation (FWHM energy resolution about 0.37 meV and 0.3 meV, respectively) are the same as the positions observed in a former ILL experiment (energy resolution about 1.3 meV). Clearly, the data of figure 5.5 show that the waterfall phenomenon in PZN–8%PT is robust with respect to different resolution conditions. Thus, the waterfall effect is not an experimental artefact and the first hypothesis given above is not likely to explain the absence of the waterfall in PMN.

We also managed to collect systematic constant-E maps of PMN with *FlatCone* (see chapter 4.5), which can achieve better resolution than conventional ILL's three-axis configuration. From figure 5.6 and figure 5.7 (extracted (q, E) dispersion from maps in figure 5.6), we again clearly observe the waterfall in the (2 0 0) BZ.

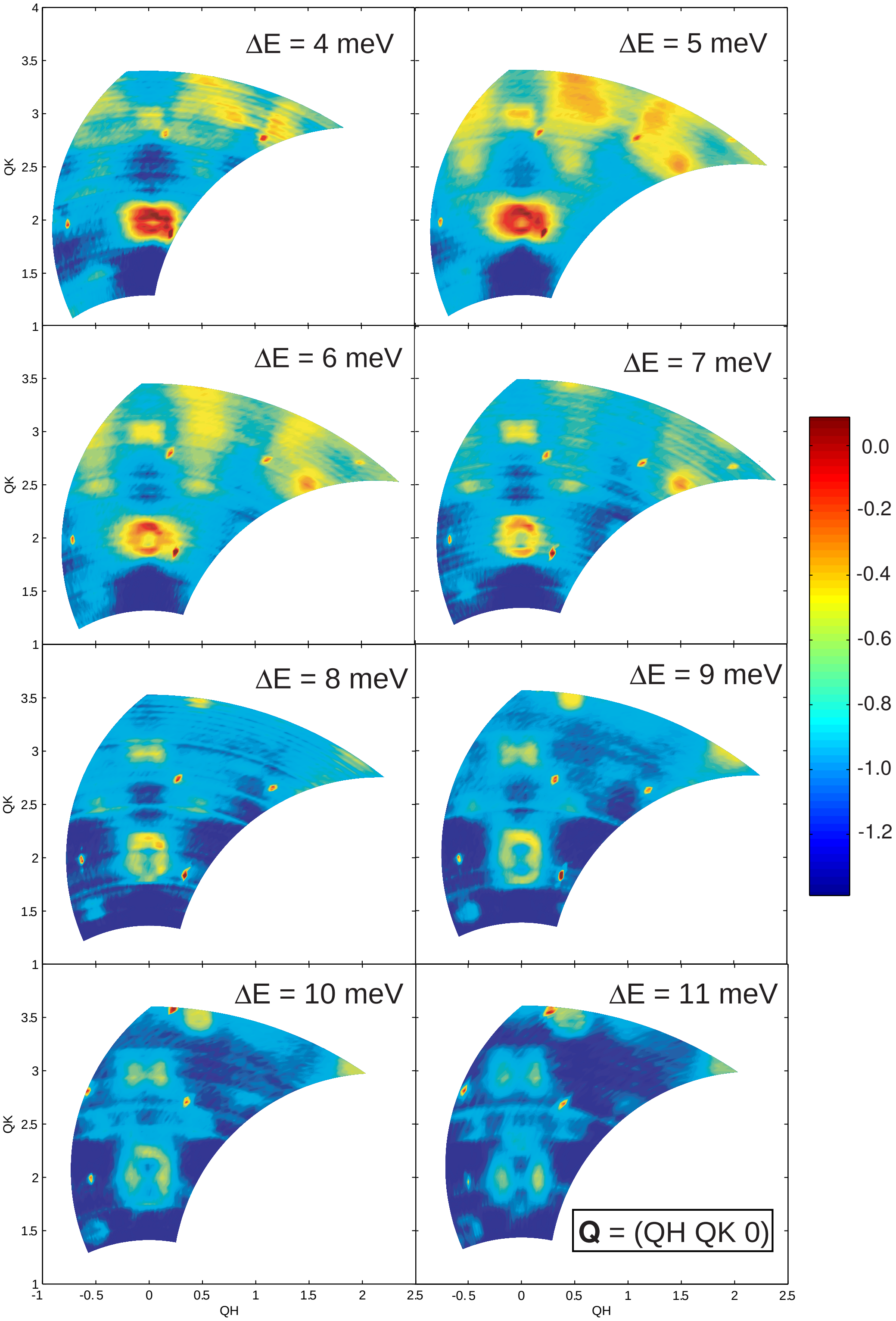

Figure 5.6: Constant-E maps of PMN made with FlatCone at 270 K.

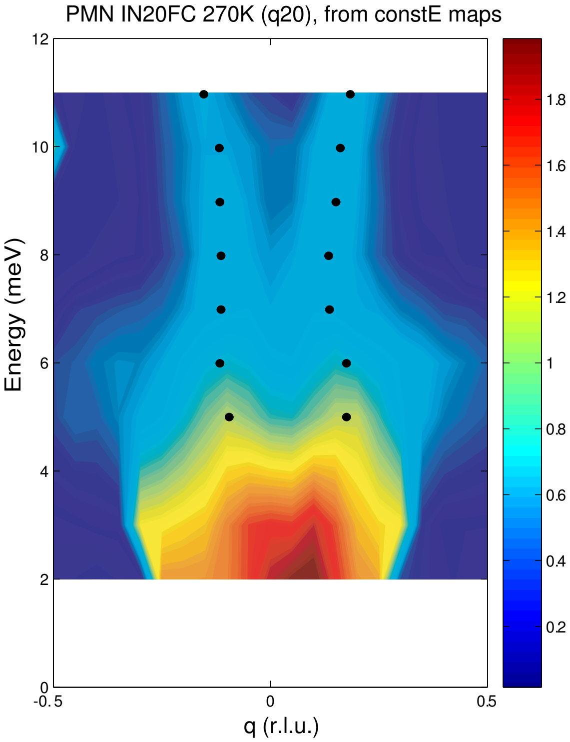

Figure 5.7: The "waterfall" dispersion in PMN at 270 K as extracted from const-E *FlatCone* maps (figure 5.6). The dots are peak positions from const-E scans.

5.3 The AOMI model and the influence of structure factors on the waterfall effect

The second hypothesis actually requires to recall results of the AOMI model of [Hlinka 03a]. It is based on the fact, that spectral maxima of the coupled DHO response under certain conditions (which are essentially those of Breit-Wigner-Fano resonance [Scott 74, Eklund 77]) may strongly depend on the relative mode strengths, here given by dynamical structure factors for inelastic neutron scattering by phonons. It was shown previously [Hlinka 03a] that even a very usual wave vector dependence of the oscillator parameters can lead to the waterfall-like intensity distribution in $q - E$ plots, and that the position of such waterfall wave vector depends on the values of INS structure factors. Therefore, one might expect that q_{wf} collapses to zero in the $(22q)$ scattering geometry adopted in [Gvasaliya 05].

An example of such a "waterfall" effect is given in figures 5.8a,b, which displays inelastic neutron scattering (INS) response function $S(q, \omega)$ of coupled TA and TO phonon branches as a function of energy transfer E and wave vector $\mathbf{q} = q\,\mathbf{c}^* \parallel (001)$, calculated from the model of [Hlinka 03a]:

$$S(q, \omega) = f_{\mathrm{BE}}(\omega, T)\mathbf{f}_q^* \mathrm{Im}\left[\mathbf{G}(\omega, q)\right]\mathbf{f}_q \tag{5.1}$$

where

$$f_{\mathrm{BE}}(\omega, T) = \left(1 - \exp\left(-\omega/kT\right)\right)^{-1} \tag{5.2}$$

is the Bose-Einstein occupation factor, $\mathbf{f}_q = (f_{\mathrm{TA}}(q), f_{\mathrm{TO}}(q))$ is a pair of bare INS structure factors of TA and TO branches corresponding to the measurement at a given temperature T and at total momentum transfer $\mathbf{Q} = H\mathbf{a}^* + K\mathbf{b}^* + L\mathbf{c}^* + \mathbf{q}$. The 2×2 Green's function of coupled DHO modes

$$\mathbf{G}(\omega, q) = (\mathbf{D}_q - i\omega\mathbf{\Gamma}_q - \omega^2\mathbf{E})^{-1} \tag{5.3}$$

is defined with the help of the dynamical and damping matrices

$$\mathbf{D}_q = \begin{pmatrix} \omega_{\mathrm{TA}}^2(q) & \Delta(q) \\ \Delta(q)^* & \omega_{\mathrm{TO}}^2(q) \end{pmatrix} \tag{5.4}$$

$$\mathbf{\Gamma}_q = \begin{pmatrix} \Gamma_{\mathrm{TA}}(q) & \Gamma_{\mathrm{AO}}(q) \\ \Gamma_{\mathrm{AO}}(q) & \Gamma_{\mathrm{TO}}(q) \end{pmatrix} \tag{5.5}$$

and of a 2×2 unit matrix $\mathbf{E}$. The diagonal elements of these matrices have the meaning of frequencies $\omega_{\mathrm{TA}}^2(q)$ and $\omega_{\mathrm{TO}}^2(q)$, and damping constants $\Gamma_{\mathrm{TA}}(q)$ and $\Gamma_{\mathrm{TO}}(q)$ of bare acoustic and optic branches, respectively. The off-diagonal terms $\Delta(q)$ and $\Gamma_{\mathrm{AO}}(q)$ describe corresponding bilinear coupling terms. In this particular model [Hlinka 03a], the above-described elements were chosen to have the q-dependence in the form as simple as possible

$$\begin{aligned}
\omega^2_{TA}(q) &= A\sin^2(\pi q) && (5.6)\\
\omega^2_{TO}(q) &= c + B\sin^2(\pi q) && (5.7)\\
\Gamma_{\mathrm{TA}}(q) &= g\sin^2(\pi q) && (5.8)\\
\Gamma_{\mathrm{TO}}(q) &= h + k\sin^2(\pi q) && (5.9)\\
\Delta(q) &= d\sin^2(\pi q) && (5.10)\\
\Gamma_{\mathrm{AO}}(q) &= 0 && (5.11)
\end{aligned}$$

which naturally reflects the symmetry and periodicity of the dispersion along the (100) direction. The explicit parametrization of the q-dependence of the model matrices is taken as in [Hlinka 03a], and is listed in column A of table 5.1. The resulting intensity map calculated with these values is depicted in figure 5.8. The two panels differ only in structure factors, simulating different BZs with (a) and without (b) the waterfall.

Despite the model simplicity, the resulting intensity map (figure 5.8) is quite similar to the experimental intensity map found for PZN [Gehring 01a]. Following closely the constant-energy scan technique [Gehring 00a] often applied in experiments, we have traced q-positions of the maxima of $S(q,\omega)$ in figures 5.8c,d. In the case of well-defined excitations (low damping of oscillators with non-zero dispersion), the resulting lines should correspond directly to the "proper" phonon frequency dispersion curves $\omega_-(q)$, $\omega_+(q)$, given by square roots of the eigenvalues of the dynamical matrix $\mathbf{D}_q$. In the present case, the resulting curve (full lines in figures 5.8c,d) actually mostly follows such proper dispersion curves (dashed lines in figures 5.8c,d), except for the very steep part in the narrow region around $q \approx \pm 0.1$. Similar counterintuitive vertical drop of the apparent dispersion curve of the soft optic branch towards the acoustic branch at a finite wave vector was observed in PZN–8%PT. It is precisely this kind of vertical intensity ridge for which the well suited term "waterfall" was coined.

The occurrence of the waterfall strongly depends, besides the structure factors, also on the TO mode damping Γ_{TO}. Keeping the values of table 5.1 and changing only Γ_{TO}, we can follow the course of the apparent dispersion (the true dispersion is of course unchanged, as it does not depend on the mode dampings), see figure 5.9.

By selecting different total momentum transfers $\mathbf{Q} = H\mathbf{a}^*+K\mathbf{b}^*+L\mathbf{c}^*+\mathbf{q}$, the INS experiment allows to probe the same phonon branches in Brillouin zones with different indexes HKL. While the Green's function describing the phonon dynamics is obviously independent of the HKL indexes selected in the

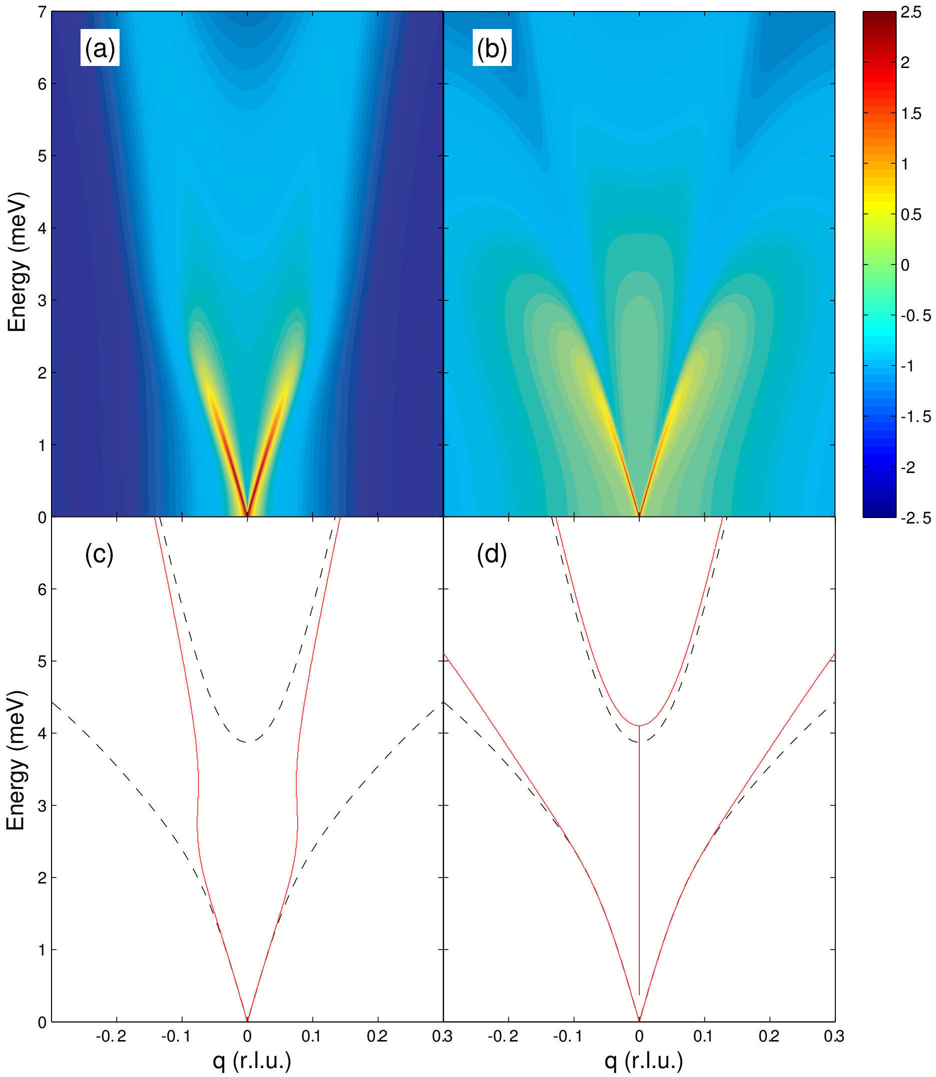

Figure 5.8: AOMI model for the waterfall effect according to [Hlinka 03a]. Top panels (a) and (b) show INS response function $S(q, \omega)$ for coupled TA+TO branches with the model parameters resumed in column A of table 5.1. Left and right panels differ only in structure factors, taken as (a) $f = (0.4, 0.6)$ (waterfall present), and (b) $f = (0.1, -0.9)$ (waterfall absent). The intensity scale is logarithmic. Bottom panels show the corresponding apparent dispersion curves (full lines) obtained by tracing the maxima positions in constant-E "scans", and dashed lines show true dispersion curves corresponding to the same dynamical system in the absence of damping. The calculation does not take into consideration resolution effects or any other contributions to scattering cross section.

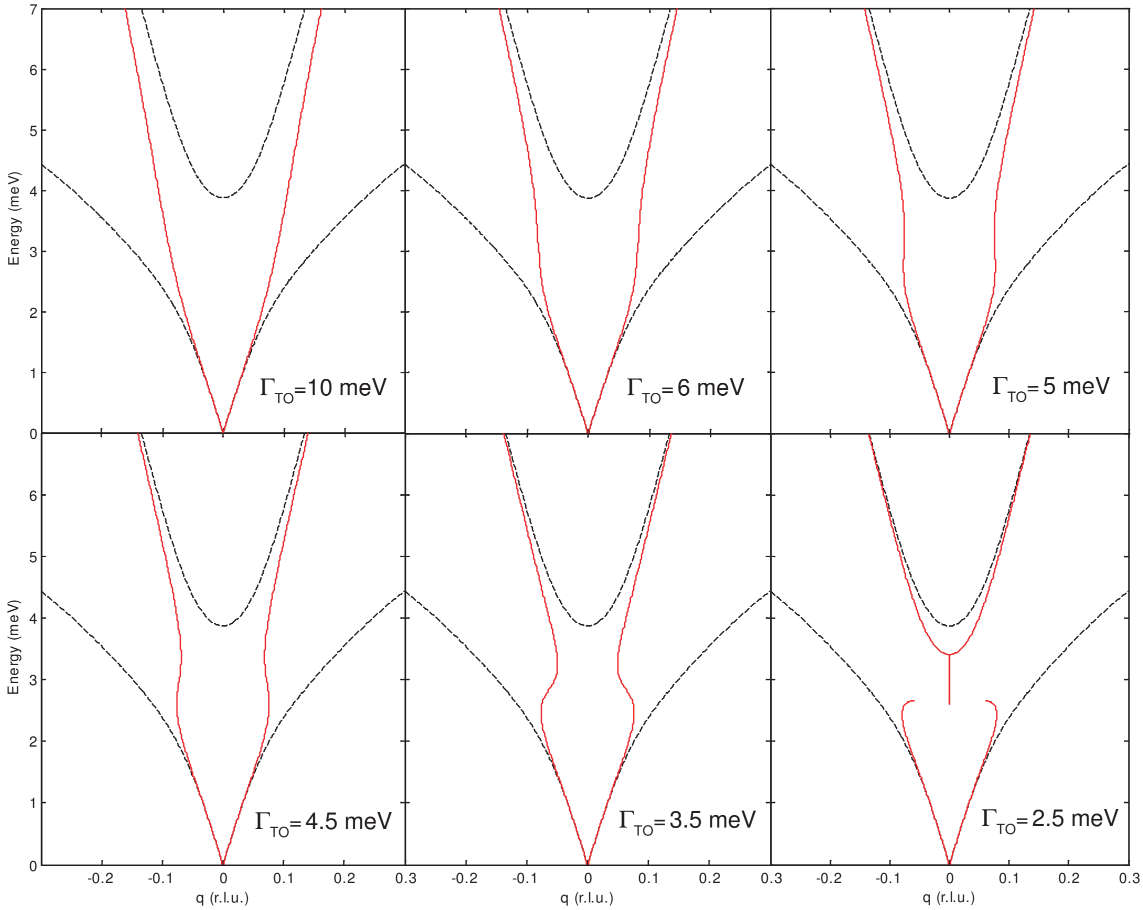

Figure 5.9: The change of the "waterfall" dispersion with the TO mode damping. Calculated for the AOMI model with the values from column A of table 5.1. Full and dashed lines have the same meanings as in figure 5.8.

	–	PMN 670 K	PMN 670 K	PMN 690 K
	A	B	C	D
ω^2_{TA} [meV^2]	$100\ t$	$101t$	$87t$	$52.4t$
ω^2_{TO} [meV^2]	$15 + 150t$	$4.4 + 137t$	$4.0 + 156t$	$25 + 150t$
Δ [meV^2]	100	85	76	50.2
Γ_{TA} [meV]	$6t$	$4.1t$	$3.9t$	$5.4t$
Γ_{TO} [meV]	5	$0.95 + 10.8t$	$0.95 + 11.0t$	eq. (5.15)
Γ_{AO} [meV]	0	$1.5t$	0	0
f_{TA}	0.4	$0.25 + 0.38t$	$0.26 + 0.50t$	13
f_{TO}	0.6	0.2	$0.20 - 0.22t$	27

Table 5.1: Parametrization of the wave-vector dependence of the $\mathbf{D}_q$ and $\mathbf{\Gamma}_q$ matrix elements introduced in equations 5.4 and 5.5, as used for calculation of $S(q,\omega)$ maps shown in figures 5.8 and 5.12. A: AOMI-model [Hlinka 03a]; B: no-waterfall model [Gvasaliya 05]; C: obtained from column B by numerical similarity transformation to the basis in which the matrix $\mathbf{\Gamma}_q$ is diagonal; D: DO-type model fitted to data of [Wakimoto 02b]. Expressions are either taken directly from the indicated references, or fitted to the available data at discrete q-points, as explained in the text. The wave vector dependence is expressed through $t = \sin^2(\pi q)$.

experiment, the scattering function $S(q,\omega)$ greatly varies with variation of the structure factors $\mathbf{f}_q$. In lead-based perovskite relaxors like PZN–8%PT, the INS structure factor of the acoustic mode is known to be much smaller than that of the soft optic mode in the 030 zone while both modes have comparable INS structure factors in zones with even indexes only. The variation of the waterfall wave vector observed in PZN–8%PT happens to exhibit the same tendency as in the outlined model [Hlinka 03a]. As a matter of fact, a mere change of structure factors is sufficient also for a complete suppression of the waterfall effect, as shown in figures 5.8b,d.

However, this mechanism of bypassing the waterfall requires relatively large change in the structure factor ratio, and thus it can hardly explain the difference between observations of [Gvasaliya 05] and [Gehring 00b]: both measurements were done around the same BZ centre (220). Moreover, measurements in PZN–8%PT show that the waterfall appears at almost the same wave vectors in both (200) and (220) BZs, which strongly supports that the structure factor ratio in these zones is quite similar. Therefore, although the above model [Hlinka 03a] can qualitatively explain the smaller value of the waterfall wave vector observed in the (300) BZ, it does not explain the result of the recent no-waterfall experiment in PMN [Gvasaliya 05].

5.4 Alternative models for the TO mode dynamics

According to the convention introduced by [Gehring 00a] and followed by others [Wakimoto 02b, Hlinka 03a], the data depicted in figure 5.3 show only *apparent* phonon dispersion curves (cf. figure 5.8), corresponding to the scattering intensity ridges in const-E scans. More fundamental dispersion curves, as given for example by the quasi-harmonic frequencies in the DHO approximation to their spectral response, are generally believed to have quite usual wave vector dependence, *without* any anomalous waterfall-like segments [Gehring 00a, Hlinka 03a, Gvasaliya 05]. Taking this into account, the wave vector dependence of the dynamical matrix elements in the no-waterfall paper [Gvasaliya 05] is exactly[2] the same as those in the waterfall theory of [Hlinka 03a], see table 5.1. Therefore, the fact that figure 3 of the no-waterfall PMN paper [Gvasaliya 05] (see figure 5.4) does not show any waterfall-like anomaly actually does not itself contradict the presence of the waterfall effect at all.

In addition, it is known that in the case of coupled DHOs, the spectral function at a given q is invariant with respect to the simultaneous unitary transformations of all $\mathbf{D}_q, \mathbf{\Gamma}_q$ and $\mathbf{f}_q$ matrices. Therefore, for a meaningful comparison of the DHO parameters of the TO mode from different coupled DHO fits, one has to take into account this additional degree of freedom. In this sense, one might suspect that the principal difference between conclusions of the no-waterfall PMN experiment [Gvasaliya 05] and the previous studies is primarily due to the different fitting strategies or due to differences in the anticipated theoretical models.

We can classify the various alternative models proposed so far under one of the following three scenarios:

- *Damping-Onset (DO) scenario.* The original idea of [Gehring 00a] assumes that the TO mode dispersion is rather usual, but that the TO damping sharply grows for wave vectors below the "waterfall" threshold q_{wf} (figure 5.10), so that the soft mode becomes suddenly strongly overdamped. The model can be extended by including the TA-TO coupling as described by the equations 5.1–5.5, as e.g. in [Wakimoto 02b]; the essential effect is nevertheless assumed to be the onset of damping of the bare TO branch below q_{wf}. This onset is postulated rather than explained by the model, but it is believed that the interaction of

---

[2] Apart from the obvious misprint - extra factor of 2 in arguments of all trigonometric functions introduced in [Hlinka 03a].

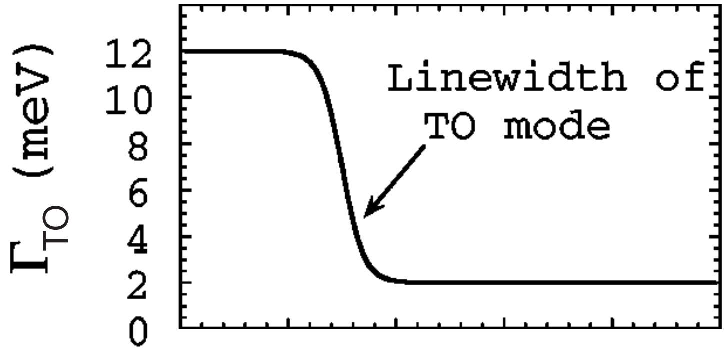

Figure 5.10: A model q-dependence of the TO mode damping Γ_{TO} in the DO scenario. Copied from [Gehring 01a].

the TO mode with the polar nano-regions (PNRs) can produce such a strongly q-dependent damping term.

- *Acoustic-Optic Mode Interference (AOMI) scenario.* The pure TA-TO mode-coupling interference scenario proposed in [Hlinka 03a] assumes that both the soft mode frequency and damping show usual wave vector dependence (without any drastic step in the damping dispersion), and that all the waterfall behaviour appears solely due to the coupling between the TA and TO modes, as described in section 5.3.

- *Extra-Mode (EM) scenario.* Several authors have proposed that an additional transverse excitation of relaxational or vibrational type overlaps or interacts with the proper soft mode spectrum. For example, [Naberezhnov 99] develops the concept of an additional vibrational mode, so-called “quasioptic mode” which is assumed to play a fundamental role of the soft mode instead of the TO1 mode. [Stock 05] put forward the idea of an independent mode of the relaxational type[3] that coexists with the TO1 mode. These additional excitations sometimes appear to be coupled to either TA or TO modes but their origin or their role in the waterfall effect were usually not specified.

The DO and AOMI scenarios differ also by the way in which they can accommodate the fact that the waterfall effect is observed only in a limited temperature window (about 250–700 K for PMN). In the DO model, it can be explained by a strongly temperature dependent density and size of PNRs; in the AOMI model, it is the TO mode temperature dependence that is

---

[3] This additional mode should not be confused with additional dielectric relaxation in the GHz region, often called (narrow) central peak.

responsible for approaching of the coupled TA and TO modes in a limited temperature region. The EM approaches were not proposed to explain the waterfall effect, so that there is no straightforward implication to the problem of the temperature window.

Nevertheless, it is worth mentioning that there was some discussion in literature about what is the true soft mode in PMN. Here we have in mind the Last-type polar mode (TO1) which is known to be of lowest frequency in lead-based relaxors. The analysis of infrared reflectivity spectra confirms that the mode seen by INS in the (200) BZ is indeed originating from the TO1 mode although some part of its spectral weight is most likely transferred to a lower frequency mode of a relaxational character [Kamba 05a, Hlinka 06b].

Unfortunately, so far available INS data taken around q_{wf} do not show very clear evidence in favour of one of these models. For example, a fit to data of [Wakimoto 02b] proposes a large damping of about 13 meV for the TO mode (making it overdamped, and thus seemingly proving the DO hypothesis). On the same data we were able to accomplish a simple fit with much more modest damping of about 8 meV (see figure 5.11), which also follows the data satisfactorily, having the TO mode underdamped ($\Gamma_{\mathrm{TO}} \approx \omega_{\mathrm{TO}}$ in this case). Similarly, the data of [Vakhrushev 02] (fitted with an extra quasioptic mode, thus supporting the EM model) are quite similar to the equivalent data of [Wakimoto 02b], fitted without the extra mode there (see figure 5.11). Of course, such extra modes can arise quite naturally, e.g. from removal of the triple degeneracy of the soft mode, from short-range-order-induced two-mode behaviour or from zone-folding effects. The need for a more complex model is obvious also from Raman [Lushnikov 99], hyper-Raman [Hellwig 06, Hehlen 07] and IR [Hlinka 06c, Kamba 03, Kamba 05a] spectra. However, it seems that the distinction of such additional features can be disregarded as a second-order effect that is not essential in the discussion of the waterfall effect itself, and in any case, no explicit model capable to explain the waterfall phenomenon with the presence of such extra modes was formulated so far.

Let us discuss in more detail the acoustic-optic coupling in PMN as revealed by the two previous reference experiments, one showing [Wakimoto 02b] and one not showing [Gvasaliya 05] the waterfall effect. The general acoustic-optic coupling scheme of equations 5.1–(5.5) remains an appropriate tool for the soft mode response description in all listed scenarios, and the simple wave-vector dependence of the $\mathbf{D}_q$ elements as assumed in [Hlinka 03a] is also commonly accepted [Gvasaliya 05]. For example, the model parameters defining $\mathbf{D}_q$ of PMN at 670 K as obtained in [Gvasaliya 05] are resumed in first three rows of column B of table 5.1. The wave-vector dependence of the bare soft mode damping and of the structure factors was not explicitly

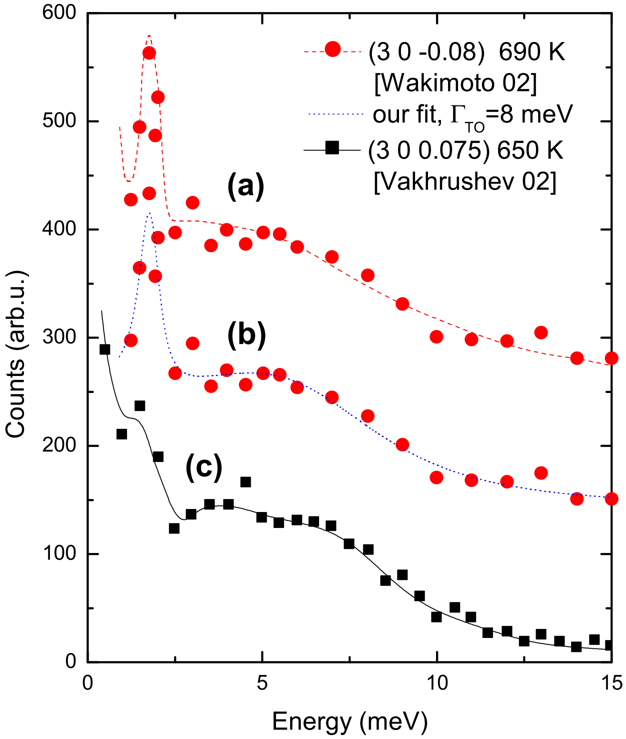

Figure 5.11: Comparison of constant-**Q** scans showing TA and TO1 modes of PMN at $\mathbf{Q} = (3, 0, q)$, $q \approx 0.5q_{\rm wf}$. Full lines are standard fits based on DHO models. (a) Data from [Wakimoto 02b], with the original fit in the spirit of the DO scenario (dashed line, $\Gamma_{\rm TO} = 13\,{\rm meV}$); (b) same data and our trial fit with a more modest damping (dotted line, $\Gamma_{\rm TO} = 8\,{\rm meV}$, broadening by the instrumental resolution neglected); (c) data and EM-scenario fit from [Vakhrushev 02]. The difference between the TA mode responses is most likely due to different resolution conditions.

parametrized in [Gvasaliya 05], but this can be performed by interpolating of the discrete values given in figure 5 and table 1 of that paper:

$$\Gamma_{\mathrm{TO}}(q) \approx 0.95 + 10.8 \sin^2(\pi q) \ , \tag{5.12}$$

$$f_{\mathrm{TA}}(q) \approx 0.25 + 0.38 \sin^2(\pi q) \ , \tag{5.13}$$

$$f_{\mathrm{TO}}(q) \approx 0.2 \ . \tag{5.14}$$

The consequent reconstruction of the corresponding $(q-\omega)$ intensity map associated with the pair of coupled branches is shown in figure 5.12a. In agreement with the conclusion of [Gvasaliya 05], the resulting picture confirms that no waterfall was present in these measurements.

In the model of [Gvasaliya 05], both $\mathbf{D}_q$ and $\mathbf{\Gamma}_q$ have nonzero off-diagonal terms. For a more appropriate comparison, one should keep in mind that $\mathbf{D}_q$, $\mathbf{\Gamma}_q$ and $\mathbf{f}_q$ cannot be determined in a unique way solely from fitting of coupled DHO spectral response to the experimental data, as it was mentioned above. To avoid this uncertainty, it is convenient to pose either $\Delta(q) = 0$ or $\Gamma_{\mathrm{AO}}(q) = 0$, which actually just means that the components of $\mathbf{D}_q$, $\mathbf{\Gamma}_q$ and $\mathbf{f}_q$ correspond to the basis where either $\mathbf{D}_q$ or $\mathbf{\Gamma}_q$ is diagonal. We have thus proceeded by transforming $\mathbf{D}_q$ and $\mathbf{\Gamma}_q$ from the model of [Gvasaliya 05] numerically at each q to the basis where $\mathbf{\Gamma}_q$ is diagonal, and the results were fitted to the same expressions postulated for dispersions.

The resulting model parameters are given in column C of table 5.1. Its spectral response is of course practically indistinguishable from the former model (column B). It seems that these recalculated parameters do not appear so much different from those of the "waterfall" model of [Hlinka 03a] (column A of table 5.1). A closer examination reveals that the main difference destroying the waterfall is the soft mode damping.

We have also tried to reconstruct in a similar way the $q - \omega$ map for the (200)-zone PMN data at 690 K, consistently analyzed by the coupled-oscillator model in [Wakimoto 02b]. We have presumed the same expression for the wave-vector dependence of $\mathbf{D}_q$, $\mathbf{\Gamma}_q$ and $\mathbf{f}_q$ as in [Hlinka 03a], except for the damping of the TO mode, which was assumed to have a form[4]

$$(\Gamma_{\mathrm{TO}})^{-1} = 0.07 + 0.28 \sin^2(\pi q) \ . \tag{5.15}$$

Data for the elements of $\mathbf{D}_q$, $\mathbf{\Gamma}_q$ and $\mathbf{f}_q$ given in table 1 of [Wakimoto 02b] are available in a rather limited interval of wave vectors ($q = 0.08 - 0.2\,\mathbf{c}^*$) only[5], but it is sufficient to adjust the small number of parameters of this

---

[4] There is no *a priori* reason to use this particular dependence, it was chosen because it well describes the shape of $\Gamma_{\mathrm{TO}}(q)$ within the DO model, see figure 5.10.

[5] We have combined the data from the (200) and (300) BZs as $\mathbf{D}_q$ and $\mathbf{\Gamma}_q$ should be independent of the BZ choice.

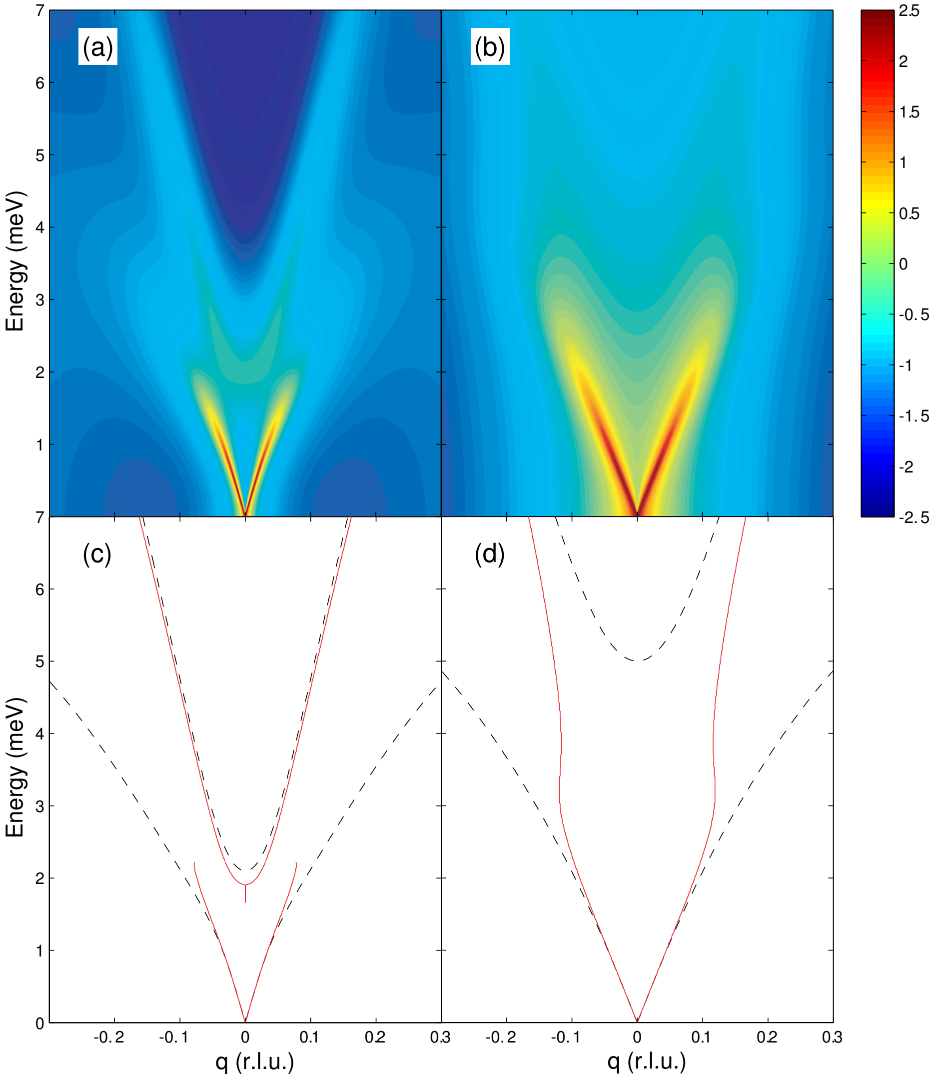

Figure 5.12: Comparison of $S(q,\omega)$ for coupled TA and TO modes (equations 5.1–**??**), as deduced from two independent experiments performed with PMN crystals at comparable conditions (similar temperature, $\mathbf{q} \parallel (001)$). The intensity maps are calculated (a) from the model of [Gvasaliya 05] (no-waterfall, 670 K), and (b) from the model fitted to data of [Wakimoto 02b] (DO model, waterfall present, 690 K). Explicit expressions used for the calculation of the $\mathbf{D}_q$, $\mathbf{\Gamma}_q$ and $\mathbf{f}_q$ matrices are given in columns C and D of table 5.1. For clarity, the maxima from constant-energy scans (full lines) are depicted in the bottom panels; dashed lines show the dispersion curves in the absence of damping. The intensity scale is logarithmic. The calculation does not take into consideration resolution effects or any other contributions to scattering cross section.

simple model. Indeed, the resulting intensity depicted in figure 5.12b shows the assumed vertical ridge of intensity. The comparison with figure 5.12a nicely illustrates the contrast between the two experiments (see also the respective dispersions in panels 5.12c,d). Moreover, the waterfall wave vector from figure 5.12d, ($q_{\mathrm{wf}} \approx 0.23$ r.l.u.), is close to the PMN value found previously in the $q \parallel 110$ experiment of [Gehring 00b]. It confirms that also in PMN the waterfall shows up for both $q \parallel 110$ and $q \parallel 100$ phonons at a similar wave vector modulus, as it was earlier demonstrated for PZN–8%PT [Gehring 00a].

In summary, the damping parameter of the TO mode is qualitatively different among various models adjusted to the experiment. The damping of the TO mode in the no-waterfall study of PMN [Gvasaliya 05] is far too small to allow for the waterfall phenomenon to occur (neither DO nor AOMI scenario is possible), cf. also figure 5.9. Moreover, resulting $S(q, \omega)$ deduced from the no-waterfall study of PMN [Gvasaliya 05] was shown to be significantly different from that deduced from other experiments, and particularly, it does not show any trace of the waterfall effect. Therefore, also the third hypothesis formulated in section 5.1 appears quite unlikely.

5.5 Comparison of measurements on different PMN samples

So far we have argued that the absence of the waterfall in the PMN experiment [Gvasaliya 05] is neither due to the improved resolution conditions, nor due to an antiresonance effect associated with the particular experimental geometry adopted and also that it is not an artefact of a biased data analysis or representation. Another possibility arises that the TO mode dynamics itself could have been different in the PMN sample used in [Gvasaliya 05]. Indeed, due to various kinds of inherent disorder (chemical, strain, polarization) in relaxor materials, it is natural that they are not in a uniquely defined equilibrium state and their properties could thus in a rather complicated way depend on the specific crystal-growth method and on the sample history. For example, Colla *et al.* [Colla 07] recently made a comparison of PMN samples grown by different methods, and show that some of them do not undergo the expected phase transition under electric field.

If we assume that the TO mode damping could be influenced by the geometric aspects of PNRs, it is equally legitimate to suspect that the absence of the waterfall might be ascribed to the sensitivity of the TO mode parameters to the sample state. In order to examine such a possibility, we

PMN	V (cm^3)	mosaic	growth method
[Dorner 03]	≈ 5	< 20'	—
[Gehring 00b]	—	—	same sample as [Naberezhnov 99]
[Gehring 01b]	0.1	—	from high-T solution with PbO flux
[Gvasaliya 05]	8	≈ 20'	—
[Naberezhnov 99]	≈ 0.5	< 40"	Czochralski
[Stock 05]	9.3	—	modified Bridgeman
[Vakhrushev 02]	—	—	same sample as [Naberezhnov 99]
[Wakimoto 02b]	0.4	—	top-seeded solution from PbO flux

Table 5.2: Information available in literature about samples of PMN from various authors.

tried to collect and directly compare equivalent spectra obtained in different experiments with different PMN samples, but keeping the same phonon wave vector $q \parallel 100$ and restricting to the even-even-even type Brillouin zone measurements where the waterfall effect is expected to occur [Hlinka 03a].

The most interesting results of such comparison are presented in figure 5.13. A number of various data is available at room temperature for transverse modes with $q = 0.2\,\mathbf{c}^*$ (figure 5.13a). Clearly, all spectra show one mode below 5 meV and another one above 10 meV, in agreement with the expectations for rough positions of the TA and lowest frequency TO modes at that q. Samples used in these measurements generally have different origin, and different methods of growth were used (see table 5.2). Despite the diverse origin of the samples,the differences in their spectra at $q = 0.2\,\mathbf{c}^*$ are rather minor. Nevertheless, a closer look suggests that the upper peak in the spectra corresponding to the no-waterfall case [Gvasaliya 05] is less damped, stronger and of a noticeably lower frequency.

This difference becomes more apparent at lower qs. At wave vectors $q = 0.12 - 0.15\,\mathbf{c}^*$, the position of the second peak in the “no-waterfall” experiment strongly shifts downwards in a similar way as the acoustic mode does, so that it keeps (due to the Bose-Einstein thermal factor) practically the same intensity as the acoustic one, while in the other experiments the upper mode does not show such a strong dispersion (figure 5.13b). The spectra taken at even smaller wave vectors ($q = 0.075 - 0.08\,\mathbf{c}^*$, see figure 5.13c) clearly show that the position of the upper peak in the two experiments differs by more than 3 meV. Similar discrepancy is also observed at higher temperatures (see figure 5.13d), because the TO mode frequency in the experiment of [Gvasaliya 05] is almost temperature independent.

Such a huge variation in the TO mode frequency could be comparable to

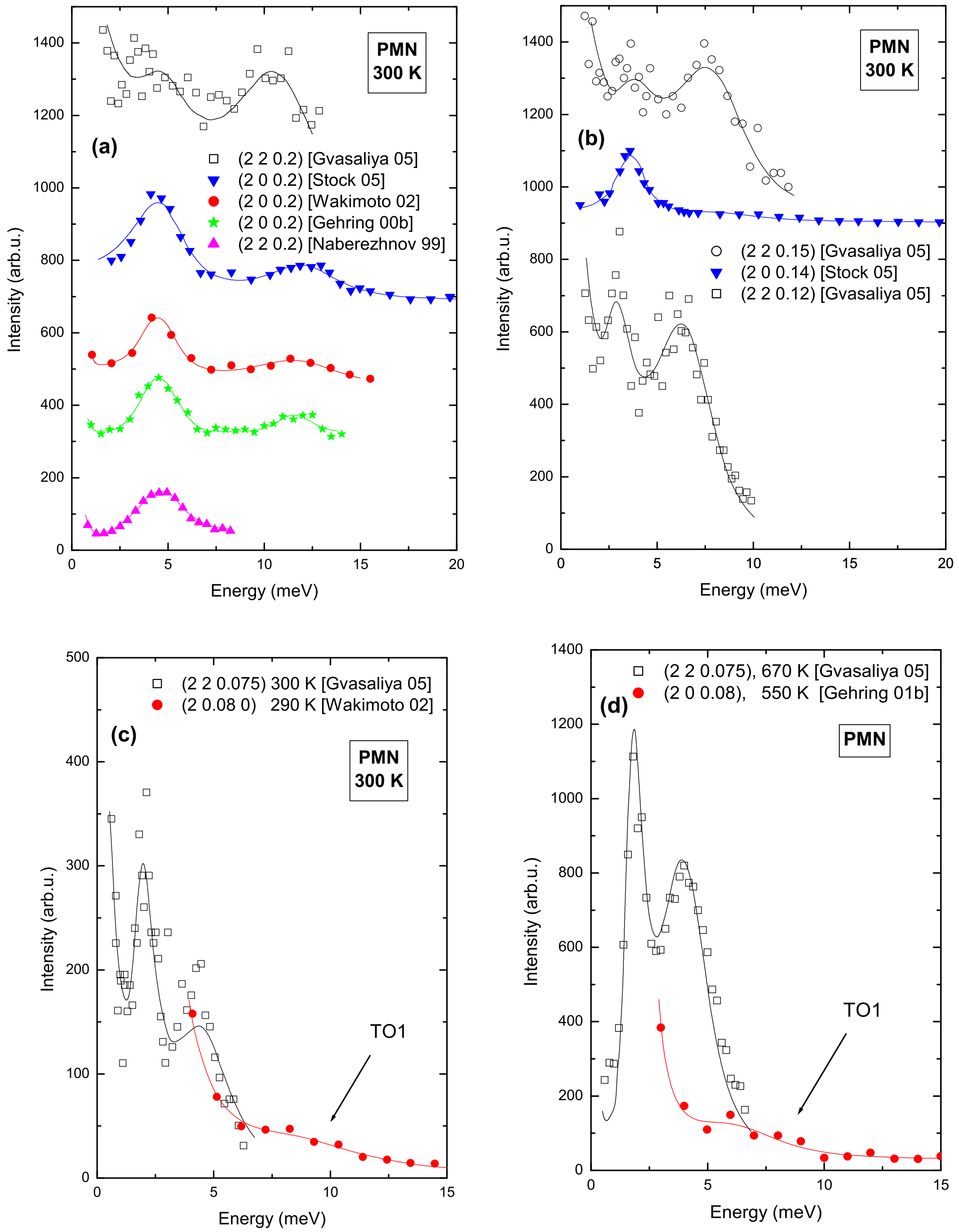

Figure 5.13: Inelastic neutron scattering spectra of PMN with $\mathbf{q} \parallel (001)$ obtained by different authors in (even/even/even)-type BZs. (a) spectra taken at $q = 0.2$ r.l.u., (b) spectra taken at $q = 0.12-0.15$ r.l.u., (c,d) spectra taken at $q = 0.075-0.08$ r.l.u. Spectra (a,b,c) are taken at room-temperature, (d) are taken at higher temperatures around 600 K. The intensity scale for the experimental data and original fitting curves in (a) was adapted so that the TA mode intensity is similar in all scans.

changes associated with some structural phase transition, but no indications[6] of any different phase or anomalous crystal structure in the specimen of [Gvasaliya 05] were reported. Therefore, it is difficult to admit that the results of the no-waterfall PMN experiment are caused by the sensitivity of the TO mode parameters to the sample preparation details.

5.6 Longitudinal acoustic mode

After we have ruled out the four simple propositions listed above, we consider to have good reasons to refuse the tacit assumption that the second lower frequency peak seen in the no-waterfall PMN experiments originates from the TO mode. Surprisingly, the most likely origin of the presumably "TO mode" seems to be a longitudinal acoustic (LA) branch.

The basic argument in favor of such assignment is the coincidence of the corresponding dispersion curves, shown in figure 5.14a. This figure resumes TO mode frequencies as obtained from different PMN experiments available in the literature. Despite a certain data spread, one can clearly see that the "TO mode" dispersion of [Gvasaliya 05] disagrees with the soft mode dispersion curves observed in the earlier experiments [Naberezhnov 99, Wakimoto 02b, Vakhrushev 02]. At the same time, it is found to be remarkably close to the LA dispersion (open circles and full line in figure 5.14a), as given in [Naberezhnov 99].

There are two other important facts strongly supporting such an assignment. First, the damping of the "TO mode" dispersion of [Gvasaliya 05] strongly increases with q (figure 5.14b), which is very unusual for a low-frequency TO mode, but normal and natural for an acoustic mode. Secondly, the no-waterfall paper [Gvasaliya 05] reports that the "TO mode" frequency is practically temperature independent, which is very unlikely for such a low-frequency TO mode. At the same time, a weak temperature dependence is completely usual for the LA mode frequency.

On the other hand, there is one principal trouble with such an interpretation. The "TO mode" was observed in the $(22q)$ point, i.e. in a typically transverse geometry, with the phonon wave vector $\mathbf{q}$ almost perpendicular to the total momentum transfer $\mathbf{Q}$. In this case, a purely longitudinal mode should not contribute to the scattering, because the expression for its INS structure factor involves multiplication by scalar product of its eigenvector with the total momentum transfer $\mathbf{Q}$ (which is zero for a pure LA mode, see equation 3.25). Still, independent low-temperature measurements on the

---

[6] In principle, PMN is known to grow also for example in pyrochlore structure, but in this case both the lattice parameters and the TO mode frequency are completely different.

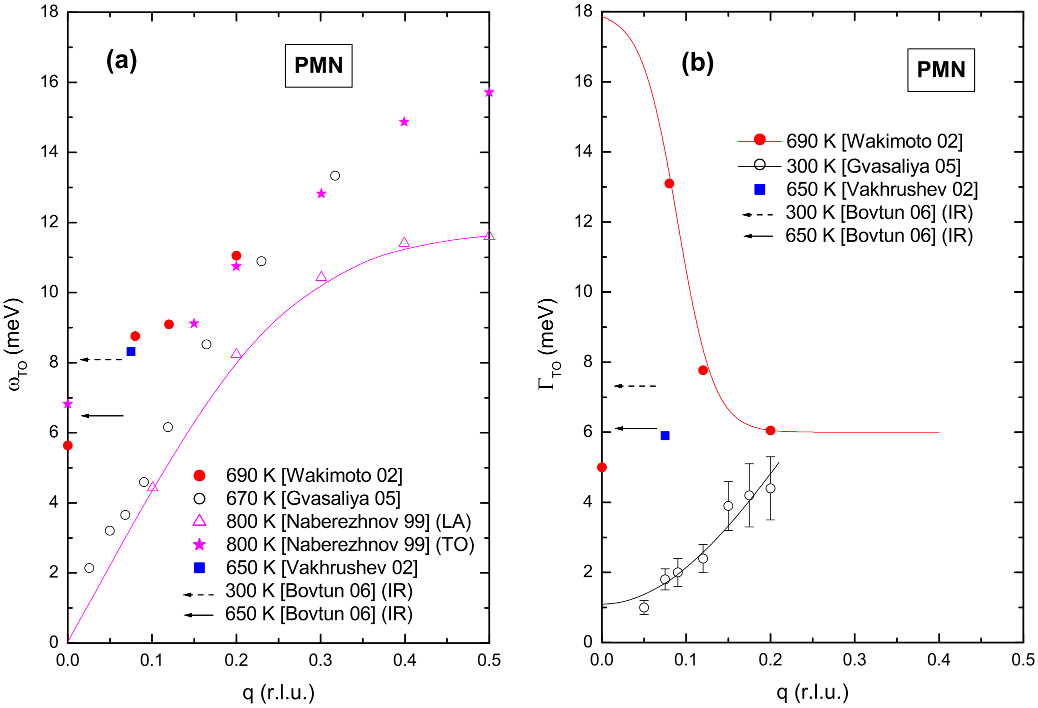

Figure 5.14: Summary of the TO mode frequency (a) and damping (b) dispersion in the (001) direction, as found in literature for PMN in the (00q) direction. Data shown here are either those obtained from independent DHO fits or they correspond to the eigenvalues of the dynamical matrix in cases when coupled DHO fits were performed. For comparison, also the longitudinal acoustic branch dispersion is appended (open triangles and a full-line guide to eye in (a)). Horizontal arrows indicate zone center frequency and damping of TO1 mode as obtained by infrared spectroscopy [Bovtun 06]. Full lines in (b) are the interpolation functions for the damping dispersion $\Gamma_{TO}(q)$ as given in columns C and D of table 5.1. They were used also in the calculation of intensity maps shown in figure 5.12.

same kind of PMN sample [Dorner 03] (see table 5.2) have also revealed longitudinal and transverse modes mixed up in certain geometries.

As a matter of fact, the transverse and longitudinal modes are probably somewhat mixed in relaxors, for example due to the inhomogeneous polarization, which locally allows piezoelectricity. Therefore, despite their macroscopically cubic average symmetry, LA modes in PMN may not be purely longitudinal, and in principle, for some reason, they may happen to scatter more strongly in the $(22q)$ experiment, which probes vibrations having nonzero displacement projections along the (110) direction (contrary to the $(20q)$ experiments).

Such intrinsic mechanism would be very interesting, but it appears to be unlikely that it could explain such a strong effect. Therefore, we could also speculate that the effect is related with some unexpected, spurious channel of neutron scattering in this particular scattering geometry. One possibility could be a multiple scattering process[7]. For example, we speculate that in the $(22q)$ experiment, the intentionally probed simple one-phonon inelastic scattering might be in competition with a combination of quasi-elastic diffuse scattering in the vicinity of the (222) Bragg reflection and subsequent inelastic scattering process in an effectively longitudinal $(0, 0, 2+q)$-type geometry (see figure 5.15), or a similar inelastic-elastic process with momentum transfer partitioning as $(22q) = (11q)+(110)$. Then, the measured intensity of the TA mode may decrease, and the LA mode may appear instead in the transverse scan. Consequently, the real TO mode need not be visible in the spectra, as its intensity is much smaller than that of the acoustic modes in the even-even-even BZs. Similar spurious elastic-inelastic and inelastic-elastic double scattering processes are sometimes noticed in INS experiments, for example in [Brockhouse 62, Ivanov 84].

We thus can conclude that the recent $(22q)$ no-waterfall measurements do not show the waterfall effect because the true TO response is masked by the response of the LA mode there. However, the reasons for the appearance of this LA mode are so far a matter of speculations.

5.7 Discussion

The discussion about the waterfall issue has brought to the fore a very important question - whether and how the PNRs (or, in general, inhomogeneous polarization fluctuations) do influence the soft mode dynamics in relaxors.

---

[7] The multiple scattering process could have taken benefit from the considerable size ($V \approx 8\,\mathrm{cm}^3$) and small mosaic (20' [Gvasaliya 04]).On the other hand, similar LA-like "TO-mode" was observed also in a smaller ($V \approx 1\,\mathrm{cm}^3$) crystal of PMN–32PT [Gvasaliya 07].

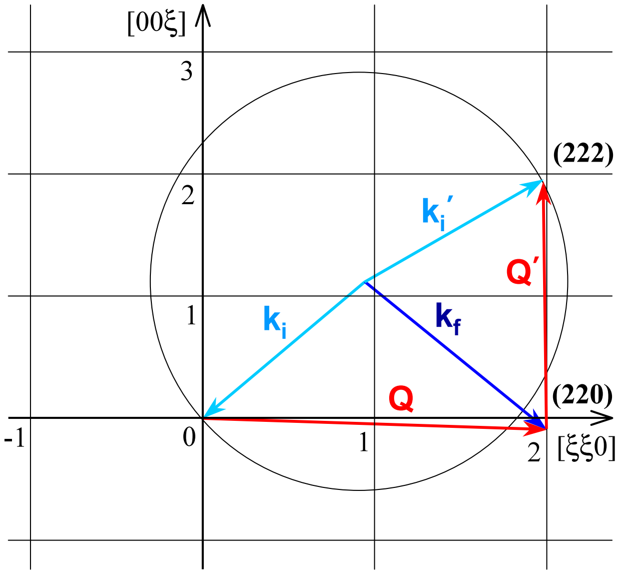

Figure 5.15: Proposition of the explanation of possible scattering by LA modes in the transverse geometry. Thanks to finite resolution and e.g. diffuse scattering, the process with an alternative triangle (k_i', k_f, Q') may be realized.

So far, it was mostly speculated that PNRs may considerably increase the damping of the soft mode. From the available data, it seems established that the TO soft mode in relaxors has a sizable damping (in room-temperature PMN it is of the order of at least 5 meV, see figure 5.14b). For a disordered solid solution, this is not so unusual, but it is possible that the DO scenario (a sudden increase in the soft mode damping below a particular wave vector q_{wf}) cannot be ruled out by the fact that q_{wf} depends on the geometry of the INS experiment [Hlinka 03a]. In fact, it seems that a hybrid DO/AOMI model may turn out to give a more appropriate description of the data than the original DO or AOMI models could do. However, if such a sudden damping increase exists, then for example in PMN the peak damping is probably less than 10 meV, and it has to decrease again near the zone centre since there the TO mode damping estimations from both INS and infrared reflectivity techniques are rather moderate (5-7 meV, see figure 5.14b); consider also value of $\Gamma_{\mathrm{TO}} = 5$ meV at $q = 0$ [Wakimoto 02b] in figure 5.14b. In any case, so far there is no really convincing evidence in favour of the DO idea, and a detailed study devoted to the wave-vector dependence of the TO mode damping remains as a task for future.

It was argued [Hlinka 06c] that the dielectric response due to the polar phonon modes in PMN-type relaxors can be consistently interpreted assuming that the polar phonon mode triplets are split by the inhomogeneous polarization. In the case of PMN, it was concluded that in the first approximation, the TO soft mode can be viewed as split into two components [Hlinka 06c]: the first one, associated with axial vibrations and assigned as the A_1 component, can be identified with the "zone-centre TO mode" investigated in detail by INS in the (200) BZ in [Wakimoto 02b], because it has essentially the same temperature dependence of the frequency and damping (at room temperature, frequency about 8 meV and damping about 4 meV). The latter IR-active mode, assigned as the E_1 component of the TO mode triplet, has a response of a strongly damped DHO or a Debye relaxator (with relaxation frequency of about 4 meV) and it should correspond to what is called broad diffuse scattering in the INS community.

At finite wave vectors q, both A_1 and E_1 components are expected to be coupled to the transverse acoustic modes of the corresponding symmetry, as for example in ferroelectric $BaTiO_3$. The systematic analysis of the coupling between the broad diffuse scattering and the TA branch [Stock 05] fits well to this picture. It would be very interesting to disentangle the relative importance of the A_1 and E_1 couplings to the resulting TA mode response, and even more to the LA response, which is allowed in the polar phase. However, the situation is far from being clear at present.

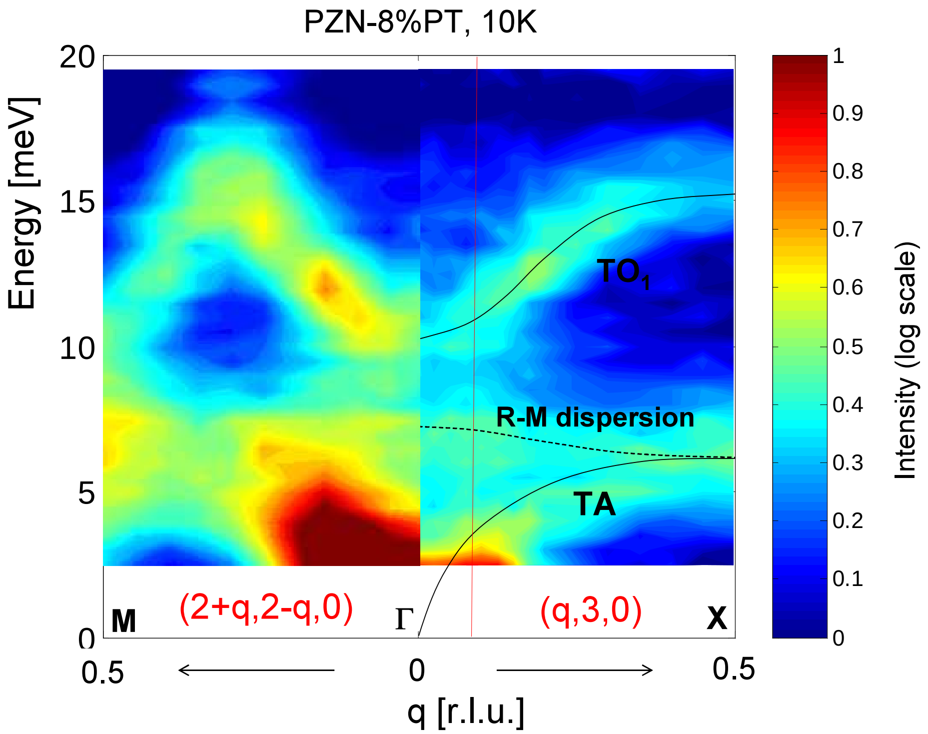

Figure 5.16: Intensity map of phonon branches in PZN–8%PT in the [110] and [100] symmetry directions. The full lines show the fitted TA and TO dispersions, the dashed line shows the R–M dispersion, as will be explained below. The intensity scale is logarithmic and arbitrary, but keeping the intensity ratio between the two BZs.

5.8 The nature of the second soft mode in PZN–xPT

In this part, we discuss the origin of an extraneous underdamped excitation near 7 meV (between the acoustic and the lowest optic phonon branch), accidentally spotted in our low-temperature measurements on PZN–8%PT (figure 5.16) in the (020) and (030) Brillouin zones (BZs).

There have been numerous propositions how to explain this additional signal:

- The idea of a spurious effect was excluded since this mode has been observed also in far-infrared spectra.
- The intensity of the excitation in INS spectra appears to vanish for $q > 0.2$ r.l.u. which suggests that it could be a genuine mode related to polar nanoregions (PNRs).

- The observed mode could be folded R-point zone boundary mode, activated in the zone centre by NaCl type ordering on the B-site (of the ABO_3 perovskite structure)

- Many other possibilities, such as the "quasi-optic mode" [Vakhrushev 02], "fracton" [Lushnikov 99] or "breather" [Bussmann-Holder 04].

In order to elucidate the nature of this signal, we used crystals of PZN–4.5%PT poled in electrical field along the (111) direction, for INS experiments on the IN22 and IN3 ILL's thermal spectrometers. The samples were mounted, contrary to our previous experiments, with the (110) axis vertical, in order to access the [111] direction, mainly the R points. The measurement was performed at 10 K and 300 K.

Poling of the crystals could help to decide if the extraneous mode was really directly caused by the nanoscopic size of PNRs. If this was the case, the intensity or q-range of its visibility should significantly decrease in the poled sample. Due to the interest in domain engineering, the poling techniques have been recently significantly improved [Zhang 03, Ogawa 03] so that relatively large crystals can be homogeneously poled. We chose poling that prefers single domain polarization so that the volume corresponding to truly nanoscopic polar regions is significantly reduced.

The inelastic spectra taken in the experiment clearly allowed us to demonstrate (figure 5.18) that this mode has the same frequency as the pronounced excitation from the BZ boundary (R point) and that it activates in the vicinity of the Γ point because of breaking of the translation symmetry (see figure 5.17). This symmetry breaking is caused by ordering on the B-sites, which doubles the unit cell[8].

The investigation of R-point spectra in the directions parallel and roughly perpendicular to the poling direction shows that the above described vibration has a transverse character (see figure 5.19): its intensity is significantly lower in the poling direction $\mathbf{Q} = (1.5\ 1.5\ 1.5)$.

The results were complemented by investigating the phonon branches in the principal pseudocubic directions. The result is depicted in figure 5.20. From there, we can conclude that:

---

[8] In figure 5.18 we do not compare exactly equivalent spectra. Firstly, BZ boundary corresponds to BZ centre, which is not represented in the figure. It is not always easy to get a pronounced signal there, because of stronger elastic incoherent signal and contributions to the scattering intensity from all directions. However, because of the flat R–M dispersion (figure 5.20), the mode at $\mathbf{Q} = (1.5\ 1.5\ 1.5)$ would only be slightly shifted towards higher frequency.

Secondly, the different sample compositions (x) can also be neglected.

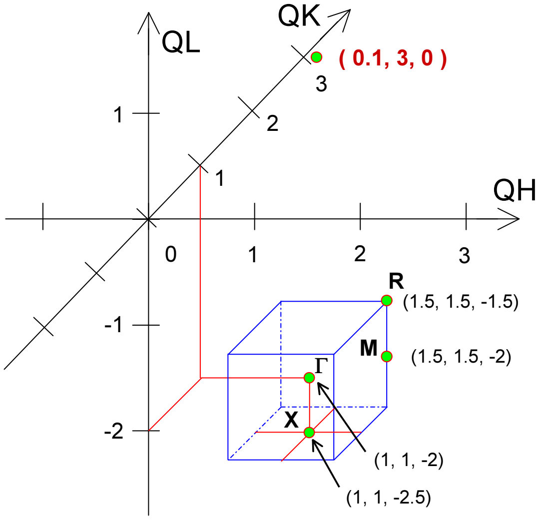

Figure 5.17: Schematic representation of the discussed points in the reciprocal space.

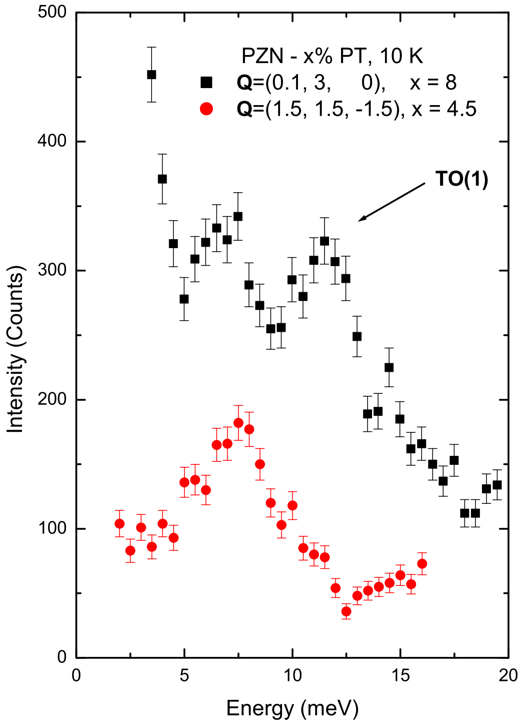

Figure 5.18: Zone-boundary TA phonon mode (circles) compared with the extra mode at ≈7 meV near the BZ centre (squares).

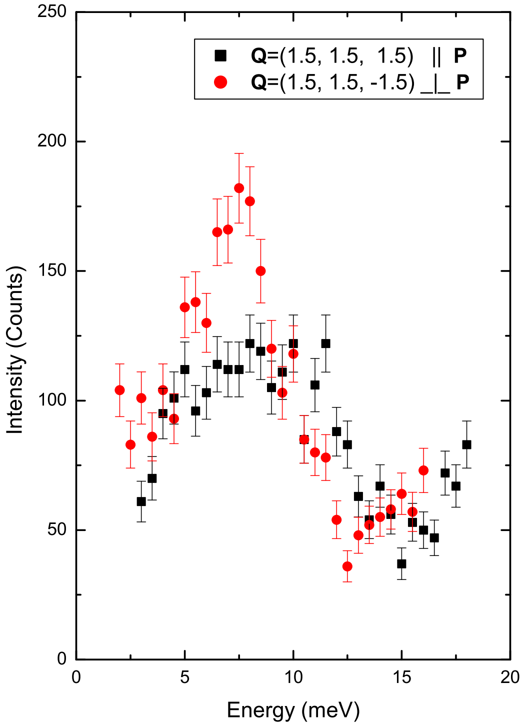

Figure 5.19: Comparison of spectra from the R-points in the directions parallel (squares) and perpendicular (circles) to the poling direction.

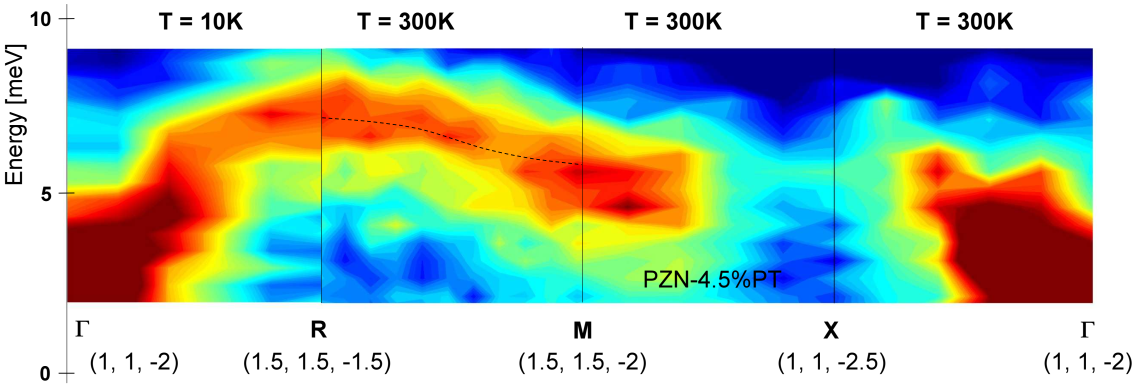

Figure 5.20: Intensity map of phonon branches in poled PZN–4.5%PT in principal symmetry directions. The dashed line shows, for convenience, the fitted R–M dispersion. The intensity scale (not shown) is logarithmic, and arbitrary between different temperatures (correcting the Bose factor).

- Zone boundary TA modes do not show pronounced temperature dependence between 300K and 10K.
- The excitations seen in the M and R points belong to the same phonon map, which is a continuation of the transverse acoustic branch.

5.9 Forbidden Raman scattering in PZN–8%PT

As was mentioned in chapter 2, the macroscopic structure of perovskite relaxors (at high enough temperatures) is cubic (Pm$\bar{3}$m), in which the first-order Raman active modes should not exist. Polar nanoregions (PNRs), which are formed already few hundreds K above the dielectric anomaly, can at nanoscale cause the symmetry breaking on both sides of the dielectric anomaly, and Raman scattering is in principle sensitive to the local order at nanometer scale [Siny 99, Guttler 03]. However, experimental data show typically quite strong Raman vibrational spectra (see figure 5.21) which persist far above the temperature of dielectric relaxation [Siny 99, Kamba 03].

The activation of the forbidden Raman active modes can be caused for example by NaCl-type occupational ordering at the B sites of the ABO_3 perovskite structure. The activated modes from the zone-boundary R-point can be then classified as zone-center modes of the Fm$\bar{3}$m ordered structure (doubled unit cell). In a number of mixed perovskite systems with 1:1 average occupation at the B-sites (like PST), this NaCl ordering was directly

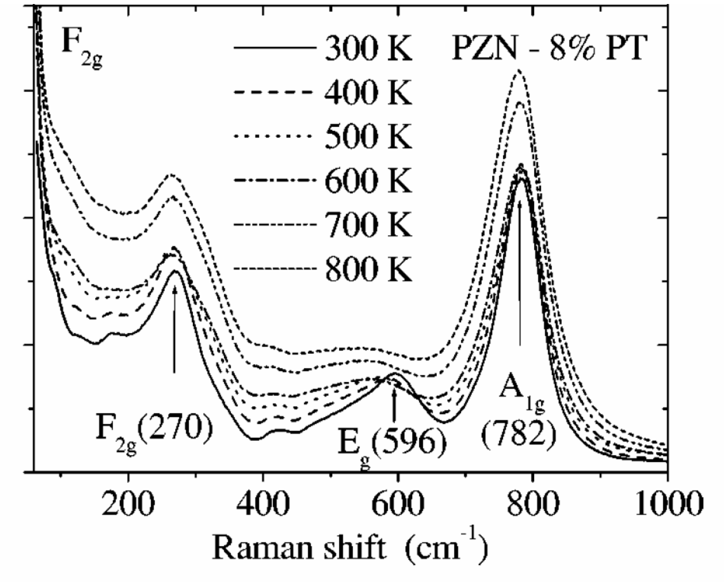

Figure 5.21: Temperature dependence of unpolarized Raman spectra of PZN–8%PT with the standard assignment [Siny 99, Guttler 03]. Copied from [Kamba 03].

evidenced by diffraction methods [Dmowski 00], and Raman scattering show indeed quite clearly the 4 expected modes from the Fm$\bar{3}$m group symmetry analysis [Guttler 03]. The same type of ordering, though more short-range and much weaker was observed also in compounds with 1:2 average occupancy at B-sites (e.g. in PZN and PMN).

There is also another possibility, that the Raman scattering in lead relaxors with 1:2 stoichiometry is primarily due to the polar ordering itself, as proposed in [Iwata 00]. In that case, the spectra could be assigned to zone centre modes of the ferroelectrically distorted perovskite structure [Iwata 00] instead of the assignment based on unit cell doubling [Siny 99, Guttler 03]. Moreover, the "zone-centre" assignment would give a very natural explanation of the temperature dependence of Raman intensity, which follows the amplitude of Pb displacement [Egami 03].

Unfortunately, ab-initio techniques are not yet capable to perform lattice dynamics of large supercells necessary to describe properly the B-site correlations, so another experimental technique, besides Raman scattering, has been highly needed here. INS is probably the best tool since it can simply distinguish zone centre and zone boundary modes by scattering geometry.

We focused our study on the longitudinal [111] (Γ–R) dispersion of the principal Raman band near 97 meV (780 cm^{-1}, figure 5.21) generally assigned

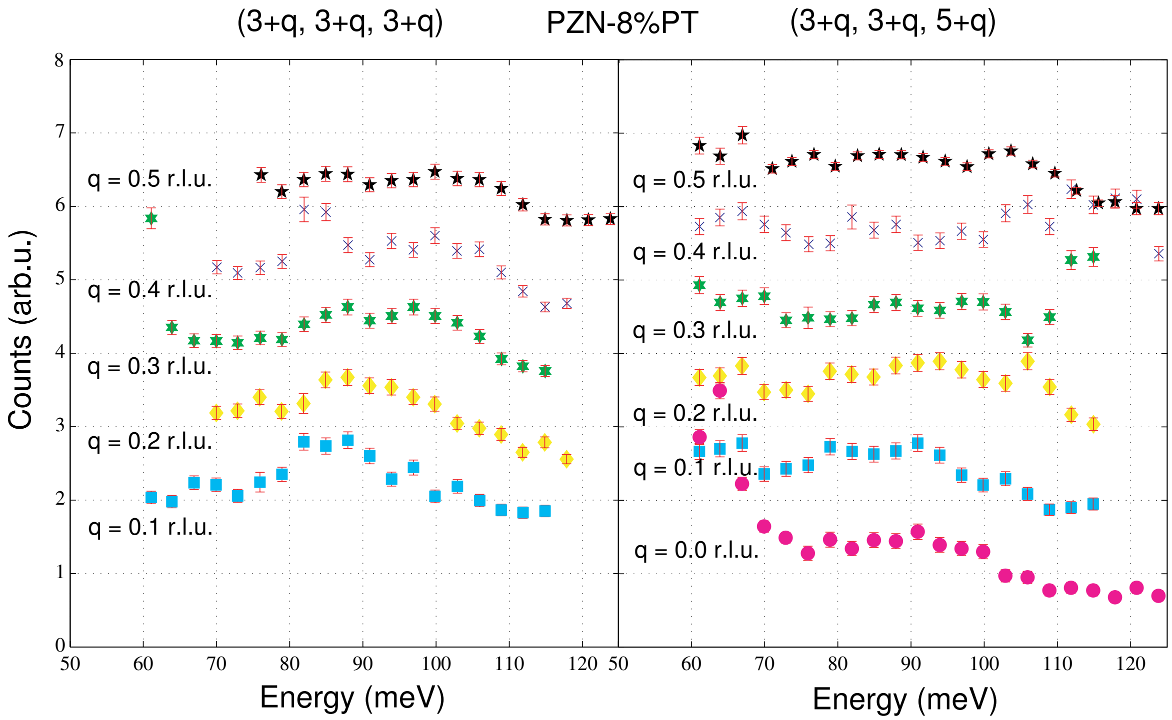

Figure 5.22: The [111] dispersion of PZN–8%PT at high energies and in two BZs. Note: The increased signal in the (3 3 5) Γ-point at 65 meV is a spurious effect - an elastic $k'_f = k_i$ process from the (445) Bragg point (see figure 4.10 and section 4.4).

to A_{1g} antiphase breathing of neighbouring oxygen octahedra [Siny 99, Guttler 03]. According to [Iwata 00], this Raman band should be the true longitudinal zone-centre mode; the comparison with virtual crystal approximation calculations for PMN (see figure 3 of [Gvasaliya 03]) suggest that the true A_{1g} antiphase breathing mode might then fall around 112 meV.

Previous INS studies of relaxor ferroelectrics concentrated mostly on the lower-frequency excitations (up to 30 meV). The INS experiment presented here was conducted on the IN1 ILL's hot-source spectrometer, in the range of energy transfers 60–125 meV. The sample, a crystal of PZN–8%PT, studied also in [Iwata 00], was mounted with the (110) axis vertical, in order to access the [111] direction. The measurements were performed at 300 K or 10 K (in the following, temperature will not be discussed, as we did not observe any distinct change with temperature in the spectra).

At the energy transfers of ≈100 meV the counting rate of neutrons is quite low (compared to, e.g., energy transfer of 10 meV) even on the hot source. This implied relatively long counting times (of the order of 30 min per point

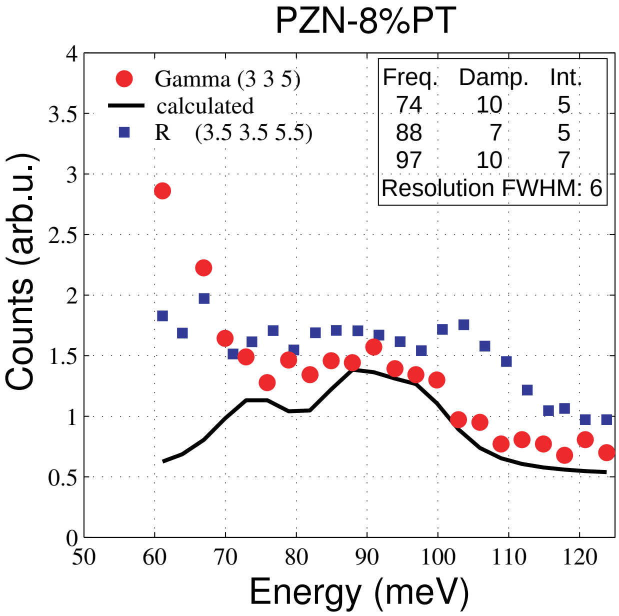

Figure 5.23: Selected Γ- and R-point energy spectra, compared with the calculated curve described in the text.

and 10 hrs per spectrum), and consequently higher noise. Measuring at such high energies means also a relatively high energy resolution width (FWHM ≈6 meV), more spurious peaks in the spectra (caused by relatively high Q-transfers, where the probability of crossing the Ewald sphere is higher) and high background (mostly from multi-phonon contributions).

Because of these reasons, we were not able to identify individual phonon branches and their dispersion, except the so far unknown mode going from 90 meV (Γ-point) to 104 meV (R-point), traceable in figure 5.22. Nevertheless, the spectra collected in different BZs show (figure 5.22) that the Raman mode at 97 meV is not activated from the BZ boundary (as was the case of the extraneous excitation near 7 meV, see section 5.8).

Despite the difficulties described above, the results are in qualitative agreement with IR and Raman spectra. Three high-frequency modes observed in IR (74 and 88 meV) and Raman (97 meV) measurements [Kamba 03], with their dampings, arbitrarily chosen intensities and convoluted with simple 1D Gaussian resolution function, reproduce well a broad feature around 90 meV from the INS Γ- and R-point spectra (see the calculated curve in figure 5.23, together with the values used). The intensities of the modes can be chosen arbitrarily because the INS structure factors are in principle different (and changing with BZ).

Chapter 6

Inelastic scattering studies of $PbTiO_3$

6.1 Introduction

Lead titanate $PbTiO_3$, one of the prototype perovskite ABO_3 ferroelectrics, is a model example of the displacive phase transition. It is an end member compound of lead-based perovskite relaxor ferroelectrics, such as (1-x)$Pb(Zn_{1/3}Nb_{2/3})O_3$–x$PbTiO_3$(PZN–xPT), (1-x)$Pb(Mg_{1/3}Nb_{2/3})O_3$–x$PbTiO_3$ (PMN–xPT), $Pb(Zr_{1-x}Ti_x)O_3$ (PZT). Despite recent trends to minimize the amount of Pb in technological applications, there still has not been found any adequate substitution, that would exhibit comparable material properties.

$PbTiO_3$, unlike many other perovskite ferroelectrics, undergoes with temperature only one structural phase transition from the high-temperature parent cubic phase (Pm3m) to the tetragonal ferroelectric phase (P4mm) at $T_C \approx 760\,\mathrm{K}$ [Lines&Glass]. This relatively high phase-transition temperature leads to a large spontaneous strain ($c/a = 1.06$ at 300 K [Shirane 50], and becoming even higher at lower temperatures).

The phonon soft mode, corresponding to this phase transition, is driven by Pb atom vibrations against the TiO_6 octahedra [Last 57]. It softens (decreases its frequency with temperature) when approaching T_C [Remeika 70]. As a case of the 1^{st} order phase transition, the soft mode frequency obeys the Curie-Weiss law $\omega_{SM}^2 \propto 1/\varepsilon' \propto (T - T_0)$ with the Curie-Weiss temperature $T_0 \approx 722\,\mathrm{K}$. At the same time, the dielectric constant ϵ' exhibits a sharp peak at T_C [Remeika 70].

Phonon dispersion curves of $PbTiO_3$ at ambient pressure have been investigated by several first-principles calculations (e.g. [Zhong 94, Garcia 96, Waghmare 97, Ghosez 99]), but until recently, the experimental data were rather limited (mainly due to the lack of single crystals of high quality and large enough for INS measurements). Recently, new experiments [Tomeno 06, Hlinka 06a, Kempa 06a] have been conducted in order to complement the early inelastic neutron scattering study of Shirane *et al.* [Shirane 70a]. Lattice dynamics have also been investigated by Raman spectroscopy [Burns 73, Burns 76a, Fontana 91, Foster 93, Cho 01] and by IR spectroscopy [Perry 64, Tornberg 70, Fedorov 95].

It is highly desirable to understand the dynamical properties of $PbTiO_3$, mainly because as a model ferroelectric, it has been a starting point for studying more complex systems. Moreover, as already mentioned, it is an important material used to dilute other complex lead-based perovskites to increase their piezoelectric properties by bringing them closer to the morphotropic phase boundaries of their phase diagrams (see chapter 2).

6.2 INS studies of the $PbTiO_3$ lattice dynamics

The samples used in our INS measurements were high-quality single crystals, grown by the flux method: The PbO-B_2O_3 system was used as a solvent and the crystallization was carried out in the temperature range of 1325-1175 K with a cooling rate of 0.7 K/h. More details are given in [Kania 06]. No ferroelastic domain walls were seen under the polarized light microscope and neutron diffraction has confirmed that the tetragonal axis c was perpendicular to the platelet in at least 95% of the sample volume.

The INS experiments were carried out on the 1T thermal neutron three-axis spectrometer at the ORPHEE reactor of the Laboratoire Leon Brillouin, CE Saclay. The instrument was operated in its standard configuration, using horizontally and vertically focusing monochromator and analyzer crystals (PG 002) together with a natural collimation. The measurements were performed at a fixed energy of scattered neutrons ($E_f = 14.7\,\mathrm{meV}$) with a pyrolytic graphite (PG) filter in front of the analyzer. A typical full width at half maximum (FWHM) energy resolution was ≈1 meV.

In the room-temperature INS experiment, the sample was mounted with its c axis (001) either horizontal or vertical, in order to access the transverse modes polarized parallel as well as perpendicular to the spontaneous polarization direction. At high temperatures, the sample was put in a Nb pocket, and mounted into a furnace with its c axis horizontal.

sym. point	point group	irreducible representations (basis)
Γ, Z	$4mm$ (C_{4v})	$4A_1$(Pb,Ti,O)$\oplus B_1$(O)$\oplus 5E$(Pb,Ti,O)
X	$mm2$ (C_{2v})	$5A_1$(Pb,Ti,O)$\oplus 3A_2$(Ti,O)$\oplus 2B_1$(Pb,O)$\oplus 5B_2$(Pb,Ti,O)
M, R	$4mm$ (C_{4v})	$2A_1$(Pb,O)$\oplus A_2$(O)$\oplus B_1$(O)$\oplus 3B_2$(Ti,O)$\oplus 4E$(Pb,Ti,O)

Table 6.1: Symmetry analysis of normal modes in tetragonal $PbTiO_3$ at symmetry points of the Brillouin zone; taken from [Freire 88].

6.2.1 Phonon dispersions in the tetragonal phase

At room temperature, we have collected quite complete low-frequency data in the [100] and [001] tetragonal symmetry directions (the [111] direction is missing, due to the chosen orientation of the sample in the furnace). Examples of such scans are displayed in figure 6.1.

The data were fitted with a superposition of independent (uncoupled)[1] damped harmonic oscillators

$$I \propto \frac{n(\omega)}{(\omega^2 - \omega_i^2)^2 + \omega^2\,\Gamma_i^2} \tag{6.1}$$

(ω_i and Γ_i denoting the frequency and damping of the mode, $n(\omega)$ the Bose factor – equation 3.24), together with a slowly varying background, convoluted with a four–dimensional Gaussian instrumental resolution function $R(\mathbf{Q}, E)$, assuming a locally linearized dispersion relation and using the program packages AFITV [Hennion] and RESTRAX [Kulda 96]. Both fitting programs converged to the same phonon frequencies. A relatively high but smooth and monotonic inelastic background was held almost constant for all spectra.

As a result, the phonon frequency dispersions are summarized in figure 6.3a,c. Labelling of the dispersions is done with the usual Bouckaert-Smoluchowski-Wigner [Bouckaert 36] notation as described in [Altmann 65], the correspondence with the Mulliken notation is given in figure 6.3. Symmetry analysis of phonon vibrations of ferroelectric $PbTiO_3$ can be found, e.g., in [Garcia 96, Freire 88] – see table 6.1.

Mode assignments are based on the fact that the inelastic structure factor scales with a scalar product of the phonon eigenvector and the momentum transfer $\mathbf{Q}$. For example, the representative neutron spectra corresponding to the transverse optic (TO) modes displayed in figure 6.1 were taken at

---

[1] In this case, the value of the coupling was negligible when included into the model, and did not influence other values.

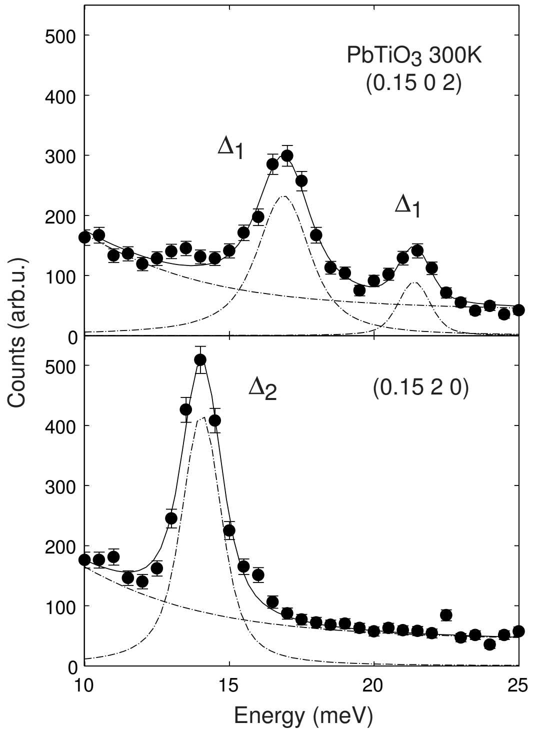

Figure 6.1: Inelastic neutron scattering spectra from constant-**Q** scans with momentum transfers of (0.15 0 2) and (0.15 2 0), revealing the Δ_1 (top) and Δ_2 (bottom) transverse optic modes. Point symbols stand for the data points, the solid line corresponds to the fit with the damped harmonic oscillator model, the dashed lines represent the individual components of the model.

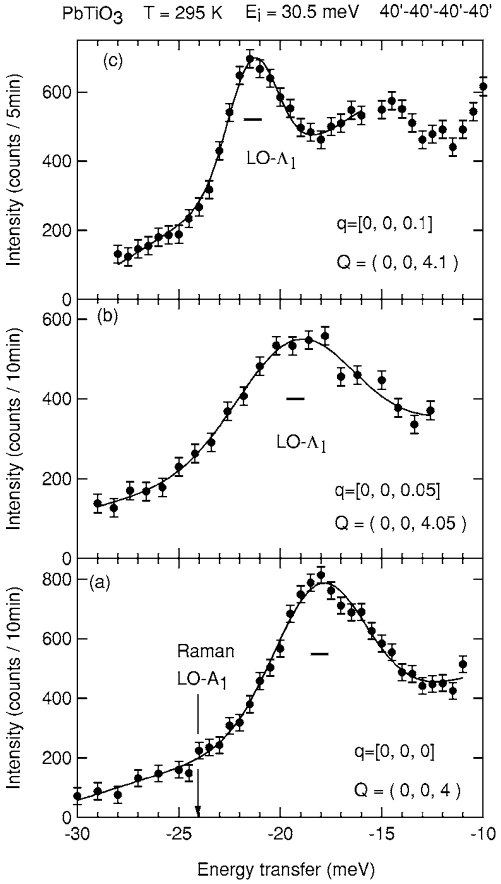

Figure 6.2: INS spectra of the LO-Λ_1 phonons, copied from [Tomeno 06]. The horizontal bars indicate the instrumental resolutions. The arrow denotes the Raman data for the LO-A_1 phonons taken from [Foster 93].

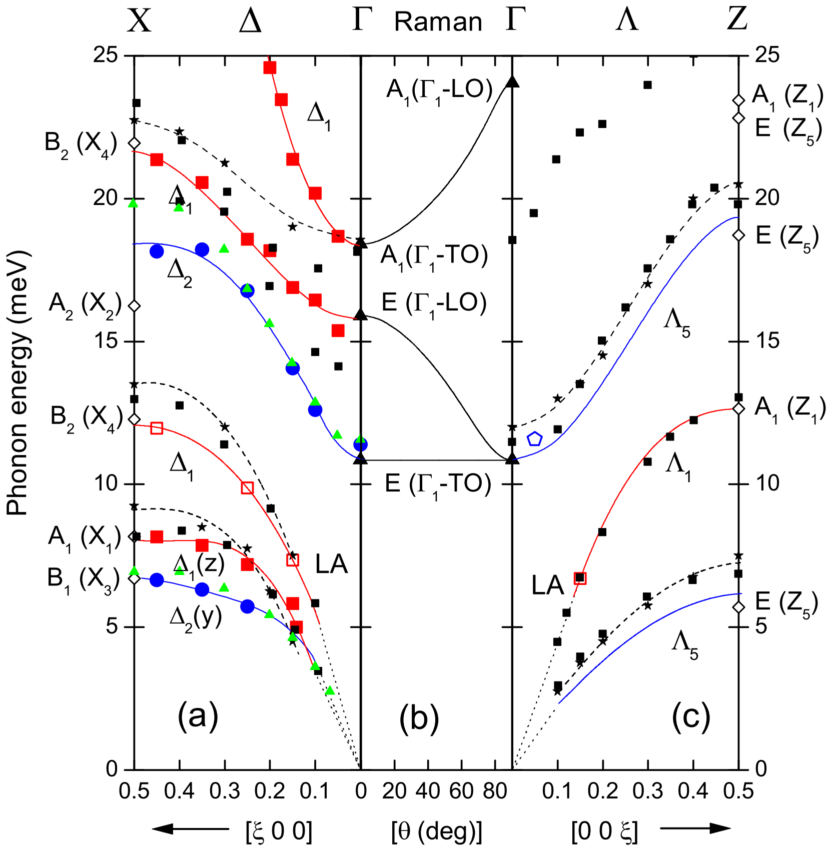

Figure 6.3: Low-frequency phonon dispersion curves of $PbTiO_3$ at room temperature. (a) Dispersion relation along the [100] direction. (b) Angular dispersion of long-wavelength modes with wave vectors rotating from [100] to [001] direction. (c) Dispersion relation along [001] direction. Larger symbols stand for the data from our study (open squares: Δ_1 and Λ_1 longitudinal acoustic branches, solid red squares: Δ_1 transverse acoustic (TA) branches, solid circles: Δ_2 branches, open pentagon: Λ_5 mode), smaller symbols are from literature (solid triangles: Raman experiment [Foster 93], stars and full black squares: inelastic neutron scattering [Shirane 70a, Tomeno 06], open diamonds: ab-initio results [Garcia 96]. Dotted lines stand for linear acoustic dispersion extrapolated from Brillouin experiments [Li 96, Kalinichev 97], dashed and solid lines are guides for the eye.

momentum transfers of (0.15 0 2) and (0.15 2 0) so that the corresponding mode eigenvectors are expected to have significant projections onto the (001) and (010) directions, respectively. Consequently, they can be assigned to Δ_1 and Δ_2 species, respectively.

Close to the BZ centre, the determined optic branches (see figure 6.3a) correspond very well with the E(TO), E(LO) and A_1(TO) modes known from Raman experiments [Foster 93]. The angular dispersion calculated according to Raman spectroscopy data from [Foster 93] is shown in figure 6.3b).

Similarly, the low-q slope of the acoustic branches fits well with the limiting long-wavelength slopes determined from Brillouin experiments [Li 96, Kalinichev 97] (see figure 6.3a). Here, it is interesting to note that the observed y-polarized Δ_2 TA modes have lower frequencies than the z-polarized Δ_1 TA modes, even though Brillouin scattering results show that at long wavelengths the situation is just the opposite ($C_{66} > C_{44}^D$). This implies an upward bending of the Δ_1 TA branch and crossing of the two TA modes at some finite wave vector. Such upward bending of the Δ_1 TA branch was already observed [Shirane 70b] in tetragonal $BaTiO_3$.

Also, the experimentally determined zone-boundary frequencies are in a remarkable agreement with the *ab-initio* calculations [Garcia 96] (figure 6.3), probably due to the fact that the anharmonic effects are quite small at room temperature in this crystal.

Comparing our results with the data obtained in the earlier inelastic neutron scattering studies [Shirane 70a], also displayed in figure 6.3, we have to bear in mind that probably, contrary to the present work, no measurement was done for sample orientation with the c axis vertical. Consequently, the transverse Δ_1 species were not observable in that study. The absence of the second optic branch in the previous results is more puzzling. But it is possible that the dynamic structure factor of the missing modes was too small in the Brillouin zone used for their measurements. At the same time, it appears that all of the previously measured frequencies are systematically by about 10-15% higher than the present ones.

Part of the differences in the mode frequencies is most probably just due to the different methods of data analysis. Indeed, the 1050 K zone centre spectrum shown in figure 2 of [Shirane 70a] is almost the same as our spectrum taken at the same temperature. These data can be fitted with the DHO response having frequency of about (7.5 ± 0.3) meV (see figure 6.12). At the same time, the intensity maximum of such damped harmonic oscillator response itself is close to 6 meV, which is the value reported in [Shirane 70a].

It is clear that fitting such energy spectra using a simple Gaussian function gives systematically lower phonon frequencies. The difference becomes more distinct for higher temperatures and larger Γ_{TO}/ω_{TO} ratio. We tried also the opposite approach - to estimate the SM energy by fitting the data from figure 2 of [Shirane 70a] with a DHO convoluted with a standard (1-dimensional) resolution function. The effect of the resolution "raised" the value to (6.6 ± 0.3) meV, which is already closer to our result.

Similar arguments can be applied to the recent study of Tomeno *et al.* [Tomeno 06], a room-temperature study, to some extent complementary to our results. They probably also applied simple fitting without correction to resolution. However, without knowledge of the resolution function $R(\mathbf{Q})$ and of the BZ explored in other studies, we cannot make any definite conclusion about the differences.

As a remark, we argue that the spectra shown in figure 10 of [Tomeno 06] (see figure 6.2) do not represent the same LO–Λ_1 phonon mode. The main reason is the inconsistence of the mode damping with increasing q. The broad peak in figure 10(b) can be rather explained as a capture of another phonon mode from a different symmetry direction.

The dispersion of the LA Λ_1 branch (figure 6.3c) can be well guessed by interpolating between the long-wavelength slope from Brillouin experiments [Li 96, Kalinichev 97] and the *ab-initio* predicted [Garcia 96] frequency of the associated zone-boundary mode (from our experiment,we have determined one additional point, see figure 6.3c). Most likely, the Λ_5 phonon frequencies of [Shirane 70a] are also overestimated by 10-15%. For example, the measurement of the Λ_5 TO mode at $\mathbf{Q}$=(2 0 0.05) gives a phonon frequency much closer to the Raman value [Foster 93] of the E(TO) mode than to [Shirane 70a]. The shift by 15% of the Λ_5 phonon data is indicated by solid lines drawn in Fig. 6.3c.

6.2.2 Phonon dispersions in the cubic phase

The most complete high-temperature investigation was carried out at 775 K, i.e. in the cubic phase, about 15 K above the phase transition. Schematic intensity maps in the $(\mathbf{Q} - \omega)$ space, drawn from such scans, are displayed in figure 6.4 (the corresponding directions in the reciprocal plane are schematically drawn in figure 6.5). Phonon dispersion curves measured at this temperature along the $\Gamma - X$, $\Gamma - M$ and $X - M$ directions in the (0 0 2) BZ are shown in figure 6.6, together with the available data from [Shirane 70a].

Certain phonon branches were measured also at 975 K. For example, the TO soft phonon mode along the [ξ00] direction (not shown in figure 6.6 at this temperature) follows the identical dependence, and differs from 775 K only in the vicinity of the BZ centre (for the discussion of the SM softening with temperature, see section 6.2.3).

The energy spectra at both temperatures were fitted with a model of

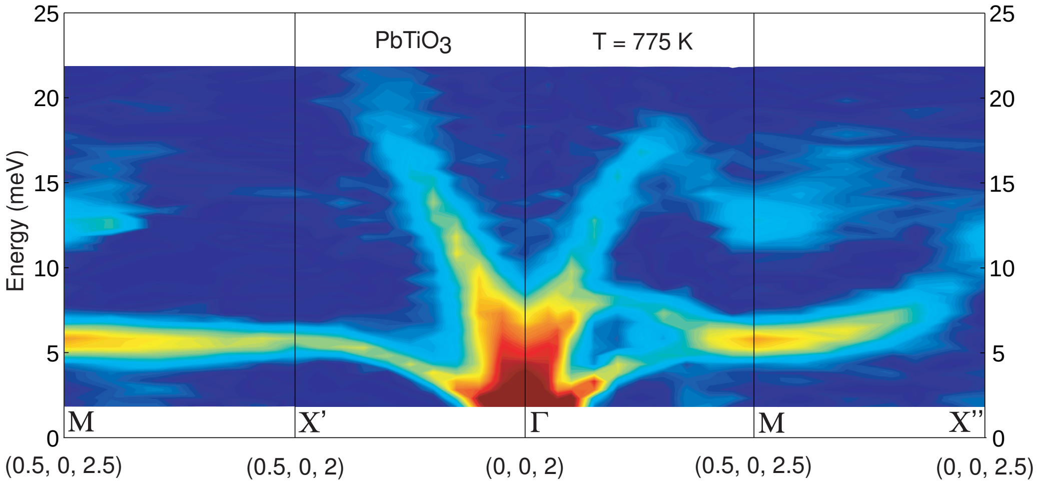

Figure 6.4: Intensity map of phonon branches in $PbTiO_3$ in most of principal symmetry directions. The X-points are equivalent and are distinguished only for the sake of clarity. The intensity scale (not shown) is logarithmic.

uncoupled damped harmonic oscillators (DHOs), convoluted with a 4D instrumental resolution function, in the same way as in section 6.2.1. The fitting was performed with the RESTRAX package [Kulda 96]. Rather detailed analysis was carried out with data corresponding to the lowest two Δ_5 transverse phonon branches. The treatment was performed in several steps. Preliminary fits revealed that both the TA and TO structure factors (figure 6.7a) and damping parameters (figure 6.7b) can be regarded as constant in the range ($0.05\,\text{r.l.u.} < q < 0.3\,\text{r.l.u}$). Moreover, these values do not change with temperature (within the errors of the fits). Further, we assumed constant background (independent of q within the Brillouin zone) and a locally linearized dispersion relation. Under these constraints, we obtained a more consistent set of fits giving the phonon energies, displayed in figure 6.6.

To appreciate the contribution of the transverse Δ_5 phonon modes to the whole scattering cross-section, figure 6.9a shows calculated intensity map of the lowest TA and TO modes from the model with the values obtained in the fit. figure 6.9b shows again the measured $\Gamma - X'$ dispersion.

These branches were investigated at practically the same temperature (783 K) also by Shirane *et al.* (see figure 1 of [Shirane 70a]). In both experiments, the TO soft phonon branch was not followed up to the BZ boundary. We probably encountered problems there simply because the structure factor for $q > 0.4$ r.l.u. rapidly decreases towards the BZ boundary (see figure 6.7a).

Data presented in this study differ from the earlier work in two aspects:

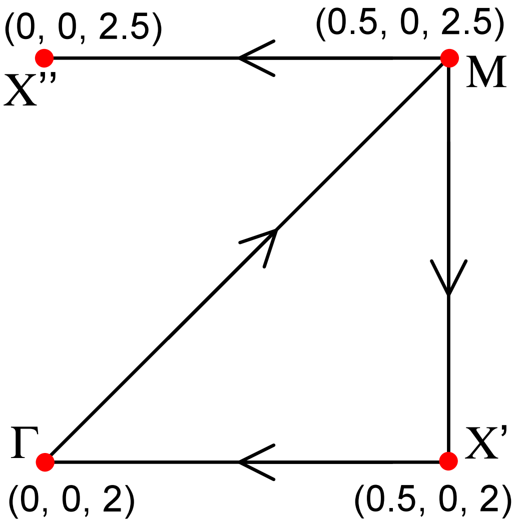

Figure 6.5: Schematic diagram of the directions in the [010] reciprocal plane, corresponding to those investigated in cubic $PbTiO_3$ and shown in Fig, 6.4.

- The TO dispersion reported in [Shirane 70a] is by about 2 meV lower than our data, while the TA dispersion is somewhat higher than in our experiment
- We did not observe the "dip" in the TA branch around $q = 0.1$ r.l.u., reported in [Shirane 70a].

These observations might be an indication of mode coupling [Harada 71]. However, the differences can be also related to a different sample used in our study (the samples can have, e.g., different T_C), or some unwanted resolution effects. Similar systematic shifts were spotted also at room temperature, and discussed in section 6.2.1.

The symmetry labels, indicating irreducible representations of measured phonon modes shown in figure 6.6, can be assigned by comparison with ab-initio data [Ghosez 99]. More quantitative comparison for these low-frequency branches is not possible since calculations were done at zero temperature, where the soft branch is unstable. Nevertheless, from the initial slopes of the acoustic branches we can estimate the high-frequency elastic constants: $C_{11} = 23 \cdot 10^{10}$ Pa, $C_{12} = 14 \cdot 10^{10}$ Pa, $C_{44} = 8 \cdot 10^{10}$ Pa (assuming the material density $\rho = 8000\,\mathrm{kg/m^3}$). We are not aware of a detailed Brillouin scattering experiment in the cubic phase, but these values are in good agreement with the C_{11} and C_{44} values from Brillouin experiments [Li 96].

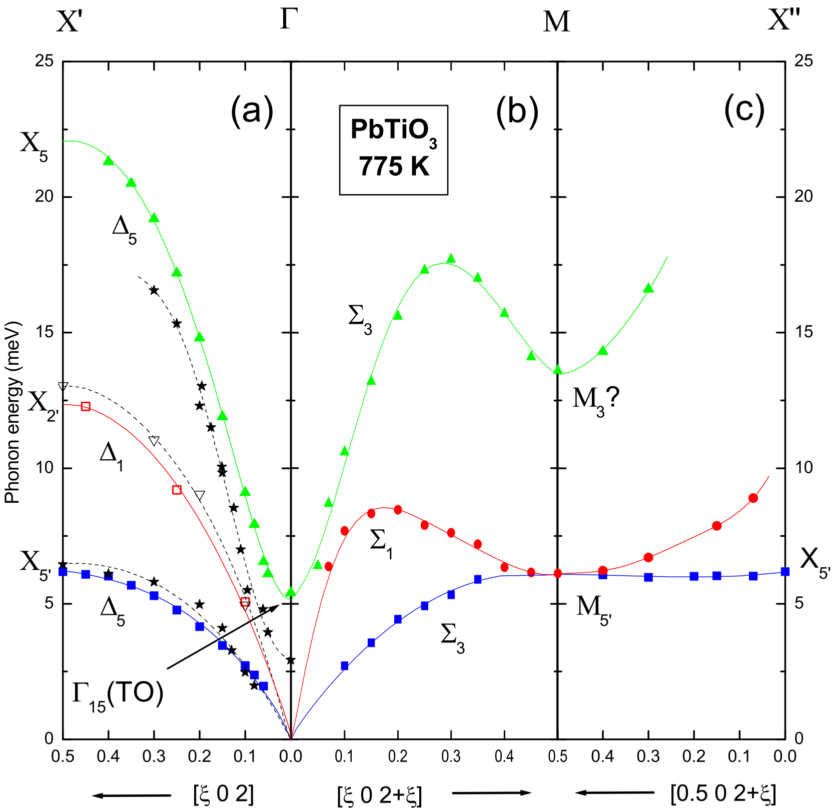

Figure 6.6: Low-frequency phonon dispersion curves in $PbTiO_3$ at 775 K along several high-symmetry cubic directions. Full symbols stand for the transverse modes from this study. Open squares: longitudinal acoustic branch, stars and open triangles: neutron scattering data from [Shirane 70a]. Dashed and solid lines are guides for the eyes.

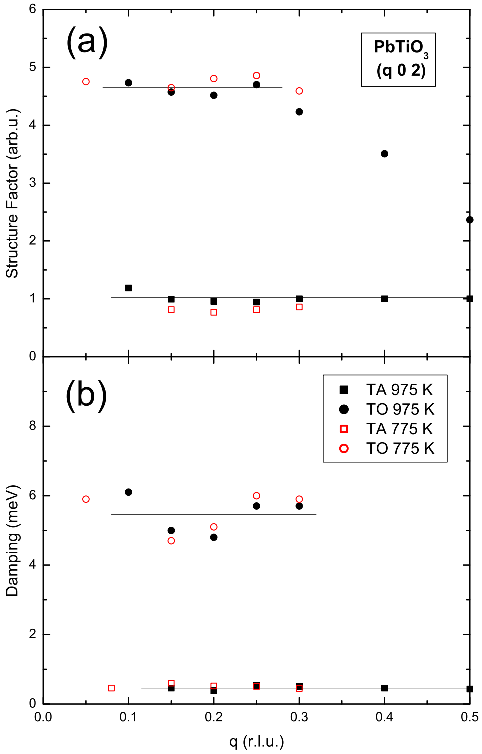

Figure 6.7: Fit parameters of the TA and TO phonon modes in the [ξ00] direction at 975 K (full symbols) and 775 K (empty symbols).

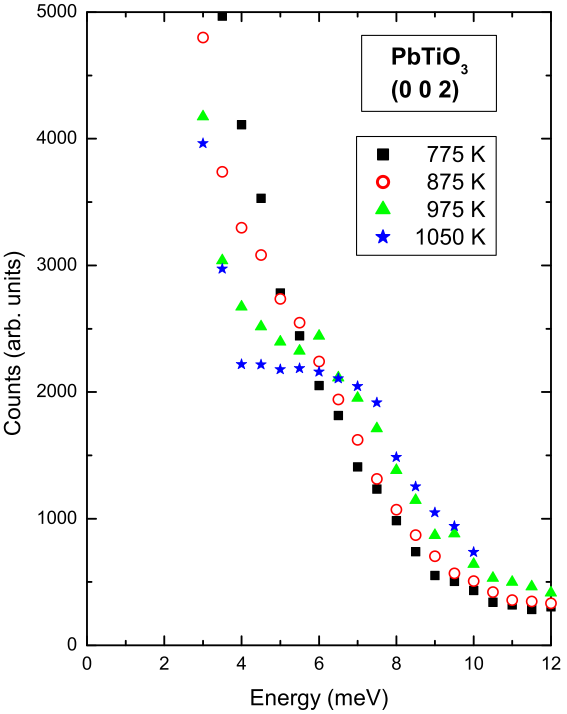

Figure 6.8: Temperature dependence of the Γ_{15}(TO) soft mode spectrum in the cubic phase.

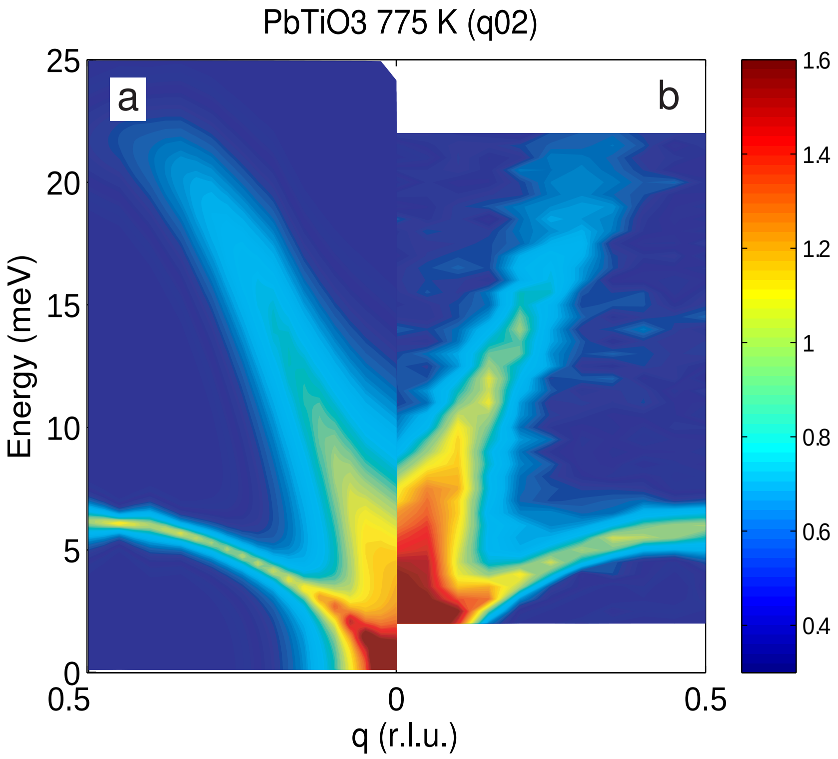

Figure 6.9: a: Intensity map calculated from the model described in the text (see equation 6.1 and thereafter); b: Measured $\Gamma - X'$ dispersion from figure 6.4.

This gives unusually high value of the cubic anisotropy parameter

$$A = \frac{2C_{44}}{C_{11} - C_{12}} \doteq 1.8 \ . \tag{6.2}$$

It is highly interesting [Cao 91] to try to evaluate also the anisotropy of the low-q dispersion of the soft phonon branch. Using the notation of [Harada 71], the dispersion of the TO soft branch can be approximated as

$$\begin{aligned} \hbar^2\omega^2_{[100]} &= \hbar^2\omega_0^2 + \Lambda(100)q^2 & (6.3)\\ \hbar^2\omega^2_{[110]} &= \hbar^2\omega_0^2 + \Lambda(110)q^2 \ . & (6.4) \end{aligned}$$

Using the 775 K data with q below 0.3 r.l.u., we have estimated that the values of gradient coefficients are about $\Lambda(100) = 1900$ (meVÅ)^2, $\Lambda(110) = 1100$ (meVÅ)^2 and $\omega_0 = 5.5 \pm 1$ meV. Here, on the contrary, the anisotropy is much lower than in $BaTiO_3$ [Harada 71].

6.2.3 Temperature behaviour of the soft mode

As the SM is not Raman active in the parent centro-symmetric phase, experimental data on the SM behaviour in the cubic phase are rather scarce. The lowest frequency is obviously expected right at the phase transition. Burns and Scott [Burns 73] deduced from the Raman spectra in the tetragonal phase that the SM in the $PbTiO_3$ single crystal softens down to about 50 cm^{-1} (6.2 meV). Fedorov *et al.* [Fedorov 95] designated from infrared measurements the SM softening in the *thin film* down to 33 cm^{-1} (4.1 meV) at 825 K. Inelastic neutron scattering study by Shirane *et al.* [Shirane 70a] reported that the SM in the single crystal softens down to 3 meV (24.2 cm^{-1}) at 785 K, which is significantly lower than our 775 K estimate $\omega_0(775\,K) = 5.5$ meV (44.4 cm^{-1}) mentioned above.

To elucidate these discrepancies, we have tried to follow the SM frequency as a function of temperature. The Γ-point spectra of the SM measured in the (002) BZ at various temperatures in the cubic phase are shown in figure 6.8. Clearly, the SM response at temperatures close to T_c merges with the tails of elastic scattering and thermal diffuse scattering from acoustic phonons, and there is probably also a noticeable contribution from a central peak [Fontana 91]. To determine the SM frequencies, we have therefore tried several fitting models, combining the following constraints:

- with or without additional Lorentzian peak describing the “central peak”

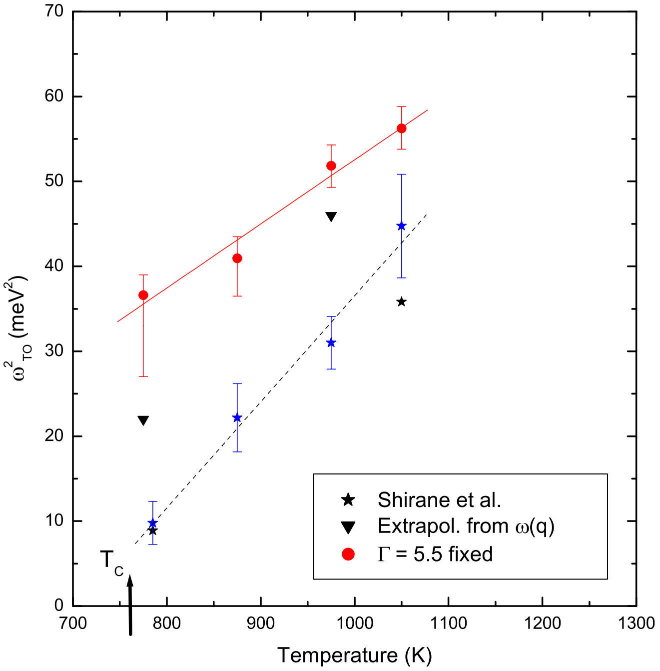

Figure 6.10: Soft mode energy as a function of temperature. Full circles: fits of the SM spectra by a single DHO response with damping fixed at 5.5 meV. The error bars represent the spread of the values from other fits, as described in the text. Stars, dashed line and corresponding error bars are data taken from figure 3 of [Shirane 70a]. The disagreement is discussed in the text.

- with free or constant inelastic structure factor of the SM (see figure 6.7a)
- with the damping constant either proportional to temperature, or kept at $\Gamma = 5.5$ meV, or left as free parameter (see figure 6.7b).

The spread of the values obtained from different models serves as a measure of the accuracy of the SM energy designation, and is represented by error bars in figure 6.10. However, we were not able to get reasonable fit with the frequencies reported in [Shirane 70a], for example 775 K data could not be adjusted with $\omega_0(775\,\mathrm{K}) = 3\,\mathrm{meV}$.

For this reason, we tried also an alternative method, used also in [Shirane 70a], which consists in extrapolation of the SM frequency from the spectra taken at q points in the vicinity of the Γ point. We tried to use this extrapolation method assuming the usual quadratic law for the phonon frequencies squared (see equation 6.3). However, in the investigated q-range the ω^2 vs. q^2 dependence was not linear, and it was obvious that the extrapolated en-

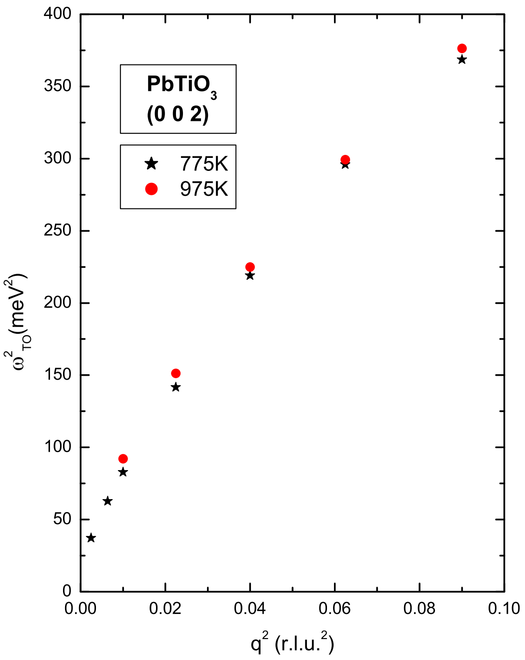

Figure 6.11: Square-square dependence of the lower-q part of the SM dispersion. Note that the dependence is not linear even for $q^2 \leq 0.04$, which makes the extrapolation to the BZ centre difficult.

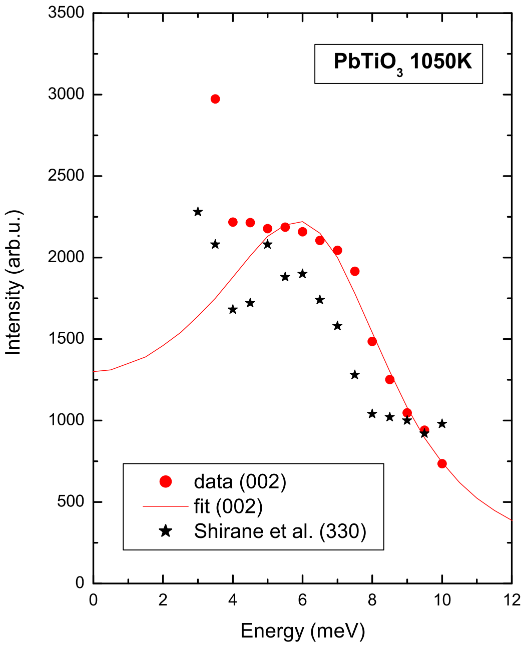

Figure 6.12: Comparison of the SM spectrum at 1050 K, as measured by Shirane *et al.* [Shirane 70a] (stars) and us (circles together with the DHO fit represented by solid line).

ergy depended on the q-range considered (see figure 6.11). In any case, this method gives a somewhat lower value of $\omega_0(TO)$: 6.8 meV at 975 K, and 4.7 meV at 775 K.

It is worth noting that, due to considerable damping, the maximum of DHO response fitted to our soft mode data is typically about $1-2$ meV below the DHO frequency. Therefore, the peak position itself would lead to temperature dependence much closer to the data of [Shirane 70a]. For example, our data at 1050 K were fitted to DHO response with oscillator frequency (7.5 ± 0.3) meV and damping (5.5 ± 0.3) meV (see figure 6.12). Interestingly, the peak position corresponds also well to the data of [Shirane 70a] taken at the same temperature (see figure 6.12).

Our temperature dependence of the soft-mode frequency extrapolates to zero well below $T_0 = 722$ K, determined from static dielectric measurements of [Remeika 70]. Therefore, an additional polar excitation (central peak) below the soft mode frequency is required for the fulfilment of the Lyddane-Sachs-Teller relation, applied to the dielectric constant from [Remeika 70], in agreement with conclusions of [Fontana 91]. However, it was not possible to determine the central peak parameters from our fits. Precise INS study of Γ-point soft modes in ferroelectrics is a difficult task, and confirmation of the central mode hypothesis will require more detailed investigation[2].

6.3 $PbTiO_3$ at high pressure

Pressure dependence of the properties of $PbTiO_3$ single crystals, powders and ceramics have been intensively studied by Raman spectroscopy [Cerdeira 75, Sanjurjo 83, Kornev 05], X-ray diffraction [Nelmes 86, Ramirez 91, Sani 02], XANES [Itie 06, Jaouen 07] and also by first-principles calculations [Tinte 03, Wu 05, Kornev 05, Kornev 07], molecular dynamics simulations [Costa 05], by the phenomenological Landau-Ginzburg-Devonshire theory [Budimir 05] etc.

Motivations for our high-pressure studies of $PbTiO_3$ arose from recent *ab-initio* studies:

1. Wu&Cohen [Wu 05] performed zero temperature calculations based on density functional theory (DFT) within the local density approximation (LDA). They reported a sequence of phase transitions in the pressure phase diagram: from the ambient tetragonal through monoclinic and rhombohedral to cubic. The most interesting part of the proposed diagram is the monoclinic part – the morphotropic phase boundary (MPB). If $PbTiO_3$ possessed the MPB phase in a certain range of pressures (which was to be confirmed experimentally), it would mean, among all, an advance in understanding the corresponding relaxor properties.

2. Another *ab-initio* study [Kornev 05], supported by Raman experiments [Kornev 05] reported, after reaching the cubic phase ($c/a \rightarrow 1$) at a fairly high pressure (30 GPa), a re-entrant ferroelectric phase, which is supposed to be of an electronic origin.

In this part, we present our recent results from inelastic X-ray (IXS) and neutron (INS) scattering studies. We show that the predictions of [Wu 05] do not agree with our observations, i.e. that the MPB is not likely to appear in $PbTiO_3$. On the other hand, we believe that the scenario stated in [Kornev 05] is more realistic (even if our results are not connected to their

---

[2] An experiment dealing with this subject is planned for the second half of 2008 at the ILL.

observations), mainly because it has already been confirmed experimentally. However, for the experimental reasons stated below, we could not decide about the behaviour of the TO soft mode above 10 GPa.

6.3.1 Inelastic X-ray scattering

In order to confirm or disprove the predictions of Wu&Cohen [Wu 05], we searched for instabilities in the pressure dependence of the lowest TA phonon mode at the BZ boundary; for this purpose, inelastic X-ray scattering (IXS) provides a valuable tool.

IXS is closely related to INS; the fundamental difference lies in the type of interaction, i.e. between photons and electrons in the case of IXS, with a strength comparable to the neutron-nucleus scattering cross-section b. Due to photoelectric absorption, increasing with atomic number Z faster than the cross-section, atoms with high Z are not suitable for IXS experiments [Hercules].

IXS is particularly suited for the studies of samples only available in very small quantities ($\ll 1\,\mathrm{mm}^3$), or for high-pressure studies. If we take into account the ratio between the photon energy (≈20 keV) and the energy transfer (e.g. 20 meV), it is clear that the IXS experiment with such precision (10^{-7} or better) is realizable only thanks to high brilliance of the photon beam.

Our IXS experiment was done at the ID28 inelastic X-ray beamline [ID28] on the ESRF synchrotron, Grenoble, France. The sample (diameter $20\,\mu$m, height $5\,\mu$m) was placed in a diamond anvil cell which in principle can produce pressures up to 60 GPa; in our case, however, it broke when going to 40 GPa. Yet the range of pressures reached was sufficient for our conclusions. We used the Si(11,11,11) reflection on monochromator, which corresponds to energy resolution ≈1.5 meV. The focal spot size of the beam at the sample was $25\,\mu m$ horizontally and $60\,\mu m$ vertically.

An inelastic X-ray scattering beamline allows to reach practically any point in a Brillouin zone, in the case of pressure studies though limited by the windows of the pressure cell; his is mainly thanks to the fact that the energy of the photons incident on the sample is selected by changing the temperature of the monochromator crystal. In practice, however, the Lorentzian-like energy resolution function does not allow to study phenomena close to the BZ centre or to zero energy transfer, or generally near any scattering stronger than the desired inelastic signal (elastic scattering, diffuse scattering etc.) This fact was not in contradiction with the idea of investigating the BZ boundaries. The only remaining question was the choice of particular BZ boundary points,

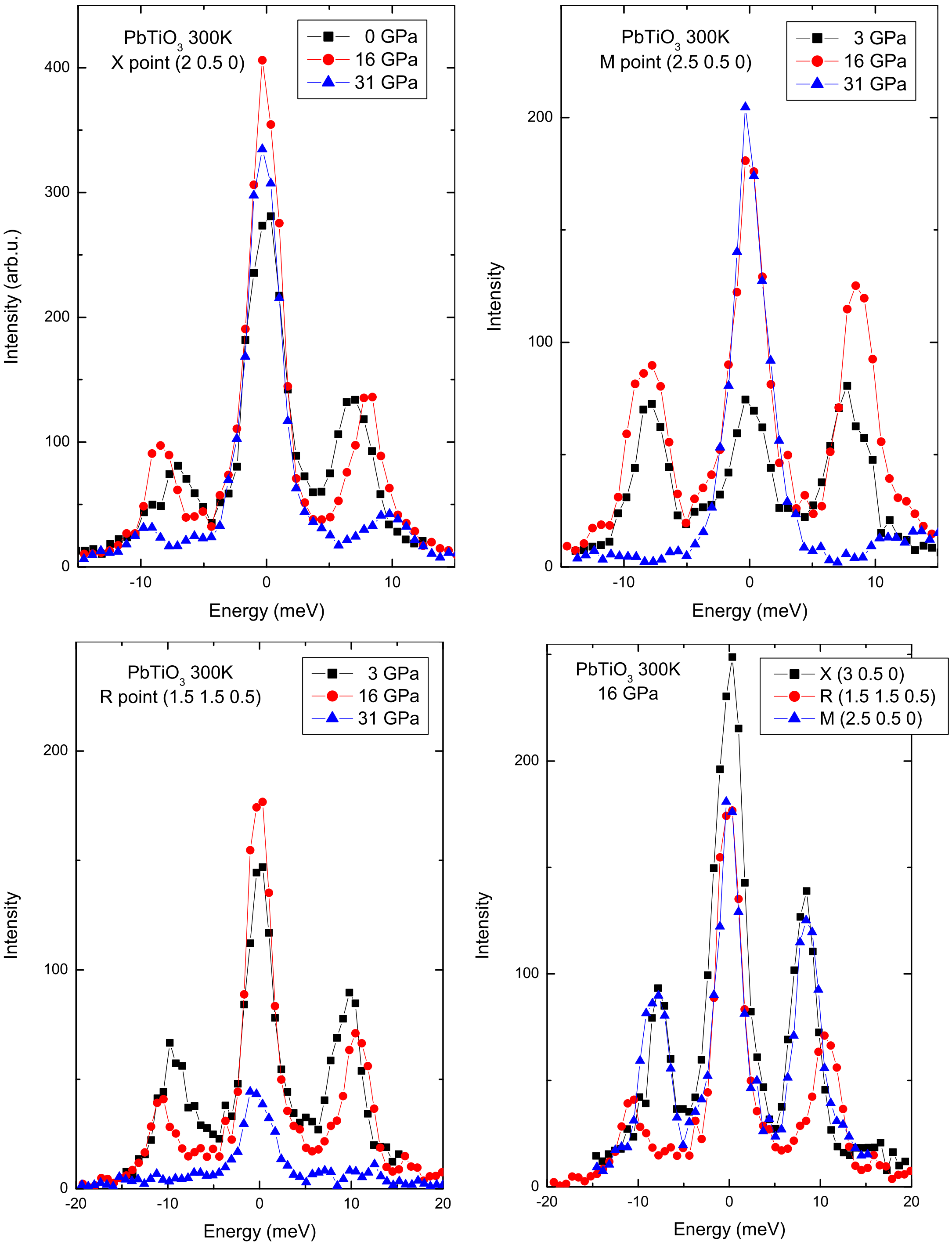

Figure 6.13: Representative IXS spectra of PbTiO$_3$ measured at BZ boundary points, as a dependence of pressure. The spectrum consists of the elastic peak and the TA phonon mode, symmetrically located at both positive and negative energy transfers.

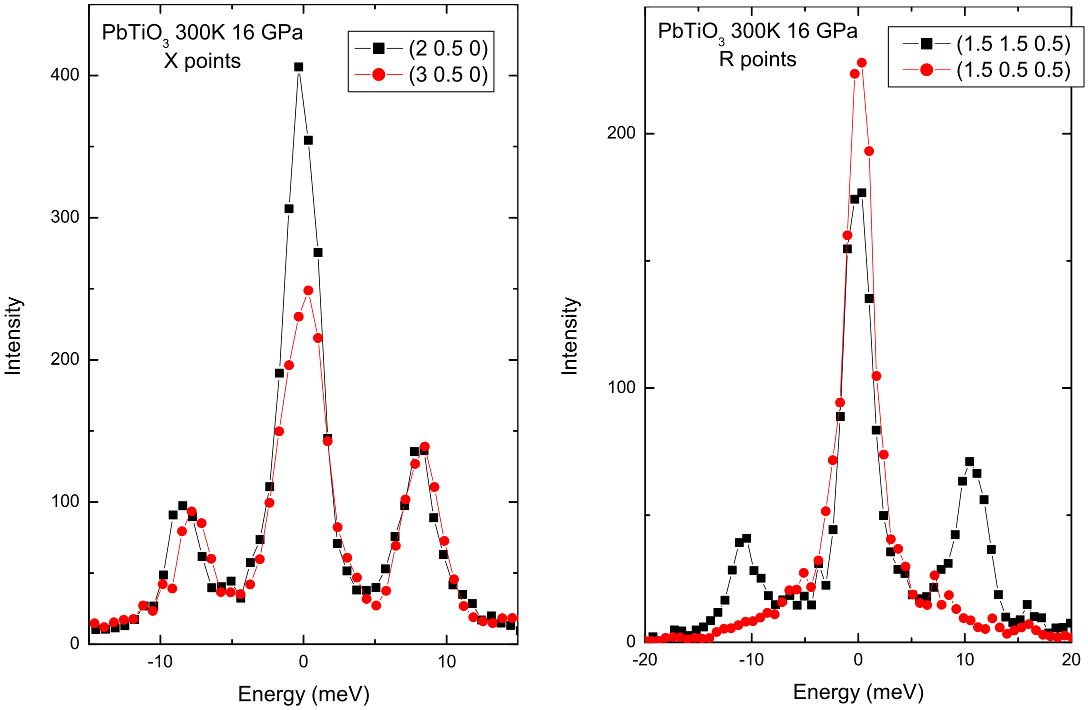

Figure 6.14: Comparison of IXS spectra of PbTiO$_3$ at 16 GPa at two different X- and R-points, showing the difference in the TA structure factors.

corresponding to BZs with different structure factors[3] (see figure 6.14).

Typical IXS spectra at the zone boundary points(X, M, R) at different pressures are shown in figure 6.13. It can be clearly seen that in each spectrum, the elastic signal is well separated from the TA phonon. From figures 6.14 we can estimate the change of the signal at different zone boundary points, due to different structure factors depending on the Brillouin zone chosen. The origin of the pressure dependence of the elastic line intensity is not know to us, as well as its variation among the BZ boundary points. The possible factors are the orientation of the sample in the pressure cell, the effective sample volume irradiated by the X-ray beam, and the fact that there are more different contributions to the elastic intensity (Bragg scattering, diffuse scattering from the sample, scattering from the pressure cell).

The spectra were fitted by simple Lorentzians, in order to trace the change of the TA peak positions with increasing pressure. As a result, the pressure dependence of the TA frequencies in all BZ boundary points studied are summarized in figure 6.18. Obviously, when disregarding the shallow minimum at ≈2 GPa, TA frequencies in all investigated BZ boundary points systematically harden with pressure, thus not confirming the proposed TA instabilities [Wu 05].

6.3.2 Inelastic neutron scattering

For high-pressure measurements, a cylinder-shaped crystal of about 2 mm diameter was mounted into a Paris-Edinburgh pressure cell [Klotz 00], in principle able to apply hydrostatic pressures up to ≈12 GPa. The experiment was carried out on the 1T three-axis spectrometer at LBB Saclay, under the same conditions as described in the beginning of section 6.3.2.

Another feature, which would accompany the possible transition to the monoclinic phase, is the softening of the respective elastic constant C_{44} [Wu 05]. This could not be checked by IXS, because by the means of inelastic scattering, the elastic constants have to be determined by measurements at low energy transfers q, as near to the BZ centre as possible. On the other hand, inelastic neutron scattering (INS), with its Gaussian-like resolution, is much more suitable to approach these areas.

The values of C_{44} obtained so far by different authors and techniques are summarized in table 6.2.

In order to calibrate the pressure cell, we compared at each pressure the refined lattice parameters a, c (figure 6.15b) with their tabulated dependence

---

[3] Note: the appellations of the zone boundary points (R, M, X) were, for simplicity, kept from the cubic symmetry.

source	[Kempa 06a]	[Tomeno 06]		[Li 96]	[Wu 05]	[Freire 88]
method	INS	INS		Brillouin	*ab-initio*	rigid-ion m.
T	775 K	295 K		295 K	0 K	300 K
type	$C_{44}(C)$	$C^{E}_{44}(T)$	$C^{P}_{44}(T)$	$C^{E}_{44}(T)$	$C_{44}(C)$	$C_{44}(T)$
(10^{10} Pa)	8	7.2	8.0	6.5	6.0	8.0

Table 6.2: Elastic constant C_{44} at ambient pressure from various experiments and calculations.

known from powder diffraction measurements [Janolin 07] (figure 6.15a). The precision of such calibration is governed mainly by the precision of the a, c determination (less than 0.3%, limited by the resolution of the spectrometer and increasing with pressure), and by the relaxation of the pressure itself with time (less than 5% of total decrease of pressure). The latter factor was eliminated by performing the calibration several times during each pressure. The resulting calibration curve is displayed in figure 6.15c.

From available data of pressure dependence of lattice parameters a, c we have chosen diffraction measurements on powder [Janolin 07]. Apart from the data obtained on the ceramic sample [Ikeda 75], other samples gave practically same results (figure 6.15a).

With the sample in the pressure cell, one is in principle limited in the range of scattering angles, and consequently in the accessible areas of the reciprocal plane. Thanks to prior alignments, this restriction showed not to be critical, and we could reach all the **Q**-points important for our study.

With increasing pressure, the signal from the sample decreases, mainly due to closing of the clamping jaws of the cell. Moreover we could not reach pressures higher than 5 GPa because the sample started to turn around a horizontal axis at each increase of pressure. Fortunately this axis was (100), perpendicular to the direction $q \parallel (001)$ of the dispersion. At 5 GPa, the tilt of the respective goniometer was 8 degrees, which did not allow to accumulate any useful intensity. Thus for the last point (5 GPa) we have set the goniometer to zero (vertical position). Assuming isotropic dispersions in the [100] plane, we used Christoffel equations [Every 79], and estimated the error of the determination of the TA frequency from scans with such tilt to 2%.

Typical INS energy spectra are shown in figure 6.16a. At low pressures, the TA mode appeared as a sharp peak at about 5 meV; above 1 GPa the crystal twinned (two grains, mutually rotated, were created by pressure), and thus another peak at ≈3 meV appeared. In addition, the "original" mode started to broaden as expected, but still it remained well defined. We

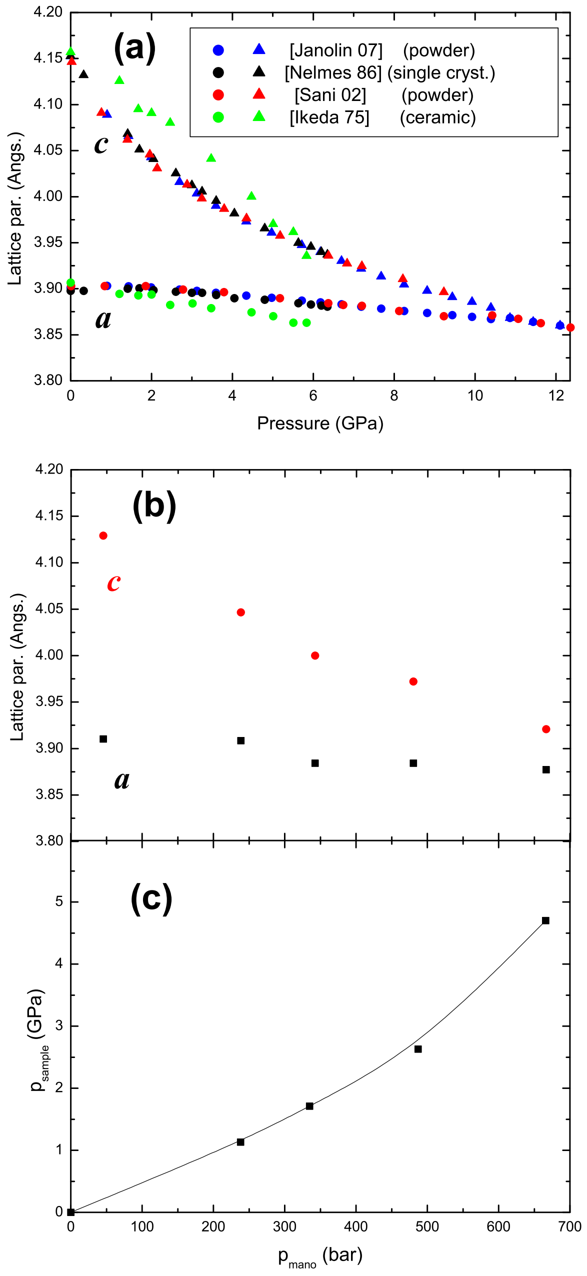

Figure 6.15: (a): Pressure dependence of lattice parameters a, c of $\mathrm{PbTiO_3}$ on different samples (from literature – the citations are given in the figure). (b): Dependence of the lattice parameters in our INS study on the manometer pressure. (c): Calibration of the Paris-Edinburgh pressure cell, i.e. the dependence of the pressure applied to the sample on the pressure actually set on the manometer. The line is a guide for the eye.

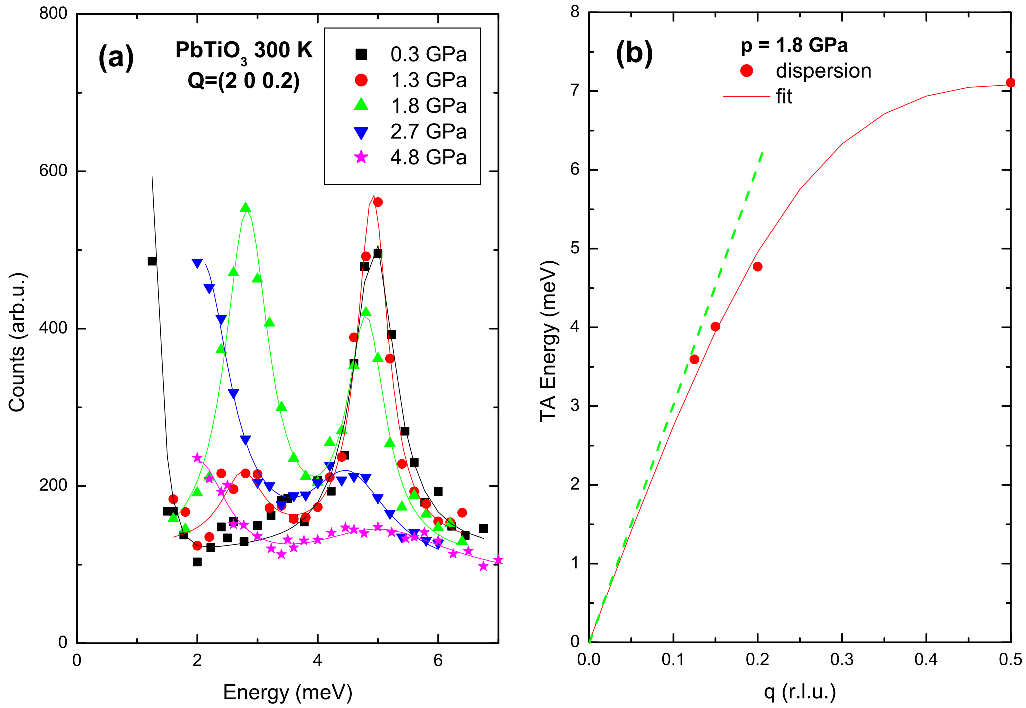

Figure 6.16: (a): INS spectra for $q = 0.2$ r.l.u. With increasing pressure, the TA mode at ≈5 meV started to split due to twinning. (b): To the determination of the C_{44} pressure dependence; full line: fit of the dispersion, dashed line: limiting slope of the low-frequency part of the dispersion.

cannot, however, exclude the possibility that the crystal twinned again at the highest pressure.

The elastic constant C_{44} was determined from a well-known expression

$$C_{44} = \rho v^2 \tag{6.5}$$

where ρ is the material density, and v is the sound velocity, which can be calculated as the slope $v = d\omega/dq$ of the linear (low-q) part of the dispersion of the corresponding [100] TA mode (see figure 6.16b). The density ρ of $PbTiO_3$ has been corrected for pressure, through the refined lattice parameters a, c.

The value of C_{44} (through the sound velocity v) is very sensitive to small changes of the TA dispersion. Therefore, the slopes of the dispersion were determined consistently in the same way for all pressures[4]. Thus the relative

---

[4] The best method for determining the slope of the low-frequency part of the TA dispersion showed to be fitting the whole dispersion at each pressure to the formula $\omega_{TA} = A\sqrt{\sin^2(\pi q) + B\sin^2(2\pi q)}$. Then the desired slope (and consequently, after the conversion of units, the sound velocity v) is $A\pi\sqrt{1+4B}$.

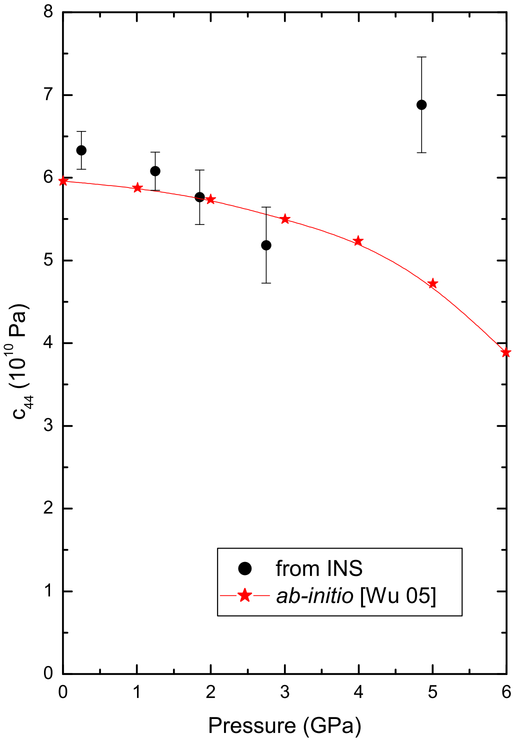

Figure 6.17: Pressure dependence of the elastic constant C_{44}. Full circles: determined from our INS measurement. Stars: calculated by *ab-initio* [Wu 05] at 0 K; The line is a guide for the eye.

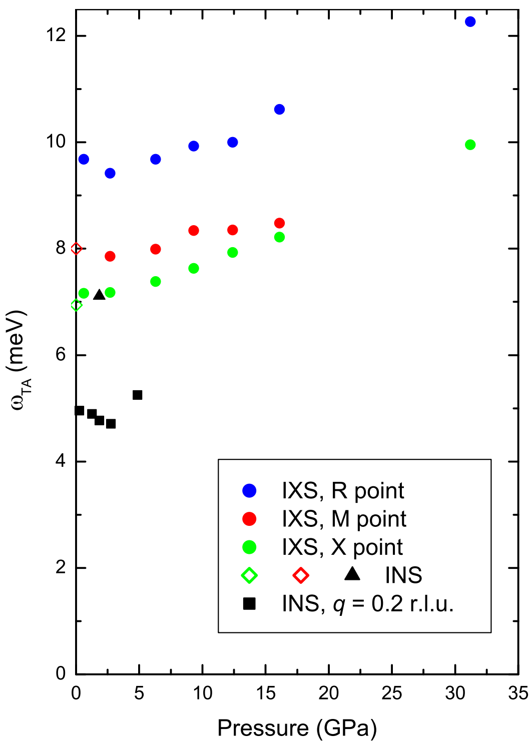

Figure 6.18: Pressure dependence of the TA frequencies in different BZ boundary points from our IXS and INS experiments. For comparison, also the dispersion at (2 0 0.2) is included (full squares and stars).

pressure dependence should be free of errors concerning the determination of the individual slopes at each pressure, bearing in mind the possible high uncertainty in the absolute value of C_{44}.

As a result, the pressure dependence of C_{44} is displayed in figure 6.17, together with the predicted C_{44} at 0 K of Wu&Cohen [Wu 05].

Wu&Cohen [Wu 05] predicted complete softening of C_{44} at ≈9 GPa. Because of technical problems mentioned above, we could not reach pressures above 5 GPa. We have thus confirmed the softening of C_{44} up to ≈3 GPa. Then the TA frequency appears to re-harden again. Although we cannot be completely sure about the last point at ≈5 GPa (as explained above), it may indicate an anomaly around 4 GPa which has to be confirmed by further experiments.

For comparison, the results of the INS study are also included in fig-

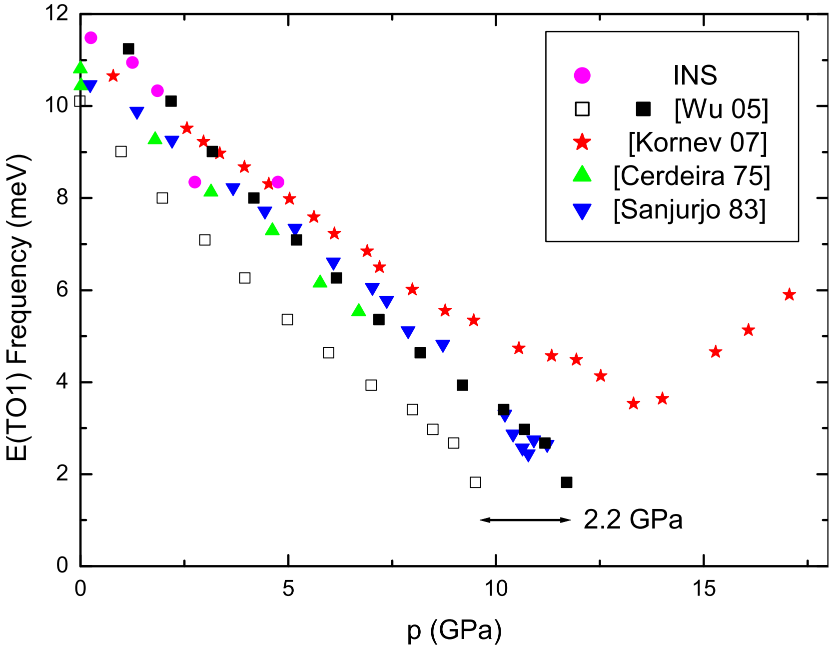

Figure 6.19: Pressure dependence of the E(TO1) soft mode frequency.

ure 6.18, showing their good agreement with the IXS data.

At lower pressures, we also determined the dispersion of the E(TO1) soft mode (figure 6.19); our results are in good agreement with Raman data [Cerdeira 75, Sanjurjo 83, Kornev 07] as well as with first-principles calculations [Wu 05]. Concerning the latter source, we shifted the data by 2.2 GPa, according to the remark about the correction to the volume of the unit cell [Wu 05].

Chapter 7

Summary

This thesis reports on lattice dynamics of perovskite relaxor ferroelectrics PMN and PZN–8%PT, and of perovskite ferroelectric $PbTiO_3$, mainly by inelastic neutron scattering and far-IR spectroscopy. The investigated materials have been established as model examples in their categories (PMN as a "pure" relaxor, PZN–8%PT as a relaxor near the morphotropic phase boundary, and $PbTiO_3$ as a model displacive ferroelectric). Despite this effort and great progress, many of their properties are not still fully understood.
The experimental part of the thesis is divided into two parts.

In the first part, devoted to relaxors, we have revisited the question of the origin of the unexpected shape of the apparent soft mode dispersion curve obtained by tracing the scattered intensity ridge in INS measurements of lead-based relaxors (the so-called waterfall effect). We have demonstrated that

1. the waterfall effect is not an artefact of instrumental resolution, since it persists in the (20q) experiments repeated on PZN-8PT and PMN with significantly improved resolution conditions;
2. the absence of the waterfall effect in (22q) measurements of [Gvasaliya 05] cannot be explained by the AOMI model [Hlinka 03a];
3. the waterfall effect appears in the (20q) $S(q, \omega)$ map reconstructed from the PMN experiment of [Wakimoto 02b], but not in the (22q) $S(q, \omega)$ map reconstructed from the PMN experiment of [Gvasaliya 05] (it implies that neither the fitting nor the model choice are responsible for the difference);
4. the raw (20q) soft-mode spectra recorded with a number of various PMN samples are similar, while they significantly differ from (22q) raw spectra of [Gvasaliya 05].

On the other hand, the frequency dispersion, damping dispersion and the temperature independence of the presumed TO branch in the no-waterfall experiment of [Gvasaliya 05] strongly suggest that this branch is actually an LA branch. While the reason for the appearance of the LA mode scattering remains to be clarified, the basic contradiction can be naturally explained in this way: the waterfall is not observed simply because it is hidden by the LA mode scattering.

Finally, we admit that the AOMI model [Hlinka 03a] is not general enough to describe the soft mode dynamics in detail. At the same time, we are not aware of any solid argument disqualifying its basic idea: it provides the most simple and natural explanation for the origin of the waterfall wave vector including its dependence on the BZ selected in the INS experiment. At present, the possibility of a peculiar q-dependence of the soft mode damping cannot be excluded. Ideally, the wave-vector dependence of all coupled DHO parameters should be derived from the experiment directly. This is, however, a very nontrivial task as it is not even obvious how many branches should be included in the fit. It is possible that a considerable progress in understanding can arise when systematic fitting of phonon dispersions in 2D or 3D areas of the reciprocal space is done.

The second part is devoted to $PbTiO_3$. At ambient pressure, we investigated long-wavelength lattice dynamics of $PbTiO_3$ in the both tetragonal and cubic phase. We showed that our neutron data at room temperature for phonon modes are perfectly consistent with the results of recent Raman and Brillouin scattering studies. Also, they are in good agreement with the frequencies of zone boundary modes predicted by *ab-initio* calculations. On top of that, our results reveal a remarkable tetragonal anisotropy in the ferroelectric phase of $PbTiO_3$. This more complete picture of low-energy phonon dispersion curves in $PbTiO_3$ will provide a reference for comparison with other perovskites, such as lead-based relaxor ferroelectrics, exhibiting Last-type soft modes.

The lattice dynamics of cubic $PbTiO_3$ was investigated along the $[\xi 00]$ and $[\xi\xi 0]$ directions. These measurements allowed to estimate dispersion parameters defining the anisotropy of the acoustic and soft mode branches. The obtained dispersions are again in good agreement with other studies. Attention was paid also to the softening of the TO soft mode with temperature.

The soft mode is not overdamped in $PbTiO_3$, but determination of its frequency from our spectra was difficult. Our analysis gives the SM energy (5.5 ± 1) meV at $775\,\mathrm{K}$ ($T_\mathrm{c} + 15\,\mathrm{K}$), and its temperature dependence indicates additional low-frequency relaxation (central peak). More detailed study is needed to clarify this issue.

In the pressure studies, we showed that our new IXS and INS data do not support the *ab-initio* calculations of [Wu 05], particularly:

- Lowest zone-boundary (X,M,R) modes do not soften at pressures up to 31 GPa.
- Complete softening of C_{44} was not observed; on the other hand, our results indicate possible anomalous pressure dependence at about 4 GPa (figure 6.17), which remains to be explained.

We hope that the experimental results of this thesis will be useful for beter insight to lattice dynamics of the inversigated materials.

Bibliography

[Altmann 65] L.S. Altmann and A.P. Cracknell, *Rev. Mod. Phys.* **37**, 19 (1965).

[Arai 96] M. Arai, M. Fujita, M. Motokawa, J. Akimitsu and S.M. Bennington, *Phys. Rev. Lett.* **77**, 3649 (1996).

[Blinc 06] R. Blinc, V.V. Laguta, B. Zalar and J. Banys, *J. Mater. Sci.* **41**, 27 (2006).

[Bouckaert 36] L.P. Bouckaert, R. Smoluchowski and E. Wigner, *Phys. Rev.* **50**, 58 (1936).

[Bovtun 04] V. Bovtun, S. Kamba, A. Pashkin, M. Savinov, P. Samoukhina and J. Petzelt, *Ferroelectrics* **298**, 23 (2004).

[Bovtun 06] V. Bovtun, S. Veljko, S. Kamba, J. Petzelt, S. Vakhrushev, Y. Yakymenko, K. Brinkman and N. Setter, *J. Eur. Ceram. Soc.* **26**, 2867 (2006).

[Brockhouse 62] B.N. Brockhouse, T. Arase, G. Caglioti, K.R. Rao and A.D.B. Woods, *Phys. Rev.* **128**, 1099 (1962).

[Budimir 05] M. Budimir, D. Damjanovic and N. Setter, *Phys. Rev. B* **72**, 064107 (2005).

[Burns 73] G. Burns and B.A. Scott, *Phys. Rev. B* **7**, 3088 (1973).

[Burns 76a] G. Burns, *Phys. Rev. Lett.* **37**, 229 (1976).

[Burns 76b] G. Burns, *Phys. Rev. B* **13**, 215 (1976).

[Burns 83] G. Burns and F.H. Dacol, *Phys. Rev. B* **28**, 2527 (1983).

[Bussmann-Holder 04] A. Bussmann-Holder and A.R. Bishop, *J. Phys.: Condens. Matter* **16**, L313 (2004).

[Cao 91] W. Cao and L.E. Cross, *Phys. Rev.* **44**, 5 (1991).

[Cerdeira 75] F. Cerdeira, W.B. Holzapfel and D.Bäuerle, *Phys. Rev. B* **11**, 1188 (1975).

[Cho 01] S.M. Cho, H.M. Jang and T.-Y. Kim, *Phys. Rev. B* **64**, 014103 (2001).

[Colla 07] E.V. Colla, M.B. Weissmann, P.M. Gehring, G. Xu, H. Luo, P. Gemeiner and B. Dkhil, *Phys. Rev. B* **75**, 024103 (2007).

[Cooper 67] M.J. Cooper and R. Nathans, *Acta Cryst.* **23**, 357 (1967).

[Costa 05] S.C. Costa, P.S. Pizani, J.P. Rino and D.S. Borges, *J. Phys.: Condens. Matter* **17**, 5771 (2005).

[Dmowski 00] W. Dmowski, M.K. Akbas, P.K. Davies and T. Egami, *J. Phys. Chem. Solids* **61**, 229 (2000).

[Dorner 03] B. Dorner, A.S. Ivanov, S.B. Vakhrushev, S.G. Lushnikov, S.N. Gvasaliya, D. Strauch and K. Schmalzl, *Ferroelectrics* **282**, 9 (2003).

[Egami 03] T. Egami, E. Mamontov, W. Dmowski and S. Vakhrushev, *AIP Conf. Proc.* **677**,48 (2003).

[Eklund 77] P.C. Eklund, G. Dresselhaus, M.S. Dresselhaus and J.E. Fischer, *Phys. Rev. B* **16**, 3330 (1977).

[Every 79] A.G. Every, *Phys. Rev. Lett.* **42**, 1065 (1979).

[Fedorov 95] I. Fedorov, J. Petzelt, V. Železný, G.A. Komandin, A.A. Volkov, K. Brooks, Y. Huang and N. Setter, *J. Phys.: Condens. Matter* **7**, 4313 (1995).

[Fontana 91] M.D. Fontana, H. Idrissi, G.E. Kugel and K. Wojcik, *J. Phys.: Condens. Matter* **3**, 8695 (1991).

[Foster 93] C.M. Foster, Z. Li, M. Grimsditch, S.K. Chan and D.J. Lam, *Phys. Rev. B* **48**, 10160 1993.

[Freire 88] J.D. Freire and J.S. Katiyar, *Phys. Rev. B* **37**, 2074 (1988).

[Garcia 96] A. García and D. Vanderbilt, *Phys. Rev. B* **54**, 3817 (1997).

[Gehring 00a] P. M. Gehring, S.-E. Park and G. Shirane, *Phys. Rev. Lett.* **84**, 5216 (2000).

[Gehring 00b] P.M. Gehring, S.B. Vakhrushev and G. Shirane, *AIP Conf. Proc.* **535**, 314 (2000).

[Gehring 01a] P.M. Gehring, S.-E. Park and G. Shirane, *Phys. Rev. B* **63**, 224109 (2001).

[Gehring 01b] P.M. Gehring, S. Wakimoto, Z.-G. Ye and G. Shirane, *Phys. Rev. Lett.* **87**, 277601 (2001).

[Gehring 04a] P.M. Gehring, W. Chen, Z.-G. Ye, G. Shirane, *J. Phys.: Condens. Matter* **16**, 7113 (2004).

[Gehring 04b] P.M. Gehring, K. Ohwada and G. Shirane, *Phys. Rev. B* **70**, 014110 (2004).

[Ghosez 99] P. Ghosez, E. Cockayne, U.V. Waghmare and K.M. Rabe, *Phys. Rev. B* **60**, 836 (1999).

[Glinchuk 02] M.D. Glinchuk and E.A. Eliseev, *Appl. Phys. Lett.* **81**, 4808 (2002).

[Guttler 03] B. Guttler, B. Mihailova, R. Stosch, U. Bismayer and M. Gospodinov, *J. Mol. Str.* **661**, 469 (2003).

[Gvasaliya 03] S.N. Gvasaliya, D. Strauch, B. Dorner, S.G. Lushnikov and S.B. Vakhrushev, *Ferroelectrics* **282**, 21 (2003).

[Gvasaliya 04] S.N. Gvasaliya, S.G. Lushnikov and B. Roessli, *Phys. Rev. B* **69**, 092105 (2004).

[Gvasaliya 05] S.N. Gvasaliya, B. Roessli, R.A. Cowley, P. Hubert and S.G. Lushnikov, *J. Phys.: Condens. Matter* **17**, 4343 (2005).

[Gvasaliya 07] S.N. Gvasaliya, B. Roessli, R.A. Cowley, S. Kojima and S.G. Lushnikov, *J. Phys.: Condens. Matter* **19**, 016219 (2007).

[Harada 71] J. Harada, J.D. Axe and G. Shirane, *Phys. Rev. B* **4**, 155 (1971).

[Hehlen 07] B. Hehlen, G. Simon and J. Hlinka, *Phys. Rev. B* **75**, 052104 (2007).

[Hellwig 06]	H. Hellwig, A. Sehirlioglu, D.A. Payne and P. Han, *Phys. Rev. B* **73**, 094126 (2006).
[Hennion]	B. Hennion and P. Bourges, AFITV: Refinement program for triple axis spectrometer data at Laboratoire Leon Brillouin, CEA/Saclay, France.
[Hercules]	J. Baruchel, J.L. Hodeau *et al.* (editors), Neutron and synchrotron radiation for condensed matter studies, Vol. 1,2 (HERCULES proceedings) (Les Editions Physique & Springer Verlag, Paris & Berlin, 1993).
[Hlinka 03a]	J. Hlinka, S. Kamba, J. Petzelt, J. Kulda, C.A. Randall and S.J. Zhang, *Phys. Rev. Lett.* **91**, 107602 (2003).
[Hlinka 03b]	J. Hlinka, S. Kamba, J. Petzelt, J. Kulda, C.A. Randall and S.J. Zhang, *J. Phys.: Condens. Matter* **15**, 4249 (2003).
[Hlinka 06a]	J. Hlinka, M. Kempa, J. Kulda, P. Bourges, A. Kania and J. Petzelt, *Phys. Rev. B* **73**, 140101 (2006).
[Hlinka 06b]	J. Hlinka, J. Petzelt, S. Kamba, D. Noujni and T. Ostapchuk, *Phase Transitions* **79**, 163 (2006).
[Hlinka 06c]	J. Hlinka, T. Ostapchuk, D. Noujni, S. Kamba and J. Petzelt, *Phys. Rev. Lett.* **96**, 027601 (2006).
[ID28]	`http://www.esrf.eu/UsersAndScience/Experiments/HRRS/ID28`
[Ikeda 75]	T. Ikeda, *Solid State Commun.* **16**, 103 (1975).
[Itie 06]	J.P. Itié, B. Couzinet, A.C. Dhaussy, A.M. Flank, N. Jaouen, P. Lagarde and A. Polian, *High Pressure Res.* **26**, 325 (2006).
[Ivanov 84]	A.S. Ivanov, N.L. Mitrofanov, A.Yu. Rumiantsev, V.I. Bobrovskii, B.N. Goshchitskii, A.A. Evtukh, I.L. Zhdakhin, V.P. Koliadin and A.V. Mirmel'stein, Preprint KIAE-3913/9, I.V Kurchatov Institute of Atomic Energy, Moscow 1984 (in Russian).
[Ivanov 05]	M.A. Ivanov, M. Kozlowski, T. Piesiewicz, V.A. Stephanovich, A. Weron and A. Wymyslowski, *Phys. Solid State* **47**, 1928 (2005).

[Iwata 00] M. Iwata, H. Hoshino, H. Orihara, H. Ohwa, N. Yasuda and Y. Ishibashi, *Jpn. J. Appl. Phys.* **39**, 5691 (2000).

[Janolin 07] P.-E. Janolin, PhD thesis, École Centrale Paris (2006).

[Jaouen 07] N. Jaouen, A.C. Dhaussy, J.P. Itié, A. Rogalev, S. Marinel and Y. Joly, *Phys. Rev. B* **75**, 224115 (2007).

[Kalinichev 97] A.G. Kalinichev, J.D. Bass, B.N. Sun and D.A. Payne, *J. Mater. Res.* **12**, 2623 1997.

[Kamba 03] S. Kamba, E. Buixaderas, J. Petzelt, J. Fousek, J. Nosek and P. Bridenbaugh, *J. Appl. Phys.* **93**, 933 (2003).

[Kamba 05a] S. Kamba, M. Kempa, V. Bovtun, J. Petzelt, K. Brinkman and N. Setter, *J. Phys.: Condens. Matter* **17**, 3965 (2005).

[Kamba 05b] S. Kamba, M. Berta, M. Kempa, J. Hlinka, J. Petzelt, K. Brinkman and N. Setter, *J. Appl. Phys.* **98**, 074103 (2005).

[Kamba 05c] S. Kamba, M. Kempa, M. Berta, J. Petzelt, K. Brinkman and N. Setter, *J. Phys. IV France* **128**, 121 (2005).

[Kania 06] A. Kania, A. Slodczyk and Z. Ujma, *J. Cryst. Growth* **289**, 134 (2006).

[Kempa 06a] M. Kempa, J. Hlinka, J. Kulda, P. Bourges, A. Kania and J. Petzelt, *Phase Trans.* **79**, 351 (2006).

[Kempa 06b] M. Kempa, B. Janousova, J. Saroun, P. Flores, M. Boehm, F. Demmel and J. Kulda, *Physica B* **385-386**, 1080 (2006).

[Kiat 02] J.M. Kiat, Y. Uesu, B. Dkhil, M. Matsuda, C. Malibert and G. Calvarin, *Phys. Rev. B* **65**, 064106 (2002).

[Klotz 00] S. Klotz, M. Braden and J.M. Besson, *Hyperfine Interact.* **128**, 245 (2000).

[Koo 02] T.Y. Koo, P.M. Gehring, G. Shirane, V. Kiryukhin, S.G. Lee and S.W. Cheong, *Phys. Rev. B* **65**, 144113(2002).

[Kornev 05] I.A. Kornev, L. Bellaiche, P. Bouvier, P.E. Janolin, B. Dkhil and J. Kreisel, *Phys. Rev. Lett.* **95**, 196804 (2005).

[Kornev 07] I.A. Kornev and L. Bellaiche, *Phase Trans.* **80**, 385 (2007).

[Kulda 96] J. Kulda and J. Saroun, *Nucl. Instrum. Methods Phys. Res.* **A379**, 155 (1996).

[La-Orauttapong 03] D. La-Orauttapong, J. Toulouse, Z.G. Ye, W. Chen, R. Erwin and J.L. Robertson, *Phys. Rev. B* **67**, 134110 (2003).

[La-Orauttapong cm 03] D. La-Orauttapong, J. Toulouse, O. Svitelskiy and J.L. Robertson, cond-mat/0303004 (2003).

[La-Orauttapong 02] D. La-Orauttapong, B. Noheda, Z.-G. Ye, P. M. Gehring, J. Toulouse, D. E. Cox and G. Shirane, *Phys. Rev. B* **65**, 144101 (2002).

[Last 57] J.T. Last, *Phys. Rev.* **105**, 1740 (1957).

[Li 96] Z. Li, M.H. Grimsditch, C.M. Foster and S.K. Chan, *J. Phys. Chem.* Solids **57**, 1433 (1996).

[Lines&Glass] M.E. Lines and A.M. Glass, Principles and Applications of Ferroelectrics and Related Materials (Oxford University Press, Oxford, 2001).

[Lovesey] S.W. Lovesey, Theory of neutron scattering from condensed matter; Part 1: Nuclear scattering (Oxford University Press, 1986).

[Lushnikov 99] S.G. Lushnikov, S.N. Gvasaliya and I.G. Siny, *Physica B* **263-264**, 286 (1999).

[Naberezhnov 99] A. Naberezhnov, S.B. Vakhrushev, B. Dorner, D. Strauch and H. Moudden, *Eur. Phys. J. B* **11**, 13 (1999).

[Nelmes 86] R.J. Nelmes and A. Katrusiak, *J. Phys. C: Solid State Phys.* **19**, L725 (1986).

[Noheda 00] B. Noheda, D.E. Cox, G. Shirane, R. Guo, B. Jones and L.E. Cross, *Phys. Rev. B* **63**, 014103 (2000).

[Ogawa 03] T. Ogawa and Y. Numamoto, *Ferroelectrics* 286, 731 (2003); *Integrated Ferroelectrics* **63**, 533 (2004).

[Ohwada 01] K. Ohwada, K. Hirota, P.W. Rehrig, P.M. Gehring and B. Noheda, *J. Phys. Soc. Jpn.* **70**, 2778 (2001).

[Ohwada 03] K. Ohwada, K. Hirota, P.W. Rehrig, Y. Fujii and G. Shirane, *Phys. Rev. B* **67**, 094111 (2003).

[Park 87] S.E. Park and T.R. Shrout, *J. Appl. Phys.* **82**, 1804 (1987).

[Perry 64] C.H. Perry, B.N. Khanna and G. Rupprecht, *Phys. Rev.* **135**, A408 (1964).

[Petzelt 87] J. Petzelt, G.V. Kozlov and A.A. Volkov, *Ferroelectrics* **73**, 101 (1987).

[Popovici 75] M. Popovici, *Acta Cryst. A* **31**, 507 (1975).

[Ramirez 91] R. Ramírez, H. Vincent, R.J. Nelmes and A. Katrusiak, *Solid State Commun.* **77**, 927 (1991).

[Remeika 70] J.P. Remeika and A.M. Glass, *Mat. Res. Bull.* **5** **37**, (1970).

[Samara 03] G.A. Samara, *J. Phys.: Condens. Matter* **15**, R367 (2003).

[Sani 02] A. Sani, M. Hanfland and D. Levy, *J. Phys.: Condens. Matter* **14**, 10601 (2002).

[Sanjurjo 83] J.A. Sanjurjo, E. López-Cruz and G. Burns, *Phys. Rev. B* **28**, 7260 (1983).

[Saroun 00] J. Saroun, J. Kulda, A. Wildes and A. Hiess, *Physica B* **276-8**, 148 (2000).

[Saroun 04] J. Saroun and J. Kulda, *Proc. of SPIE* **5536**, 124 (2004).

[Scott 74] J.F. Scott, *Rev. Mod. Phys.* **46**, 83 (1974).

[Shirane 50] G. Shirane, S. Hoshino and K. Suzuki, *Phys. Rev.* **80**, 1105 (1950).

[Shirane 70a] G. Shirane, J.D. Axe, J. Harada and J.P. Remeika, *Phys. Rev. B* **2**, 155 (1970).

[Shirane 70b] G. Shirane, J. D. Axe, J. Harada and A. Linz, *Phys. Rev. B* **2**, 3651 (1970).

[Shirane 02] G. Shirane, S.M. Shapiro and J.M. Tranquada, Neutron Scattering with a Triple-Axis Spectrometer (Cambridge University Press, 2002).

[Siny 99] I.G. Siny, S.G. Lushnikov, R.S. Katiyar and V.H. Schmidt, *Ferroelectrics* **226**, 191 (1999).

[Smolenskii 58] G.A. Smolenskii and A.I. Agronovskaya, *Sov. Phys. Tech. Phys.* **3**, 1380 (1958).

[Squires 78] G.L. Squires, Introduction to the theory of thermal neutron scattering (Dover Publications Inc., New York, USA, 1978)

[Stock 05] C. Stock, H. Luo, D. Viehland, J.F. Li, I.P. Swainson, R.J. Birgeneau and G. Shirane, *J. Phys. Soc. Jpn.* **74**, 3002 (2005).

[Tagantsev 98] A.K. Tagantsev and A.E. Glazounov, *Phys. Rev. B* **57**, 18 (1998).

[Tinte 03] S. Tinte, K.M. Rabe and D. Vanderbilt, *Phys. Rev. B* **68**, 144105 (2003).

[Tomeno 01] I. Tomeno, S. Shimanuki, Y. Tsunoda and Y.Y. Ishii, *J. Phys. Soc. Jpn.* **70**, 1444 (2001).

[Tomeno 06] I. Tomeno, Y. Ishii, Y. Tsunoda and K. Oka, *Phys. Rev. B* **73**, 064116 (2006).

[Tornberg 70] N.E. Tornberg and C.H. Perry, *J. Chem. Phys.* **53**, 2946 (1970).

[Uesu 02] Y. Uesu et al, *J. Phys. Soc. Jpn.* **71**, 960 (2002).

[Vakhrushev 02] S.B. Vakhrushev and S.M. Shapiro, *Phys. Rev. B* **66**, 214101 (2002).

[Waghmare 97] U.V. Waghmare and K.M. Rabe, *Phys. Rev. B* **55**, 6161 (1997).

[Wakimoto 02a] S. Wakimoto, C. Stock, R.J. Birgeneau, Z.-G. Ye, W. Chen, W.J.L. Buyers, P.M. Gehring and G. Shirane, *Phys. Rev. B* **65**, 172105 (2002).

[Wakimoto 02b] S. Wakimoto, C. Stock, Z.-G. Ye, W. Chen, P.M. Gehring and G. Shirane, *Phys. Rev. B* **66**, 224102 (2002).

[Westphal 92] V. Westphal, W. Kleemann and M.D. Glinchuk, *Phys. Rev. Lett.* **68**, 847 (1992).

[Wu 05] Z. Wu and R.E. Cohen, *Phys. Rev. Lett.* **95**, 037601 (2005).

[Zhang 03] R. Zhang, B. Jiang, W.H. Jiang and W.W. Cao, *Mater. Letters* **57**, 1305 (2003).

[Zhong 94] W. Zhong, R.D. King-Smith and D. Vanderbilt, *Phys. Rev. Lett.* **72**, 3618 (1994).

Articles related to the thesis

[Kamba 05a]
S. Kamba, M. Kempa, V. Bovtun, J. Petzelt, K. Brinkman and N. Setter: Soft and central mode behaviour in $PbMg_{1/3}Nb_{2/3}O_3$ relaxor ferroelectric. *J. Phys.: Condens. Matter* **17**, 3965 (2005).

[Kamba 05b]
S. Kamba, M. Berta, M. Kempa, J. Hlinka, J. Petzelt, K. Brinkman and N. Setter: Far-infrared soft-mode behavior in $PbSc_{1/2}Ta_{1/2}O_3$ thin films. *J. Appl. Phys.* **98**, 074103 (2005).

[Kamba 05c]
S. Kamba, M. Kempa, M. Berta, J. Petzelt, K. Brinkman and N. Setter: Dynamics of polar clusters in relaxor ferroelectrics. *J. Phys. IV France* **128**, 121 (2005).

[Hlinka 06a]
J. Hlinka, M. Kempa, J. Kulda, P. Bourges, A. Kania and J. Petzelt: Lattice dynamics of ferroelectric $PbTiO_3$ by inelastic neutron scattering. *Phys. Rev. B* **73**, 140101 (2006).

[Kempa 06a]
M. Kempa, J. Hlinka, J. Kulda, P. Bourges, A. Kania and J. Petzelt: Lattice dynamics of cubic $PbTiO_3$ by inelastic neutron scattering. *Phase Trans.* **79**, 351 (2006).

[Kempa 06b]
M. Kempa, B. Janousova, J. Saroun, P. Flores, M. Boehm, F. Demmel and J. Kulda: The *FlatCone* multianalyzer setup for ILLs three-axis spectrometers. *Physica B* **385-386**, 1080 (2006).

[Hlinka 08]
J. Hlinka and M. Kempa: Soft mode dispersion and "waterfall" phenomenon in relaxors revisited. *Phase Trans.* **81**, 491 (2008).